Metal foam regenerators; heat transfer and pressure drop in porous metals

Farzad Barari

Supervisor: Dr Robert Woolley

2nd Supervisor: Professor Stephen Beck

Dissertation Submitted to the Department of Mechanical Engineering, University of Sheffield in partial fulfilment of the requirements for the

Degree of

Doctor of Philosophy

June 2014

Acknowledgment

I would like to express my special appreciation and thanks to my supervisor Dr Robert Woolley for his support and encouragement. It has been an honour for me to be his first PhD student. He taught me how to be a good experimentalist. I appreciate all his contributions of time and ideas to help me overcome the difficulties during my research. Without his supervision and constant help this dissertation would not have been possible.

I want to thank my second supervisor Professor Stephen Beck for his support, brilliant comments, remarks and engagement through the learning process of my PhD. Besides, he is a keen cyclist and I had a memorable time riding bike with him and other students around the Peak district National Park.

Furthermore, I would also like to acknowledge with much appreciation the crucial role of Dr Russell Goodall, who gave the permission to use all required equipment and the necessary materials to manufacture the metal foams. I would also like to thank him for his tremendous support for building the thermal test rig. I feel motivated and encouraged every time I attend his meeting.

I would like to thank Professor Shuisheng He and Professor David A Reay for being my examiners and giving the valuable suggestions and corrections to this work.

I take this opportunity to express my gratitude to technicians Mr Malcolm Nettleship and Mr Chris Grigson, who have willingly shared their precious time, knowledge and experience for manufacturing the test rigs. I can't say thank you enough for their tremendous support and help.

Many thanks go to Dr Taha Abdulla, Mr Erardo Elizondo Luna, Mr Ryan Marshal and Mr Ahmed Abuserwal for their help during my PhD, as well as being a good friend of mine.

I would like to thank my parents who raised me with a love and supported me to achieve my dreams. And most of all my special thanks go to my loving, supportive, encouraging, and patient wife, Ella, whose faithful support during my PhD is so appreciated. Your love and support means more to me than you will ever know.

Abstract

Open pore metal foams with moderate porosity (0.6 – 0.7) may be of interest as regenerators due to their high volumetric heat capacity and large specific surface area. Replication process is a low cost and simple foam manufacturing method which provides moderate porosity metal foams. Due to its simplicity, it provides many opportunities to investigate the effect of porosity, pore size and shape or their combination.

In this study, this process was used to manufacture metal foams. A method, called vacuum-gas, was the standard method for manufacturing metal foams in the University of Sheffield Material Science and Engineering department. This method was further investigated and two new methods, gas-only and mechanical infiltration, were introduced. Based on the foams produced by these methods, the gas-only method was adopted due to its repeatability and quality. The method was further investigated by manufacturing eight more samples (1.4-1.7 mm pore size) under various infiltration pressures and the optimum infiltration pressures were found for manufacturing foams with pore size of 1-1.1 mm, 1.4-1.7 mm and 2.0-2.36 mm.

A total of nine aluminium metal foams were manufactured for thermal and pressure testing. The manufactured foams had three different pore sizes, 1-1.1 mm (called Small samples), 1.4-1.7 mm (called Mid samples) and 2-2.36 mm (called Large samples). On average foams had porosity in the range of 0.62 – 0.65. Since this type of metal foams never been tested as a regenerator, two extra samples (a packed bed of 10000 2mm ball bearing and a packed bed of 100 layers of wire mesh No. 200) were made to compare with the manufactured foams and the results from other researchers.

A test rig was built to test the pressure drop under steady state flow condition from 1 to 6.5 m/s (permeability based Reynolds number from 20 to 175). The extended Darcy-Forchheimer equation and a cubic velocity of Darcy-Forchheimer were used to measure the permeability and form drag of the samples. The results showed that the cubic velocity equation had a better prediction of the permeability and form drag. The Small samples had the lowest permeability and highest form drag coefficient for metal foams. The wire mesh sample had the lowest permeability and lowest form drag among the tested samples.

In addition to steady state flow, samples pressure drop was also measured under oscillatory flow. A test rig was built to measure pressure drop and air instant velocity under oscillatory flow (1 to 19 Hz). The results showed that the oscillatory pressure drop was higher than steady state flow except for the Small samples which had higher pressure drop at steady state flow. The pressure drop for the wire mesh sample was measured to compare with other researchers data and a good agreement was observed with some of the published data. Moreover, the instant air velocity was measured by a hot-wire anemometer inside the connecting tube between the sample holder and the compressor. The results showed that the air velocity behaved like a turbulent flow during the acceleration and deceleration period.

A single-blow test rig was designed and manufactured to measure thermal performance of the samples. To estimate the average heat transfer coefficient of the samples, several types of the single-blow models were studied and the extended Schumann-Hausen model was implemented for predicting the samples' outlet air temperature history. Two matching techniques, maximum gradient and direct curve matching were used to march the experimental and modelled outlet temperatures history to estimate samples' *NTU* and average heat transfer coefficient. The results showed that *NTU* increased with decreasing of pore size. Based on mass flow rate Mid samples had the highest *h*, however the difference between the metal foam samples were insignificant. The foam samples had higher heat transfer coefficient than the ball bearing sample but the wire mesh sample had the highest heat transfer coefficient. The heat transfer results for the wire mesh and ball bearing samples were compared with published data and good agreements were observed.

Table of Contents

Nomenclature

A	Empirical constants
A_{cs}	Cross section area (m^2)
A_{hs}	Heat transfer surface area (m^2)
A_{OA}	Dimensionless oscillation amplitude
A_{ss}	Specific surface area (m^2)
B	Empirical constants
Bi	Biot number
C	Form drag coefficient (m^{-1})
C_p	Specific heat capacity at constant pressure (kJ/(kg K))
D_h	Hydraulic diameter of the pipe (m)
E	Instantaneous applied bridge voltage (V)
H	Elevation of the point above the reference point (Bernoulli's equation) (m)
K	Permeability (m^2)
L	Length (m)
M	Mass (kg)
N	Number of neighbouring data points
NTU	Number of Transfer Units
P	Pressure (Pa)
Q	Thermal energy (J)
$\dot{Q}$	Dissipated power (King's law) (V)
R	Resistance (Ω)
R_0	Reference resistance (Ω)
R_{20}	Hot-wire reference resistance at 20C (Ω)
R_T	Hot-wire total resistance (Ω)
R_w	Hot-wire resistance (Ω)
Re	Reynolds number
Re_k	Reynolds numbers (permeability-based)
Re_ω	Kinetic Reynolds number
R_{tc}	Heat capacity ratio
Rad	Radios
S_{max}	Maximum gradient
Sf	Shape factor
St	Stanton number
SSE	Sum of Squares Due to Error
SSR	Sum of Squares Regression
SST	Total Sum of Squares
T	Dimensionless temperature
T_0	Hot-wire reference temperature (°C)
T_w	Mean wire temperature (°C)
$\acute{T}_s$	Dimensionless sold temperature
V_p	Swept volume of the piston (m^3)
W	Wall thickness (m)
X	Dimensionless distance (Negligible thermal resistance model)
X	Distance between the wires in wire mesh (m)

$\acute{a}$	Constants
a	Constants
$\acute{b}$	Constants
b	Constants
d	Diameter m
di	Diffusion number
f	Friction factor
h	Heat transfer coefficient (W/(m^{2}K))
I	Current (A)
k_e	Effective thermal conductivity
k	Thermal conductivity coefficient (W/(m K))
$\dot{m}$	Flow rate (kg/s)
n	Empirical constants
p	Order of the spline
r	Residual (m)
r_h	Hydraulic radius (m)
s	Smoothing function applied to the data
t	Temperature (°C)
u_m	Cross-sectional mean velocity (m/s)
u_{max}	Maximum mean cross-sectional velocity (m/s)
v	Darcian Velocity (m/s)
x_t	Ratio of wire diameter to distance between the wires in wire mesh
x_{max}	Maximum fluid displacement (m)
y	Response value
$\hat{y}$	Predicted value of y
$\bar{y}$	Mean of y values
y_{ma}	Moving average (Eq. 8.3)

Greek symbols

α	Hot-wire temperature coefficient
ε	porosity
η	Dimensionless time (Schumann-Hausen model)
Θ	Dimensionless time
λ	Longitudinal thermal conduction parameter
μ	Dynamic Viscosity (kg/m s)
ν	kinematic viscosity (m2/s)
ξ	Dimensionless distance
ρ	Density (Kg/m^3)
τ_n	Dimensionless time
τ	Time (s)
φ	Phase angle (Radian)
ψ	Inlet air response time
ω	oscillatory angular frequency

Subscripts

cs	Cross section

e	Effective
f	fluid
fi	Fluid Initial
fmax	Fluid maximum
hs	Heat transfer surface
i	A single point in discretised x direction
l	A single point in discretised time dimension
m	mean
ma	Moving average
max	maximum
s	Solid
ss	Specific surface
T	total
w	wall
wire	Wire
0	At time zero
20	sensor temperature coefficient of resistance at T_{20}

Chapter 1 – Introduction and literature review

1.1 Introduction

A regenerator is a temporary heat storage which intermittently absorbs and releases the heat from/to working fluid respectively. It is mainly adopted in different applications such as Stirling engine where working fluid shuttles between a heated cylinder (expansion chamber) and a cooled cylinder (contraction chamber). Shown in Fig. 1.1 is a simple diagram of a regenerator. It shows the thermal energy transfers from the hot air to the regenerator and in reverse it passes thermal energy from the regenerator to the cool fluid. The major difference between a heat exchanger and a regenerator is the direction of the heat transfers between the fluids. In heat exchanger (gas-to-gas), thermal energy transfers from one gas to the wall between the gases and from the wall to the other gas in one direction. Therefore, high thermal conductivity material such as aluminium is desirable for heat exchanger. However, in a regenerator heat transfers from a gas to a solid and then the stored heat transfers from the solid to the gas at a later stage. Having high thermal conductivity causes the heat to transfer through the structure (longitudinal) of the regenerator as it reduces the temperature difference between the gas and the regenerator. This reduces regenerators' effectiveness. Having high volumetric heat capacity (density multiple specific heat capacity) is another important factor for applications such as Stirling engines which the size of the regenerator is curtail. For instance, for a given volume, a stainless steel regenerator can store nearly twice the thermal energy than an aluminium regenerator.

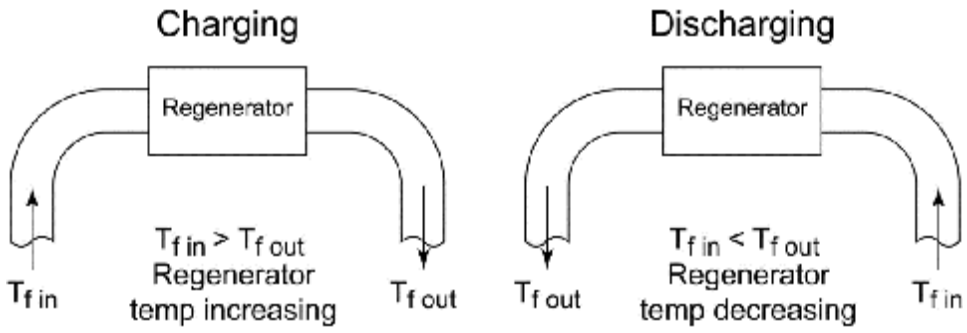

Fig 1.1 Schematic diagram of the operation of a regenerator in a thermal system. The switch between the charging and discharging phases may happen at several Hertz or a fraction of a

Hertz, depending on the application [1].

The other important factor for having a high performance regenerator is having a large specific surface area. Since the heat transfer resistance between the gas and the solid is much higher than the resistance inside the regenerator. Therefore, transferring the heat from the gas to the regenerator can be increased by increasing the specific surface area. However, increasing the surface area also increases the pressure drop and consequently increases the parasitic loss. These two factors, high specific surface area and low pressure drop, are conflicting factors and increasing one desirable factor (surface area) would also increase the other undesirable factor (pressure drop). Therefore, finding the optimum point can be challenging and it might be difference from one application to another application.

Packed beds of stainless steel wire mesh screens are commonly used as a regenerator for Stirling engine due to their high volumetric heat capacity, high specific surface area and high longitudinal thermal conductivity. However, they are not an ideal regenerator. They have high pressure drop and is difficult to seal the gap between the holder wall and the regenerator. This problem can be prevented by oversizing the wire meshes but is also increases the pressure loss even further [2]. In addition, stacking the wire mesh screen is difficult and the packed bed performance depends on the packing method (random or structured packing) and space between the screens.

1.2. Metal foam as a regenerator

Based on application purpose there are two methods in literatures of measuring thermal performance of metal foams:

1- Measuring the heat transfer between the wall and the sample (e.g. heat exchangers, heat sinks for cooling electronic components, etc.)
2- Measuring the heat transfer between the fluid and the sample (e.g. regenerator, recuperators, advance burners etc.)

In method one, generally metal foam is attached to a hot surface and the heat transfer rate from the surface to the passing fluid is measured. Then the results are compared with the results when no metal foam is attached to the surface. This method is mainly adopted to

study the performance of metal foams as a heat exchanger [3–7] or as a fins to increase the heat transfer surface of heat exchangers [8]. A good review of thermal transportation in high porosity cellular metal foam was done by Zhao [9] and more information regarding this method can be found in this review.

The second method measures the heat transfer rate from the fluid to the solid. In this method, a fluid flows steadily through the sample which is allowed to equilibrate with the passing fluid. A step change in temperature is applied to the inlet flow. The outlet temperature history is then measured until the new equilibrated temperature is achieved. The heat transfer coefficient is estimated by matching the outlet temperature curve with the curve predicted by the model. This method is called single-blow method and it was introduced by Schumann and Hausen [10,11]. A full literature review of this method will be given in chapter 6.

Majority of the studies have been conducted based on the second method were mainly focused on the packed beds [10,12–15] with porosities range of 0.4 – 0.5 or stack of wire meshes [16–20]. Since the internal structure and porosity of metal foams are different from packed beds, the results from these studies may not be applicable to metal foams. In comparison to packed beds, a limited number of studies have been conducted on metal foams and ceramic foams [21–23]. Ceramic foams have similar internal structure like metal foams but they have lower thermal conductivity than metal foams. Therefore, the results from these studies may also not be applicable to metal foams.

Open-cell metal foams are thought to be suitable for manufacturing regenerators due to their high specific surface area and low pressure drop. However, relatively few studies have been done to investigate the thermal performance of metal foam as a regenerator. Researchers [20,24] have conducted a series of tests to measure the pressure drop and heat transfer coefficient of high porosity open-cell aluminium foams under oscillatory flow and reported lower pressure drop compared to the wire mesh screens. Although high porosity metal foams (90-95%) has shown less pressure drop and high heat transfer coefficient, their performance is limited due to their low volumetric heat capacity and high dead volume.

Medium porosity metal foams (60-70%) have received less attention as they have not been readily manufactured. This type of metal foams has a better volumetric heat capacity and

less dead volume due to their lower porosity. Hwang et al. [25] studied thermal performance of three different porosity (ε=0.7, 0.8 and 0.95) and their results showed that both friction factor and volumetric heat transfer coefficient increases with increase with decreasing the foam porosity. Some researches tried to improve the thermal performance of high porosity aluminium foams by compressing the foams and decreasing their porosity. However, they didn't test the compressed foam as a regenerator[26].

The replication process or "the space-holder technique" is one of the simplest and most inexpensive methods [27] of producing foams with moderate porosity (60 - 70%). It has the potential to compete with conventional regenerators like wire mesh screens (porosity of 50 – 70%). In this process the metal foam porosity, pore size, pore shape and material can be altered. Therefore it provides an excellent opportunity for testing the effect of changing each of these parameters or their combination to optimise their performance. In addition, this type of metal forms has not been tested as a regenerator.

The primary goal for this research is to study metal foams with moderate porosity as a regenerator. To achieve this goal, the replication process for manufacturing metal foams technique was investigated and improved. Three different pore sizes aluminium foam (three of each pore size) and two additional conventional regenerators (a randomly packed of 2mm steel ball bearings and a packed bed of 100 layers of steel wire mesh No 200) were manufactured. The results of this investigation on replication process and samples properties will be presented in Chapter 2. Pressure drop under unidirectional flow will be discussed in Chapters 3 and 4. The samples were tested under oscillatory flow to evaluate their pressure drop performance. The experimental presider and the results will be given in Chapter 5 and 6. Thermal performance of the samples was evaluated by the single-blow method. A mathematical model and data reduction technique for the single-blow method will be presented in Chapters 7, 8 and 9. The overall performance of the samples will be discussed in Chapter 10 and Conclusions and Future Work will be in Chapter 11.

Chapter 2 – Metal foam manufacturing

2.1. Replication process

Porous metal foams can be made by casting (or infiltrating) molten metal around a space holder (or preform) to retain spaces in the molten metal. By removing the space holder chemically or thermally a porous metal can be produced. This process is known as Replication [27]. An application of the method is using sodium chloride (salt) particles as the space holder to make aluminium foams [28–30]. The salt-aluminium method was first developed by Seliger and Deuther [31] has the advantages of being inexpensive, plus the salt is non-toxic and easily removed with water. The pore size and porosity can be altered by changing the preform (shape and size of the particles; and density of the preform), infiltration pressure and method of infiltration[28].

In this study aluminium foams were manufactured by the salt-aluminium method. To make foams with different pore sizes, three different salt particles sizes (1-1.1 mm, 1.4-1.7mm and 2-2.36 mm) were used to make the preforms. The preform was made by randomly packing (pouring salt in a mould) the salt particles into a mould. After preparing the preform molten aluminium was infiltrated into the preform. The infiltration method was improved and developed throughout in this study.

In this chapter, the preform preparation will be explained. Then the test rig used for making the foam will be discussed. Finally, the different methods of infiltration and the effect of infiltration pressure will be presented.

2.2. Preform preparation

The first step in the replication foam manufacturing process is preparing the preform. The preform is the negative shape of the foam as it fills all of the space that will become pores. The structure of the foam can be changed by using different shape and size of the space holder. The preform material must fulfil three main conditions [27]:

1- Have a higher melting point than the metal being cast.
2- Be chemically stable in contact with the molten metal.

3- Easy to remove once the metal has solidified.

Sodium chloride fulfils all of these conditions, and was used here. Its melting point is 801°C [32] and it is chemically inert in contact with aluminium during the infiltration and leaching steps. Moreover, removing it from the foam does not create toxic or hazardous by-products [27].

Initially ordinary rock salt was used to make the preform for this experiment. However, it was found to have some disadvantages. It cracked at high temperature (740 ^{o}C) and during the infiltration aluminium flowed into the resulting cracks and altered the general structure of the foam. To prevent the salt from reacting with oxygen it was necessary to heat it under vacuum. If this was not done, the rock salt turned into an ash like powder, likely due to the presence of impurities. As a result of this water softening tablets were used to overcome these problems.

The water softening salt tablets were obtained in the form of lozenges with typical diameter of 20 mm. They were then crushed and sieved to obtain the desired size. To get salt particles in the required range, particles were passed through several grades of sieves. A schematic view of the sieve order is shown below.

Fig. 2.1, The order of the sieves used to separate the particles size.

The crushed salt particles were poured in the first sieve which was shaken to separate the particles. As it can be seen from the Fig. 2.1, particles that remained in the top red sieve were used to make the foam. For instance, particles remained in the sieve 2.00 mm had size between 2.00 mm to 2.36 mm. The three sizes of salt particles used in this study were those found in the red sieves in Fig. 2.1.

Packing density has an inverse relation with the porosity of the sample. If the salt particles were packed randomly in the mould, the maximum relative densities which could be achieved were below 0.7 but with sintering this can be increased up to 0.8 [33]. Some researchers have studied modification of the starting salt grains using additives that control the growth habit of the salt crystals or by a melting process to produce roughly spherical crystals [34].With these types of preforms exotic foams can be manufactured with replication method. However making these types of preforms is expensive and was not investigated here, as an aim of the study was to manufacture inexpensive foams. Randomly packed crushed salts were used for making all the preforms in this study.

Random packing the crushed salt particles has an effect on the manufactured foam structure and alters the magnitude of the pressure loss of fluids through the manufactured foam. Ergun [35] showed that viscous energy losses were proportional to $\frac{(1-\varepsilon)^2}{\varepsilon^3}$ and the kinetic energy losses to $\frac{(1-\varepsilon)}{\varepsilon^3}$ (ε is samples porosity). This indicates the strong influence of porosity on pressure drop. As a result of random packing, fluctuation of sample porosity was inevitable and the effect of this randomness on pressure drop will be discussed in Chapter 3.

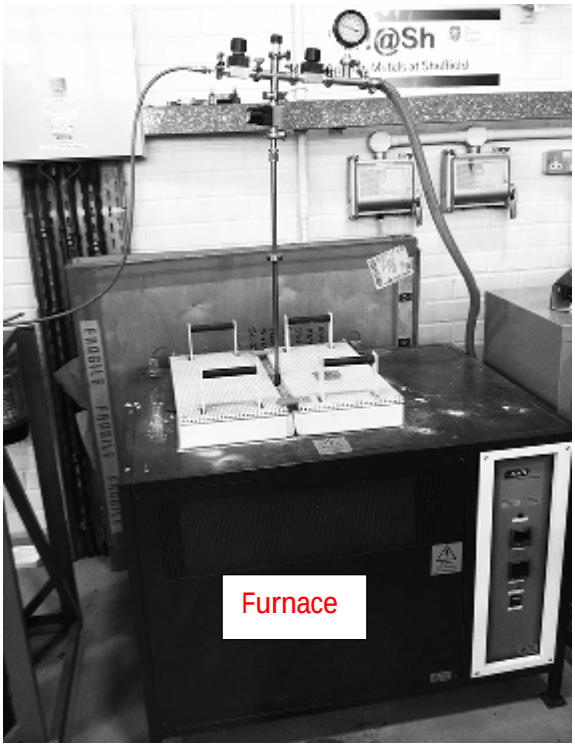

Fig. 2.2a, Foam manufacturing rig

2.3. Test rig description

Replication method had been one of the foam manufacturing methods used at Material Science and Engineering department in the University of Sheffield. The first replication foam manufacturing rig was only able to produce foam inside a test tube (19mm diameter) with an induction heating system[36] [27]. The current test rig (Fig. 2.2a) was manufactured to produce larger size metal foam. The vacuum-gas method was implemented by Abdulla [37] to manufacture the metal foam. The current author introduced two new methods to overcome the issues Abdulla highlighted in his work.

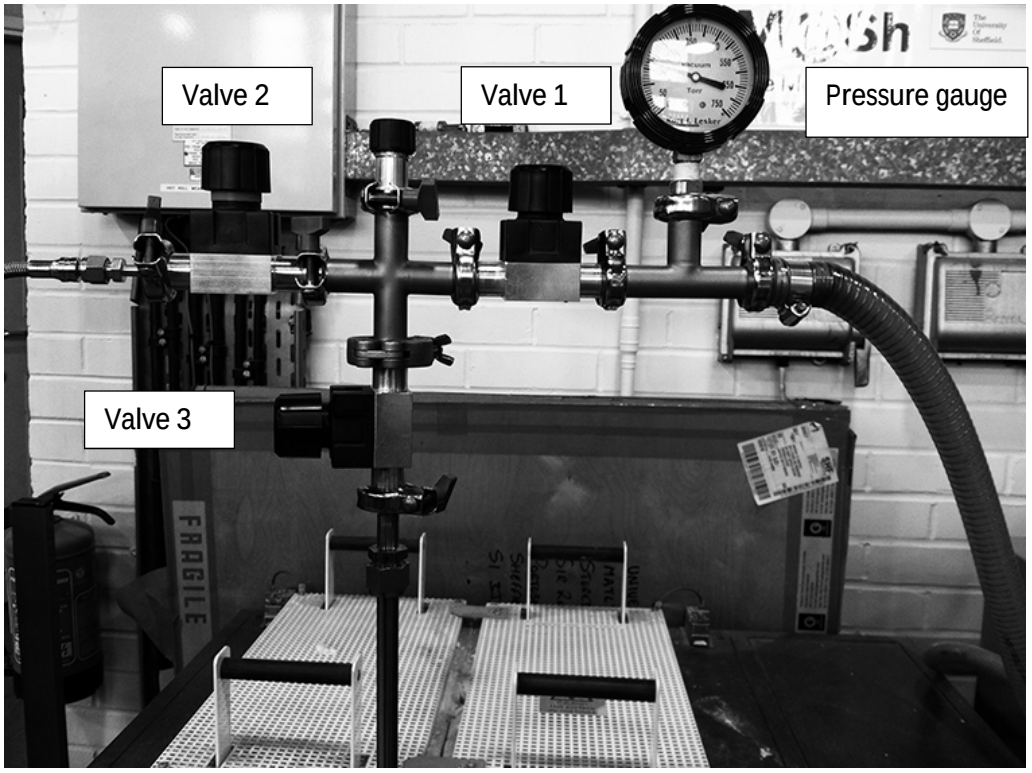

Fig. 2.2b, Valves positions in the metal foam manufacturing rig

In order to infiltrate the molten aluminium into the preform three methods (vacuum-gas, gas-only and mechanical infiltration) were tested. For applying the gas and vacuum-gas methods the same test rig (shown in Fig. 2.2c) was used. It consisted of an argon gas cylinder, a vacuum pump, a furnace and a mould. They were connected by stainless steel pipes, via three valves and appropriate fittings. The gas pressure was monitored with a pressure and vacuum gauges. The argon pressure could be regulated up to 10 bar and the flow of argon leaving the cylinder could also be monitored.

The valve 1 isolated the mould and the gas cylinder from the vacuum pump and was closed to pressurise the mould. During the vacuum process, valve 2 was closed to prevent damage to the pressure gauge. Valve 3 was used to isolate the mould from the system and to detect any gas leakage from the piping system. Quick release clamps were fitted between the mould and the valve 3 so the mould could be separated from the system. The vacuum pump could provide a vacuum down to 750 Torr. The furnace was an electrical furnace with a heater controller that could be programed for various heating processes.

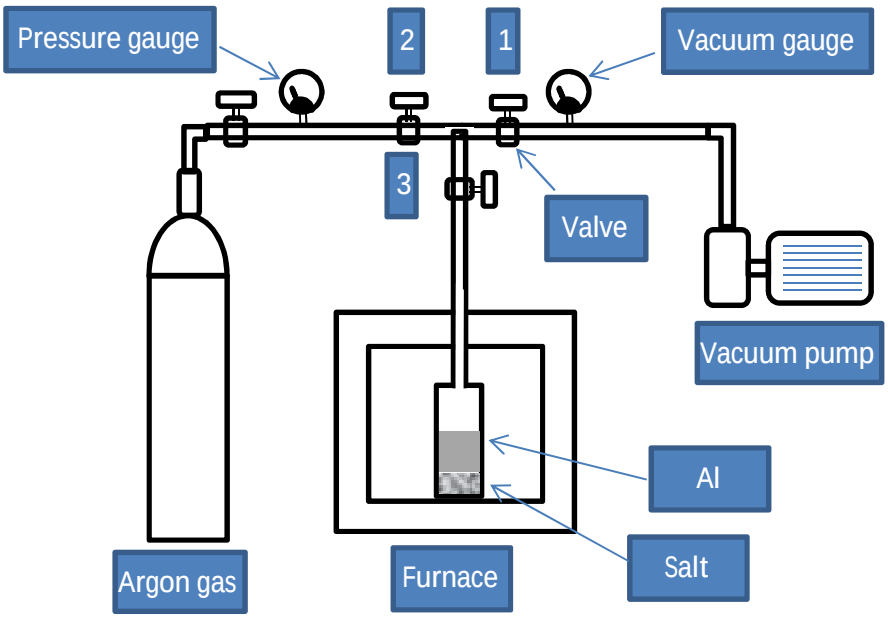

Fig. 2.2c, A schematic view of the foam making test rig.

The mould consisted of two sets of flanges (top and bottom) and a cylinder. This assembly was held together by six M8 bolts and nuts. All the components of the mould were made from stainless steel to withstand the high temperatures in the furnace. In order to seal the mould, graphite gaskets were placed between the flanges.

During foam manufacturing the stainless steel retaining nuts were found to deform under the high load (nuts were tight fastened to provide a good vacuum inside the mould) and temperature (740°C). After being used two or three times they were found to damage the studs. Replacing the studs was expensive therefore the stainless steel nuts were replaced by mild steel nuts which were discarded after each experiment.

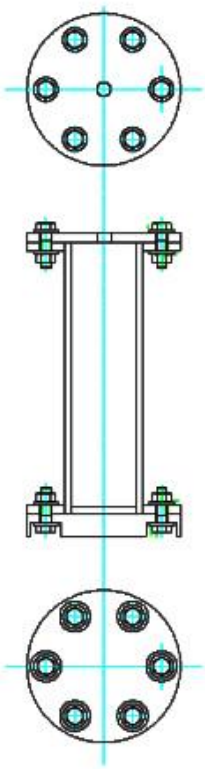

Fig. 2.3, A schematic view of the mould used for making the foams.

2.4. Foam making procedure with gas infiltration

Since the surface tension of the molten aluminium is high, wetting the salt granules without external pressure is difficult. In order to infiltrate molten aluminium into the preform two gas infiltration methods (gas-only and vacuum-gas) were tested. The vacuum-gas method had been used for foam manufacturing before but it had reproducibility and quality issues. Therefore the gas-only was developed and the foams manufactured by two methods were compared.

2.4.1 Vacuum-gas infiltration

In this method, first the inside of the mould was coated with boron nitride using an aerosol spray. This prevented the molten aluminium sticking to the wall of the mould. Once the coating dried seventy five grams of salt granules were poured into the mould and packed. Then approximately 200 grams of 2 inch aluminium bar (99.9% purity) was placed on top of the salt. After placing the gaskets and closing the lid the air inside the mould was removed

by vacuum pump to a final pressure of 720 Torr. Following a check to ensure the mould could hold the pressure it was placed inside the furnace. The furnace was heated using the profile depicted in Fig. 2.4. The vacuum pump was left on to maintain the vacuum inside the mould until 5 minutes before the end of the heating process.

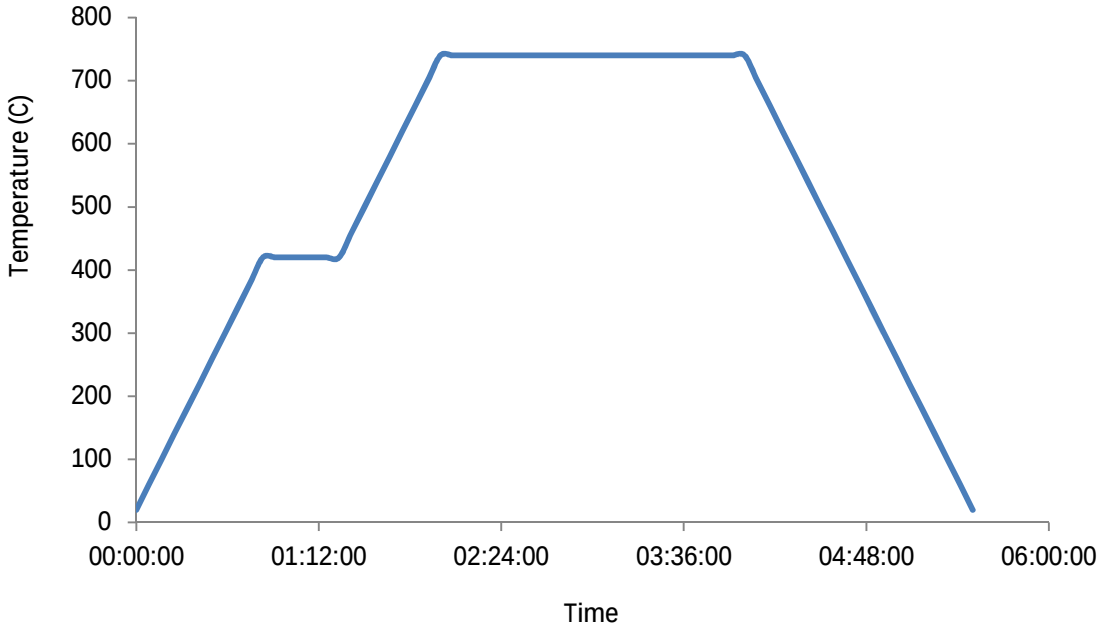

Fig. 2.4, Heating profile of the furnace.

From Fig. 2.4 it can be seen that that the mould was heated at two stages. For the first stage the mould was gradually heated up to 420 °C and kept at this temperature for 35 minutes to make sure all the parts heated uniformly. After that, the furnace temperature was gradually increased up to 740 °C and was kept there for two hours to melt the aluminium and heat the preform. Valve 1 was then closed to isolate the mould from the vacuum pump and argon was injected into the mould.

The flow rate of the gas was crucial. Molten aluminium on top of the preform does not wet the surface of the mould and by applying gas at too low flow rate, gas could leak from the gap between the mould and the molten aluminium (Fig. 2.5) and filled the negative pressure inside the preform (P1). As a result, the pressure difference between the top and bottom of the molten aluminium reduced and there was either no or partial infiltration (Fig. 2.6a). At high gas flow rates the connecting pipe to the mould acted as an air jet and sprayed molten aluminium into the preform. This made a cone shape structure under which salt granules

became trapped (Fig. 2.5). Difficulty of controlling the air flow rate made the repeatability of this method poor.

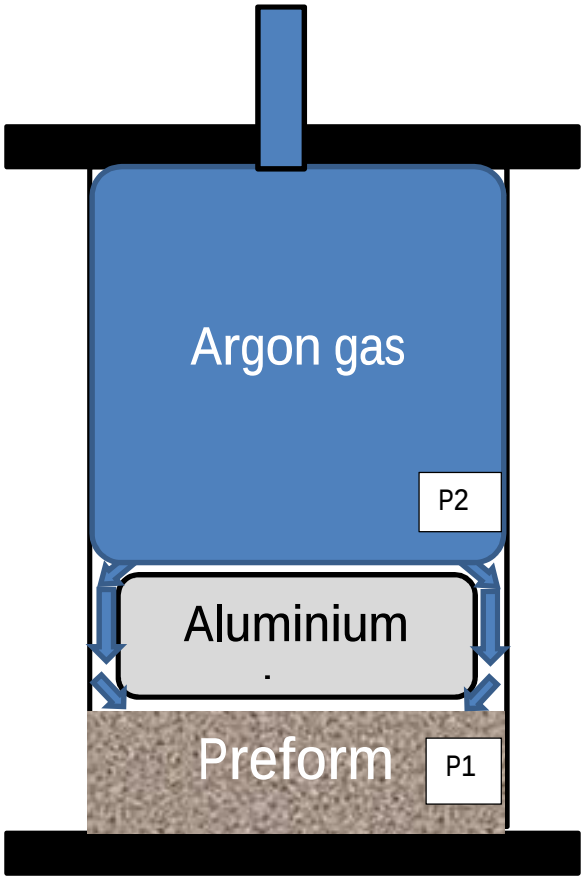

Fig. 2.5, Salt particles trapped inside the aluminium made with vacuum-gas method

During the infiltration process the pressure inside the mould was kept at one bar. Once the gas had infiltrated the molten aluminium, the mould was kept inside the furnace for 5 minutes and then it was taken out of the furnace and placed on top of a large copper block. This helped the solidification to start from the bottom to top of the sample and from the outer edge to the centre of the sample. It was important to keep the valve 3 shut to avoid reducing the mould pressure while the aluminium was still not fully solidified.

This infiltration method had two further disadvantages:

- It was not suitable for the preforms made from porous material or material with cracks in such as dough preform used by [38] (a mixture of salt, flour and water shaped together and heated to burn the flour). This kind of preform had a porous

structure and under vacuum the molten aluminium was sucked into the structure of the preform (Fig. 2.6c).

- If the pressure inside the mould was too high the molten aluminium enclosed the salt granules after infiltration and made it impossible to leach the salt completely out of the sample. Fig. 2.7 shows the foam with salt particles trapped inside the aluminium that could not be dissolved by leaching.

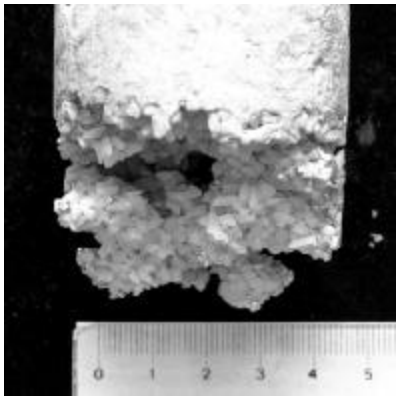

Fig. 2.6a, Low flow rate gas infiltration

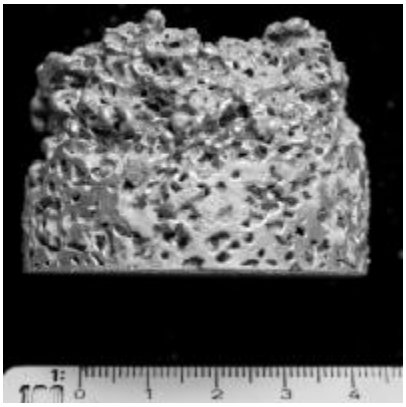

Fig. 2.6b, High flow rate gas infiltration

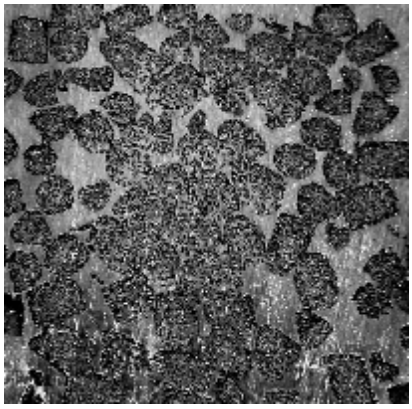

Fig. 2.6c, Preform made from dough and infiltrated with vacuum-gas method

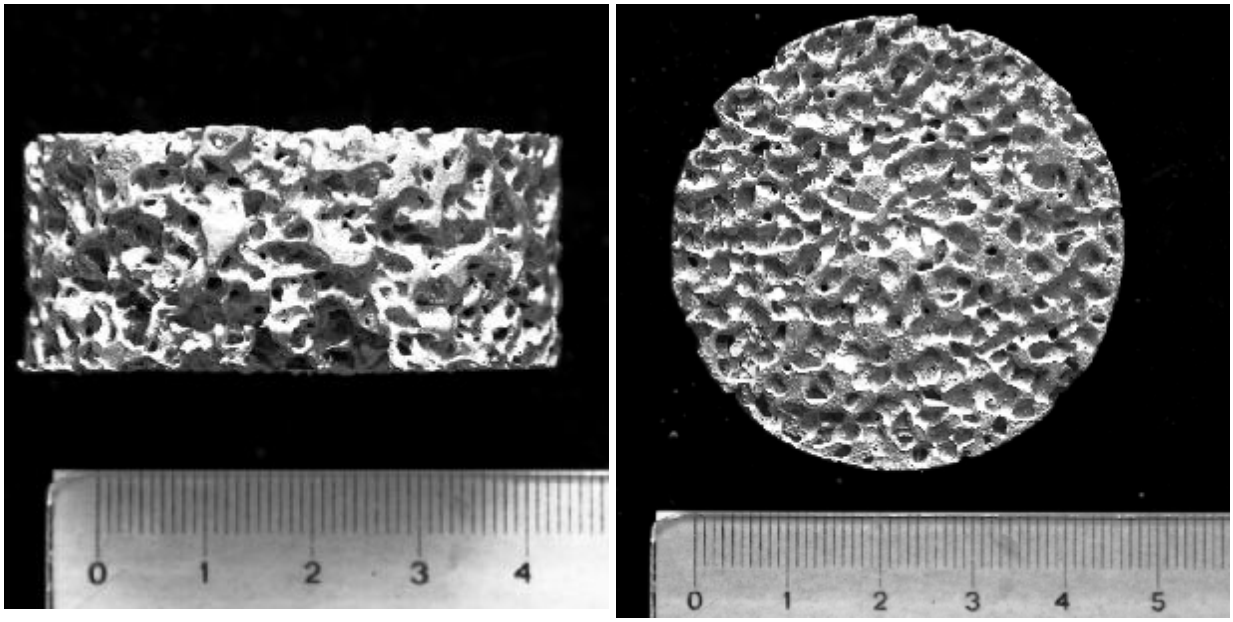

Fig. 2.7, Salt particles trapped inside the aluminium made with vacuum-gas method

2.4.2 Gas infiltration

In this method one third of the mould was filled with crushed salt and rest of the mould filled with 51 mm aluminium bar. The size of aluminium bar placing on top of the preform was essential for successful infiltration. If the height of aluminium bar on top of the salt was smaller than 30 mm, gas could leak from the side of the molten aluminium into the preform during the infiltration stage. This negated the pressure difference between the top and bottom of the molten aluminium; and stopped the gas infiltrating the molten aluminium into the preform.

For this method, the air inside the mould was removed with a vacuum pump and any leakage was checked. Argon gas then injected into the mould and pressurised to atmospheric pressure. This could also be achieved by letting air into the mould and equalising the pressure inside and outside of the mould. However, if during the heating process the molten aluminium was exposed to air a black oxide layer was formed on top of the molten aluminium (Fig. 2.8). The use of argon gas avoided this. The pressure was kept constant during the heating process by venting gas from the mould.

Fig. 2.8, Top part of the molten aluminium- Left melted under argon gas- Right- melted under atmospheric air

The same heating cycle that was used for the vacuum-gas method was used here and is shown in Fig. 2.4. At the end of heating process aluminium was ready for infiltration. Setting the right infiltration pressure is vital for the manufacture of a good sample as it defines the closeness of the pores in the foam. The optimum pressure depended on the size and shape of the salt particles which influence the permeability of the preform. The viscosity of the molten aluminium also had an influence.

The method manufacture, in particular the infiltration pressure, will also influence the pressure drop by increasing the density and closeness of the pores. As it was discussed previously, a certain threshold pressure is necessary for the molten aluminium to penetrate the preform. Once the threshold pressure is achieved, the molten aluminium only invades larger gaps between the salt particles or even the preform. In order to fill finer pores significantly higher pressures are needed. The gradual nature of infiltration has been quantified by means of "drainage/imbibition" curves which is plotted the fraction of open pore space filled by the metal as a function of the infiltration pressure [39]. The curve depends on a number of factors including[39]:

1- Intrinsic capillary parameters (wetting angle and the surface tension of the molten metal)
2- The average pore size
3- Pore size distribution
4- Shape of solid elements

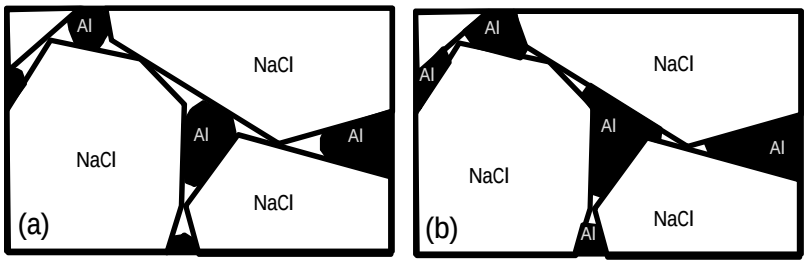

Fig. 2.9, Sketch of progressive infiltration at low applied pressure (a) and high applied pressure (b)[39].

Shown in Fig. 2.9 are sketches of progressive infiltration between touching salt particles at low and high infiltration pressures. By increasing the infiltration pressure the gaps between the salt particles fill with aluminium and reduce the window between the pores and consequently increase the pressure drop. In addition, increasing the infiltration pressure also reduces the porosity of the samples.

Samples with medium pore size were manufactured at various infiltration pressures and it was found that the sample made at 4.5 bar had low pressure drop and had uniform structure. The result of this experiment will be presented at Chapter 3. By assuming that

small pore size particles require higher infiltration pressure and vice-versa for large size salt particles, different samples were made at pressure above and below that 4.5 bar for small and large samples and it was found that for small pore size sample 5 bar pressure and for large pore size 4 bar infiltration pressure was sufficient for making uniform samples. Samples, which were made under pressure lower than specified pressure, did not fully infiltrated and samples made under higher specified pressure were unusable since the preform was trapped inside the foam. For instance, shown in Fig. 2.10a is a sample with large pore size (2-2.36mm) that was made at 7 bar infiltration pressure. The pores were nearly blocked by the aluminium and salts were trapped inside the sample which could not be dissolved. An example for samples made under pressure lower than specified pressure can be seen in Fig. 2.10b. This sample(2-2.36mm pore size) were made under 2 bar infiltration pressure and was partly infiltrated There is a notable defect near the bottom of the sample (marked with a red oval).

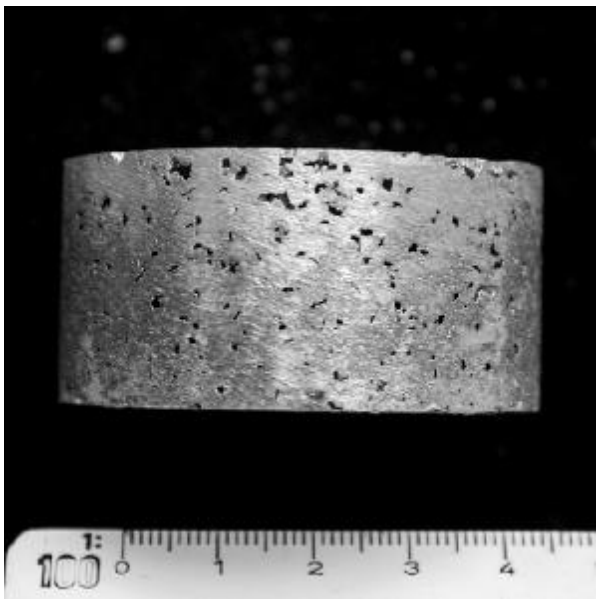

Fig. 2.10a, Large pore size sample made under 7 bar pressure.

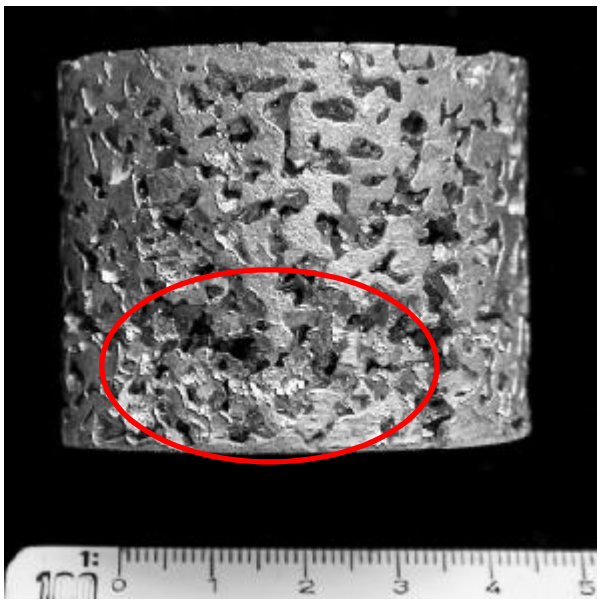

Fig. 2.10b, Large pore size sample made under 2 bar pressure.

Shown in Fig. 2.11a, 2.11b and 2.11c are samples made with gas-only infiltration. A total of nine samples (three for each pore size) were manufactured with this method, their properties are given in Table 2.1.

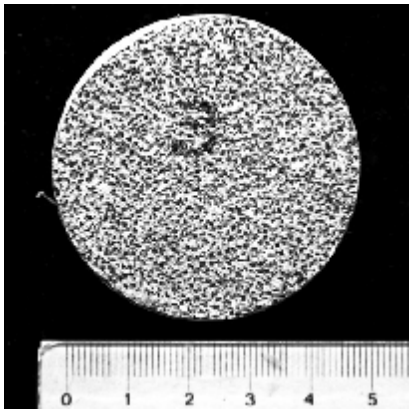

Fig. 2-11a, Small pore size foam made with gas infiltration

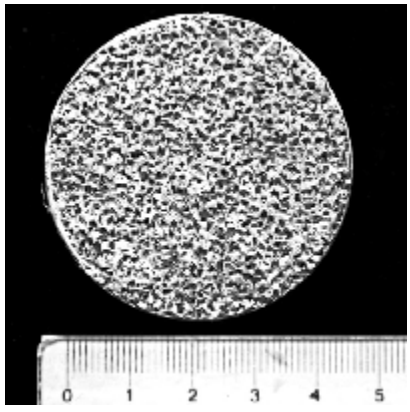

Fig. 2-11b, Mid pore size foam made with gas infiltration

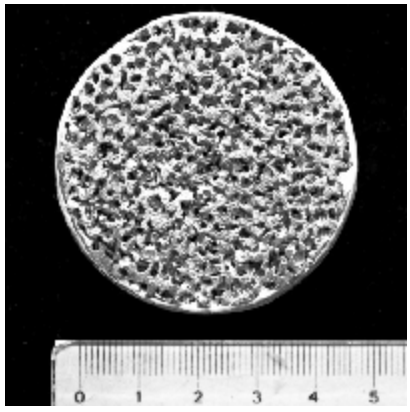

Fig. 2-11c, large pore size foam made with gas infiltration

To calculate samples porosity, first a sample's weight and volume were measured. Then weight of a solid aluminium bar similar to the sample (same volume) was calculated by knowing the pure aluminium density (2.7 g/cm3 provided by the supplier). Now the porosity can be calculated by subtracting these two values and calculating the percentage of the empty space inside the sample.

Table 2.1 – Properties of the foams made by gas-only infiltration method.

Name	Grain sizes	Weight (gr)	Length (mm)	Diameter (mm)	Porosity
Small 1	1-1.18mm	51.7	24.7	51.1	0.62
Small 2	1-1.18mm	51.3	25.1	51.1	0.63
Small 3	1-1.18mm	57.8	25.7	51.1	0.59
Mid 1	1.4-1.7mm	49.9	23.8	51.1	0.62
Mid 2	1.4-1.7mm	52.0	26.5	51.1	0.64
Mid 3	1.4-1.7mm	48.7	24.5	51.1	0.64
Large 1	2-2.36mm	47.4	25.5	51.1	0.66
Large 2	2-2.36mm	48.8	25.3	51.1	0.65
Large 3	2-2.36mm	51.4	26.7	51.1	0.65

2.5. Mechanical infiltration

An external force is required for infiltrating molten aluminium. Here the external force used to wet the salt granules with molten aluminium was applied by a piston inside the mould. Two new moulds (20 mm and 51mm diameter) were designed and manufactured to implement this method. A schematic of the mould with piston can be seen in Fig. 2.12. The

aluminium bar was placed under the preform since the air trapped inside the preform could be forced out of the preform by the molten aluminium. If the aluminium bar was placed on top of the preform the air inside the preform stopped the aluminium fully infiltrating the preform.

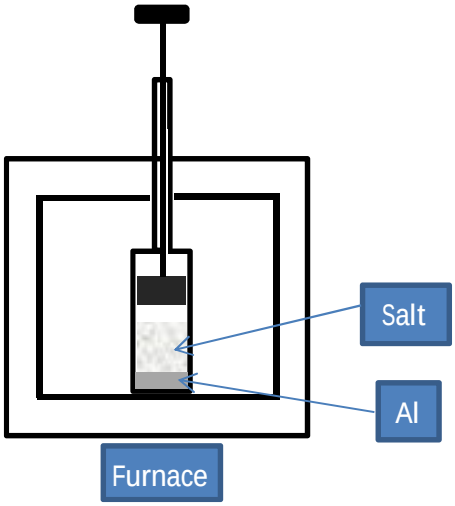

Fig. 2.12, Schematic view of mechanical infiltration rig

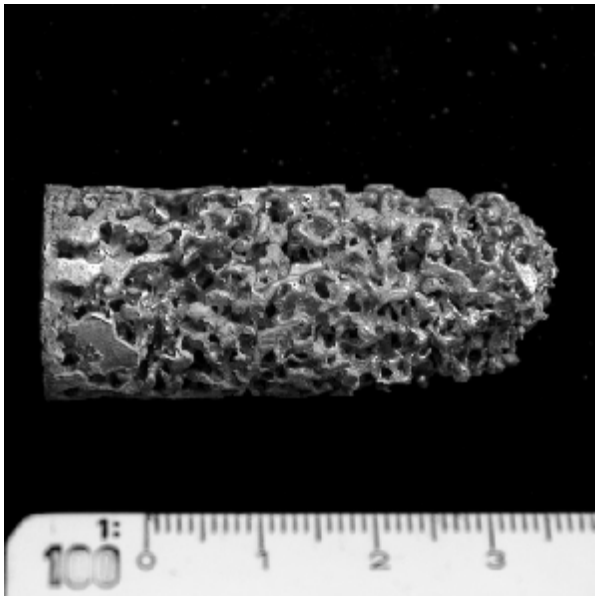

Fig. 2.13a, Partially infiltrated 20 mm foam made with mechanical infiltration method.

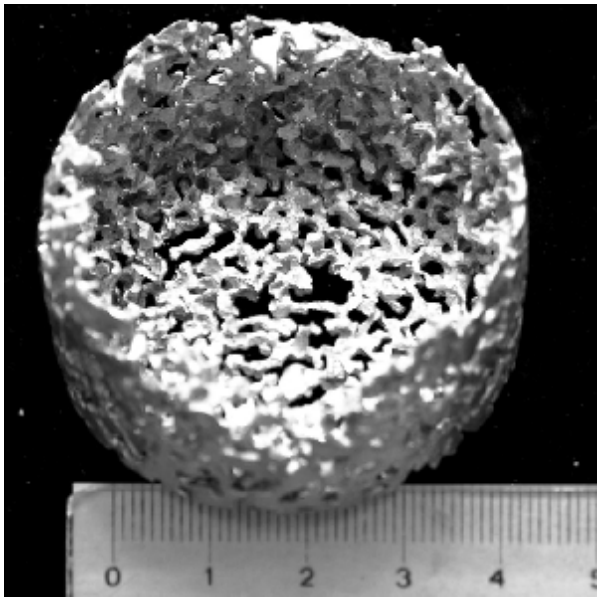

Fig. 2.13b, Partially infiltrated 51 mm foam made with mechanical infiltration method.

Higher forces were needed to infiltrate the preform with smaller particles compared to larger particles. For fine salt particles (<1.1 mm) a hydraulic press was used whilst a manual press could be used for larger particles (>1.1 mm). Similar to packed beds, porosity of the

preforms were higher close to the cylinder wall than in the centre. This effect depends on the tube/particle diameter ratio and has been shown to be negligible when the ratio is larger than 12 [40]. Consequently, foams made with this method had high porosity at the centre compared with that close to the wall. Problems occurred with molten aluminium leaking from the high porosity area at the top of the preform and not infiltrating the preform.

Size comparison- Meatal foams and a one pence coin

Fig. 2.14a, Large pore size

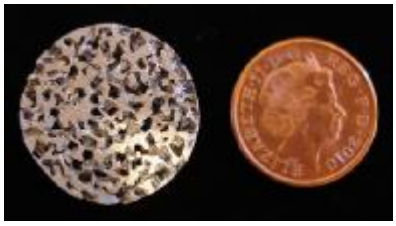

Fig. 2.14b, Medium pore size

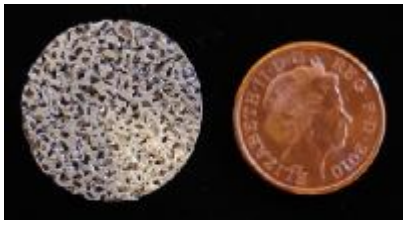

Fig. 2.14c, Small pore size

In order to overcome the aforementioned problem the furnace temperature was changed to alter the viscosity of the molten aluminium. Three different temperatures, 760ºC, 740ºC and 720ºC, were tested for this study. It was found that at 760ºC the salt granules started to deform under the piston pressure and blocked the pores inside the preform. This blockage stopped molten aluminium from infiltrating the preform. The viscosity of the molten aluminium was high at 740ºC and it tended to infiltrate from the larger pores or from outside of the preform. A temperature of 720ºC was found to give the best results. Table 2.2 shows the properties of the successful samples that were later tested.

Table. 2.2 – Properties of 20 mm diameter foams made from mechanical infiltration

Name	Grain sizes (mm)	Weight (g)	Length (mm)	Volume (mm^3)	Al weight (g)	Porosity
S1	1-1.18	4.82	18.2	5717.6	15.43	0.69
S3	1-1.18	5.73	23	7225.6	19.50	0.71
S4	1-1.18	5.91	23.88	7502.1	20.25	0.71
M1	1.4-1.7	4.51	18.98	5962.7	16.09	0.72
M2	1.4-1.7	4.89	18.51	5815	15.70	0.69
M3	1.4-1.7	6.37	23.9	7508.4	20.27	0.69
M4	1.4-1.7	5.78	23.56	7401.5	19.98	0.71
L1	2-2.36	3.91	14.9	4680.9	12.63	0.70
L2	2-2.36	4.47	16.9	5309.2	14.33	0.69

The porosity of these samples was found to vary along their height. The porosity was at its lowest at the bottom and increased upwards. The reason for this could be that during solidification the molten aluminium inside the preform contracted and since it was still in liquid state it pulled the molten aluminium from the outside of the preform. The excess aluminium which stayed on top of the preform was pulled into the foam but since there was no excess aluminium in the bottom of the mould the foams had lower density there. It can be seen from the table that these samples had higher porosity then the samples made from the gas-only method. One of reason for having higher porosity could be having a lower density at the bottom of the samples made with this method.

Foams of 20 mm diameter were made for testing the foam manufacturing methods since they needed fewer raw materials (aluminium and crushed salt) for making samples. However, the diameter of these samples was not large enough to avoid the wall effects (tube/particle ratio>12) and the number of pores per tube diameter was insufficient to provide a statistically representative sample. Therefore, 20 mm samples were not used for pressure and thermal test in this study.

Chapter 3 - Steady state pressure drop

3.1. Empirical model

Fluid flow through a porous matrix has been studied for over 150 years. Darcy [41] published what later became known as Darcy law in 1856 which states that for slow moving fluids pressure drop per unit length of a porous medium is proportional to the dynamic viscosity and velocity of the fluid, and inversely proportional to the permeability of the porous matrix. The fluid velocity, *v,* can be either the Darcian velocity (based on the cross-section of the channel) or the pore velocity (dividing the Darcy velocity by volumetric void fraction of the porous matrix). However, this must be stated when presenting the results.

$$\frac{\Delta P}{L} = \frac{\mu}{K}\mathrm{v} \qquad \text{Eq.3.1}$$

The above equation is only valid for the low permeability-based Reynolds numbers (Re_k=1) [42] and for higher flow velocities, another term must be added to accurately model the pressure drop. Osborne Reynolds was the first to formulate the pressure drop as the sum of two terms (Eq. 3.2). He showed that the pressure drop is proportional to the first power of the fluid velocity and the second power of the fluid velocity times the fluid density. In this equation *a* and *b* are constant.

$$\frac{\Delta P}{L} = a\mathrm{v} + b\rho\mathrm{v}^2 \qquad \text{Eq. 3.2}$$

Ergun showed that as the velocity approaches to zero, the ratio of pressure drop to velocity will become constant. At high velocities the first term becomes negligible in comparison to the second term [35].

$$\lim_{\mathrm{v}\to 0}\left(\frac{\Delta P/L}{\mathrm{v}}\right) = \lim_{\mathrm{v}\to 0}(a + b\rho\mathrm{v}) = a \qquad \text{Eq. 3.3}$$

The first term of Eq. 3.2 represents viscous energy loss (as defined by Darcy) and the second term represents the kinetic energy loss. Dupuit [43] and Forchheimer [44]suggested a quadratic velocity term to extend the Darcy law to accommodate the effect of form drag at

high velocity. The extended Darcy-Forchheimer equation (Eq. 3.4) is the most widely used model for describing the pressure drop in porous media [45].

$$\frac{\Delta P}{L} = \frac{\mu}{K}\mathrm{v} + \rho C v^2 \qquad \text{Eq. 3.4}$$

where *ΔP* is the pressure drop, *L* is the length of the sample, *μ* is the fluid viscosity, *C* is form drag coefficient and *K* is the permeability.

$$Re_k = \frac{\rho \mathrm{v}\sqrt{K}}{\mu}$$

Dybbs and Edwards [44,46] proved that above equation is applicable for packed beds of spheres in the range of 5<Re_k<80 (permeability based Reynolds number[44]). However, Lage et al. [44,47]showed that for Re_k higher than this range a cubic velocity expression should be used for an accurate description of pressure drop in metal foams.

$$\frac{\Delta P}{L} = \frac{\mu}{K}\mathrm{v} + \frac{\rho C}{K^{1/2}}\mathrm{v}^2 + c\mathrm{v}^3 \qquad \text{Eq. 3.5}$$

Here the permeability and the inertia coefficients are the same as those obtained over the low velocity range, the high velocity range only impacts the cubic coefficient *c.*

The permeability (*K*) and the from drag coefficient (*C*) are calculated by fitting a curve to the pressure data. One method of doing this is to use a least-squares quadratic curve through the pressure / fluid velocity data [42] or a least-squares cubic curve [47] depending on the maximum Reynolds number. Another method is to bring Eq. 3.4 into a linear form and then calculate the *K* and *C* with a linear least square fit. By dividing both sides of Eq. 3.4 by *L,* a linear form of this equation can be written as:

$$\frac{\Delta P}{L\mathrm{v}} = \frac{\mu}{K} + \rho C\mathrm{v} \qquad \text{Eq. 3.6}$$

By assuming the fluid viscosity and density remains constant, the first term can be replaced with *'a'* and *C* with *'b'*. Therefore Eq. 6 becomes a linear equation (Eq. 3.7). The permeability and the form drag coefficient can be extracted by fitting the pressure data into Eq. 3.7.

$$\frac{\Delta P}{L\mathrm{v}} = a + \rho b\mathrm{v} \qquad \text{Eq. 3.7}$$

It should be noted that this method is only valid for $5<Re_k<80$ and for higher Reynolds numbers the cubic law of Lage et al. should be used for data reduction. In this study both methods were applied to the pressure data.

3.2. Experimental apparatus and Procedure

The experimental setup shown in Fig. 3.1 was used to measure the pressure drop across the samples. It consisted of a fan, a test section, an orifice plate, two differential pressure transducers, a variable transformer (Variac), a data acquisition card and computer. For this experiment constant air flow was essential. Two 1000 W high speed centrifugal fans were placed inside a box to provide the suction power needed for the experiment, see Fig. 3.1 and Fig. 7.3a. The fan speed was controlled by adjusting the input current using an 8 Amp Variac variable transformer. It was found that at low current, the fan speed fluctuated and disturbed the flow rate. This was avoided by running the fans at high speed and controlling the flow by a ball valve connected to the box. The valve reduced the negative pressure inside the box lowering the suction power. To fine tune the flow rate the fans speed were adjusted with the Variac.

Air flowed through a 1500 mm two inch nominal size ABS pipe (internal diameter 52.9 mm and wall thickness 3.5mm) to ensure that it was fully developed before reaching a calibrated flanged-type orifice plate that was used to measure the flow rate. The orifice plate was calibrated against a manufacturer calibrated laminar flow meter (Cussons Technology P7250) and was found to have a discharge coefficient of 0.632 (max. error 0.5%). The calibration data is presented in Appendix 1. The pressure tappings and their position were compatible with BS EN ISO 5167-1 [48]. The pressure drop across the orifice plate was measured by a differential pressure transmitter (Furness Controls - Model 332-4W) with an accuracy of ±0.25% (reading). To calculate the flow rate, the air density was calculated from the atmospheric pressure, temperature and humidity. To calculate the air Humidity, a psychrometric thermometer was used to measure the air wet-bulb and dry-bulb temperature. The humidity result was cross checked by a digital humidity measuring device (VELOCICALC Models 8347(A)).

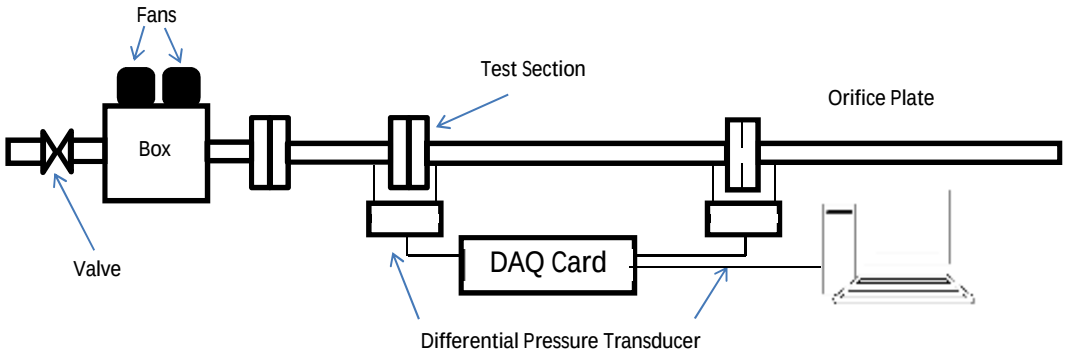

Fig. 3.1, A schematic view of the test rig for measuring steady state pressure drop

The pressure drop across the samples was measured with a differential pressure transmitter (Omega DPGM409DIFF- 350HDWU, 0.08% combined linearity, hysteresis and repeatability). The pressure loss of each sample was measured at 7 different flow rates and the measurement was repeated 20 times at each flow rate.

The test section could be separated from the rig by undoing the two flanges. The circumference of the samples were sealed by PTFE tape and pushed into the test section. Three small pins (2mm long) were placed evenly inside the test section to keep the samples in place. The effect of these pins on pressure drop was found to be negligible.

A 16-bit PCI-6221 National Instrument (NI) data acquisition card (DAQ) was used to receive the signals from two pressure transmitters. The DAQ card was connected to a PC running Windows XP. A code was written in LabVIEW software to control the DAQ card.

3.2.1. Tested Samples

In this experiment nine metal foams were manufactured with gas-only method and two other samples, a packed bed of 100 layers wire mesh (200 pores per inch and 0.041 mm wire diameter) and a packed bed of 10000 ball bearings (2mm). Samples physical properties were tabulated in Table 3.1.

Table 3.1 – Properties of the foams made by gas-only infiltration method.

Name	Grain size /pore size (mm)	Weight (gr)	Length (mm)	Diameter (mm)	Porosity
Small 1	1-1.18	51.7	24.7	51.1	0.62
Small 2	1-1.18	51.3	25.1	51.1	0.63
Small 3	1-1.18	57.8	25.7	51.1	0.59
Mid 1	1.4-1.7	49.9	23.8	51.1	0.62
Mid 2	1.4-1.7	52.0	26.5	51.1	0.64
Mid 3	1.4-1.7	48.7	24.5	51.1	0.64
Large 1	2-2.36	47.4	25.5	51.1	0.66
Large 2	2-2.36	48.8	25.3	51.1	0.65
Large 3	2-2.36	51.4	26.7	51.1	0.65
Wire mesh	0.041	50.4	12.1	52.9	0.70
Ball bearing	2	326.7	35.2	52.5	0.43

3.3. Results and Discussion

All the pressure data were calculated and reported based on Darcian flow velocity which was calculated by dividing the volumetric flow rate by the cross-sectional area. The pressure data were normalised by divided the data to the sample length. A quadratic and cubic curve was fitted through the data points for each sample and the permeability and the form drag calculated. The results from each method was presented and compared with other method. The goodness of fit was calculated in Excel from the following equation.

$$R - square = \frac{SSR}{SST} = \frac{\sum_{i=1}^{n}(\hat{y}_i - \bar{y})^2}{\sum_{i=1}^{n}(y_i - \bar{y})^2} \quad \text{Eq. 3.8}$$

Shown in Figure 3.2 is the experimental pressure-drop data for nine samples representing three pore sizes against Darcian velocity. Samples were tested for velocity of up to 6.1 m/s. This was the highest velocity which could be achieved and the pressure drop be measured for all the samples i.e. the maximum range of flow rate was achieved by the fans for the samples with the smallest pore size. The pressure-drop data for the samples with similar pore size had notably different values. The reasons for this scatter will be discussed in the last part of this chapter.

As it can be seen from Fig. 3.2 the sample with largest pore size had smaller pressure drop than the medium and small pore size samples. The pores of the Small samples were on average half the diameter of the pores of the Large samples. However, the pressure drop of the Small samples on average was 4.4 times higher (at 6.5 m/s velocity) than the Large samples.

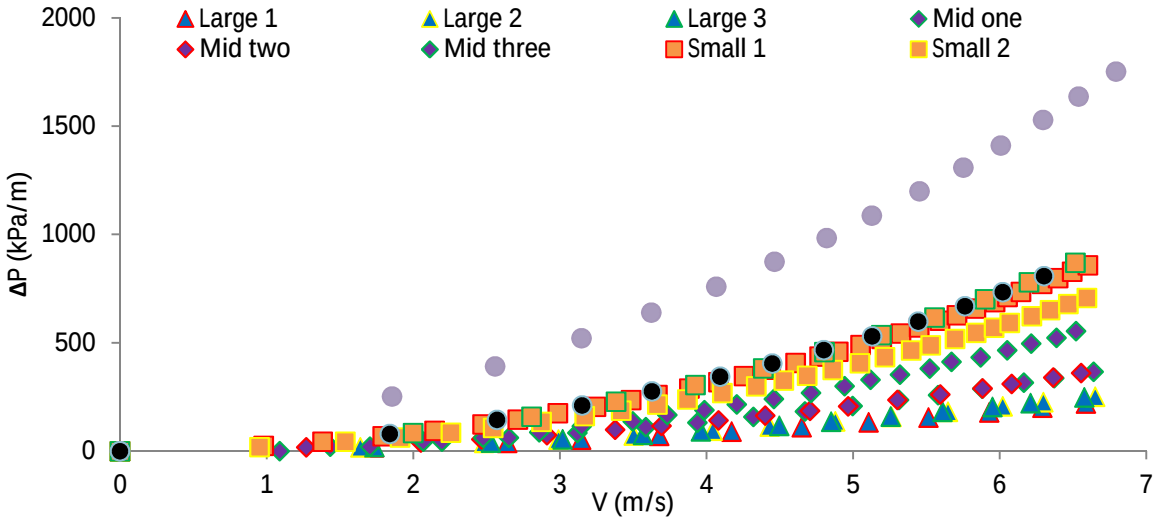

Fig. 3.2, Normalised pressure drop of 9 metal foams, wire mesh (No.200) and ball bearing (2mm diameter) against air velocity

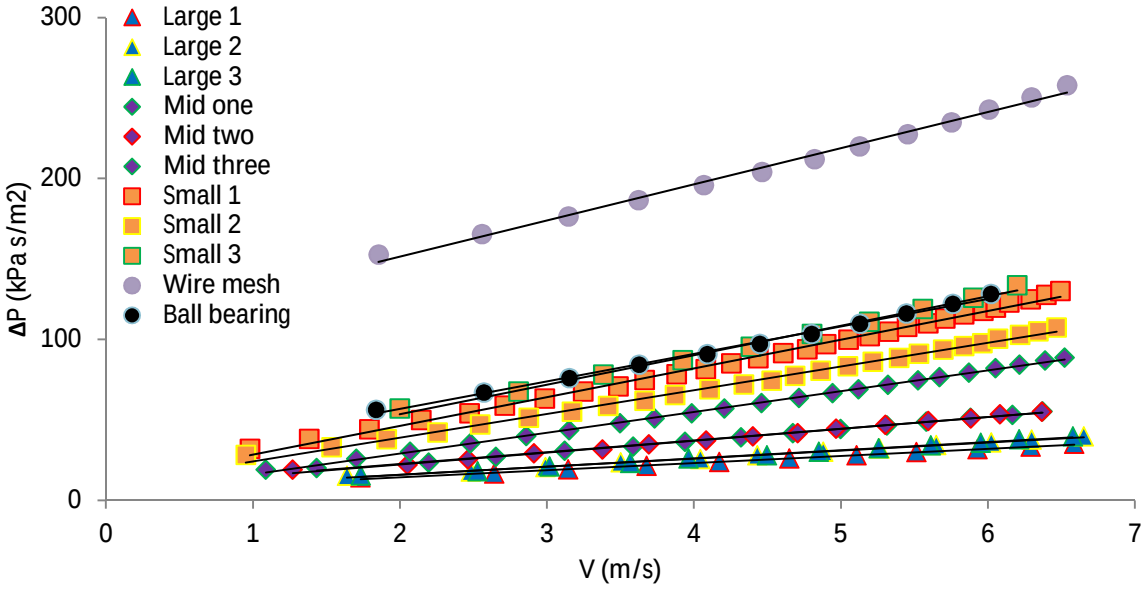

Fig. 3.3, Linearized pressure-drop data based on the Darcian velocity

For Fig. 3.3, the pressure data was linearized by dividing the normalised pressure data by velocity and a least-square line was fitted to each data set. The graph shows that the flow through the samples deviated from Darcy law flow and they were not changing linearly with velocity. In other words, the pressure drop across the samples should be fitted with a quadratic function.

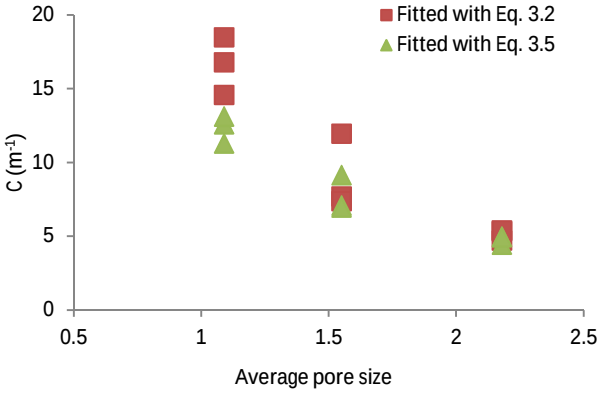

Fig. 3.4a, The form drag of the foams plotted against the values of average pore size.

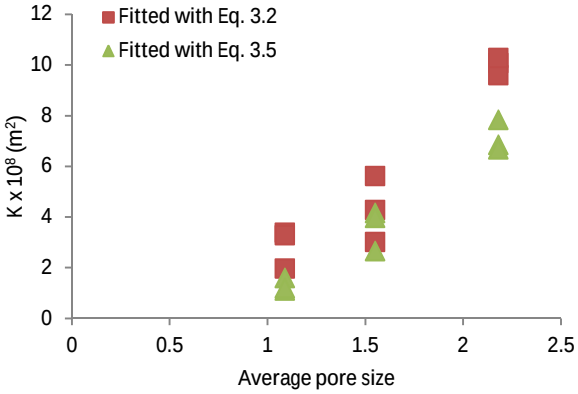

Fig. 3.4b, The permeability of the foams plotted against the values of average pore size.

By applying a linear-regression to the data the constants *a* and *b* can be determined from which the permeability and form drag coefficient were calculated, Table 3.2. The results shows that the average permeability increases with increasing pore size (Fig. 3.4b) and the form drag coefficient decreases by increasing pore size (Fig. 3.4b). It can be seen from Table 3.2 that by reducing the pore size (on average) by 30% the form drag increased by 1.7 times and by 50% reduction in pore size the form drag increases by 3.22 times. The wire mesh sample results shows that, *C* and *K* were higher than the foam results however the permeability of wire mesh was much lower than the Small samples. This may suggested that even for low velocity, wire mesh generate larger pressure drop compared to the foam but the rate of increasing was close to Small 3 sample. A packed bed of 2 mm ball bearing (51mm diameter and 35.2 mm length) was tested in this study. It generated similar pressure drop to the Small samples (small 1 and 3).

The results from the second method on average were lower than the results from the first method (Fig. 3.4a, 3.4b). In addition, Table 3.2 shows that the R^2 values reduced with the pore size. In other words, by reducing the pore size the data did not fit into a linear line.

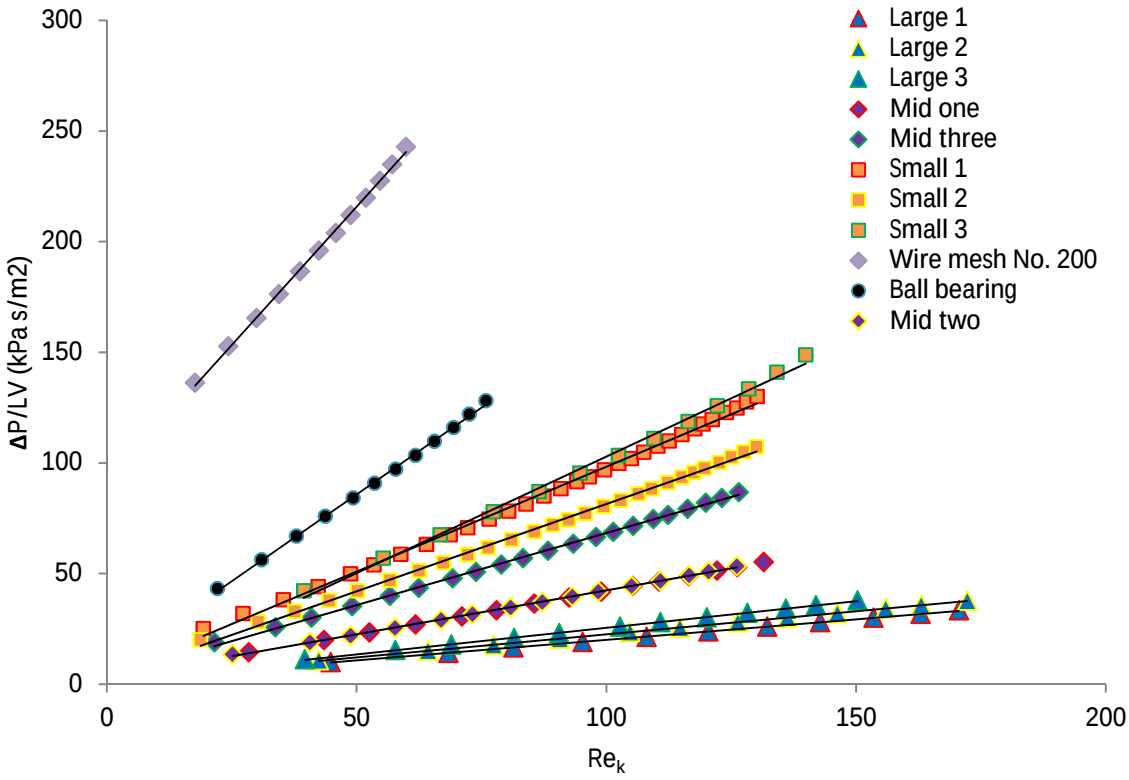

Fig. 3.5, Linearized pressure-drop data based on the Darcian velocity

Pressure drop data linearized and plotted against permeability based Reynolds number (Fig. 3.5). As can be seen from the graph, Reynolds number for metal foams was higher than 80. As it was discussed before, for a better fitting the second method should be used.

The second method was done by fitting a least-square cubic curve to the pressure data and calculating *K* and *C* from Eq. 3.5. The results were tabulated in Table 3.2. The samples with large pore size had the lowest difference for *C* value and highest for Mid samples. The difference for *K* value increased by decreasing the pore size but the wire mesh sample did not flow the same trend. Comparing the R^2 value in Table 3.2 and 3.3 shows that second method fitted better than the first method. The tables also show that the second method predicted consistently lower results for *C* and *K*. One of the reasons for this discrepancy could be the error of fitting a line through the data. R-square in Table 3.3 shows that the cubic curve fits better than the linear least-square line. Therefore, *K* and *C* predicted with the cubic curve fitting could be more accurate than the other fitting.

Table 3.2- Calculated permeability and form drag by fitting a least-square line.

Sample	*a*	*b*	$K \times 10^{8} (m^{2})$	$C \times 10^{-3} (m^{-1})$	R^{2}
Large 1	1.50	5.66	11.82	4.80	0.9999
Large 2	1.76	6.35	10.07	5.38	0.9998
Large 3	1.49	6.45	11.92	5.47	0.9998
Mid 1	2.76	9.25	6.45	7.84	0.9997
Mid 2	2.76	9.30	6.45	7.89	0.9994
Mid 3	3.31	15.21	5.37	12.90	0.9990
Small 1	2.78	18.29	6.39	15.51	0.9976
Small 2	3.68	22.04	4.82	18.69	0.9981
Small 3	2.82	23.66	6.31	20.067	0.9963
Wire Mesh	92.99	24.21	0.19	20.54	0.9992
Ball bearing	7.37	18.88	2.42	16.01	0.9991

Table 3.3 - Calculated permeability and form drag by fitting a least-square cubic curve.

Sample	c	B	A	$K \times 10^{8} (m^{2})$	$C \times 10^{-3} (m^{-1})$	R^{2}
Large 1	0.05	5.23	2.27	7.84	4.43	1
Large 2	0.06	5.87	2.60	6.86	4.98	1
Large 3	0.08	5.80	2.67	6.67	4.92	1
Mid 1	0.12	8.34	4.28	4.16	7.07	1
Mid 2	0.15	8.19	4.49	3.97	6.95	1
Mid 3	0.27	10.77	6.69	2.66	9.13	1
Small 1	0.93	14.85	16.09	1.11	12.59	0.9999
Small 2	0.65	13.30	11.14	1.60	11.28	0.9999
Small 3	1.01	15.46	15.02	1.19	13.11	0.9999
Wire Mesh	1.00	15.23	110.10	0.16	12.91	0.9997
Ball bearing	0.39	15.63	13.37	1.33	13.26	0.9999

3.4. Data scattering in pressure data

As can be seen from Fig. 3.2, samples with the same pore size generate different pressure drops. There are several factors affecting the pressure drop of metal foams manufactured by replication process especially as the structure of the foams were random (due to unstructured (random) salt particles position inside the mould prior infiltration). This randomness affects the pressure-drop across this type of metal foams. Ergun [35] stated that pressure drop through a packed bed depends on:

1- Rate of fluid flow
2- Viscosity and density of the fluid,
3- Closeness (fractional void volume) and orientation of packing
4- Size, shape, and surface of the particles

The first two are fluid related and the last two are related to the sample and will be discussed in this section.

Ergun studied the effect of fractional void on pressure drop and concluded that total energy losses in fixed beds are equal to the sum of viscous and kinetic energy losses. He showed that viscous energy losses were proportional to $(1-\varepsilon)^2/\varepsilon^3$ and the kinetic energy losses to $(1-\varepsilon)/\varepsilon^3$. He argued that Eq. 3.3 could be rewritten such that:

$$\frac{\Delta P}{L} = \acute{a}\frac{(1-\varepsilon)^2}{\varepsilon^3}\mathrm{v} + \acute{b}\frac{1-\varepsilon}{\varepsilon^3}\rho \mathrm{v}^2 \qquad \text{Eq. 3.10}$$

As it can be seen from Eq. 3.10 the fractional void volume has both second and third-power terms and any variation would have a large effect on pressure drop. For instance Ergun showed that for crashed material the most tightly packed bed having a height of 30 cm could easily be expanded by 6 to 7 cm. This could be one of the reasons of pressure drop data scattering. Porosity of the metal foams could be increased by increasing the preform packing density. The packing density depends on several factors such as shape of the particles (crushed or spherical), friction factor between particles, density of the particles, the ratio of particle diameter to the container diameter and many other factors which are beyond the scope of this study and did not investigated for this study.

3.5. Effect of infiltration pressure on samples pressure drop

Eight samples of increasing infiltration pressure (2.5 bar to 7 bar, pore size 1.4-1.7 mm) were manufactured. Samples properties were tabulated in Table 3.4. Fig. 3.6 shows the normalized pressure drop of the samples against the Darcian velocity. Samples made under 4.5 bar had lower pressure drop but they were non-homogenies and were only partly infiltrated. For sample with infiltration pressures higher than 4.5 bar were uniform and fully infiltrated. However, by increasing the infiltration pressure samples became denser and the

pressure drop increased. Since having low pressure drop and high surface area (fully infiltrated samples) are essential for high performance regenerators; the results from this experiment were used to estimate the optimum infiltration pressure for manufacturing the samples for this study. As it was explained in chapter two (section 2.4.2), 4.5 bar pressure was used for manufacturing samples with pore size of 1.4-1.7mm based on the results from this experiment.

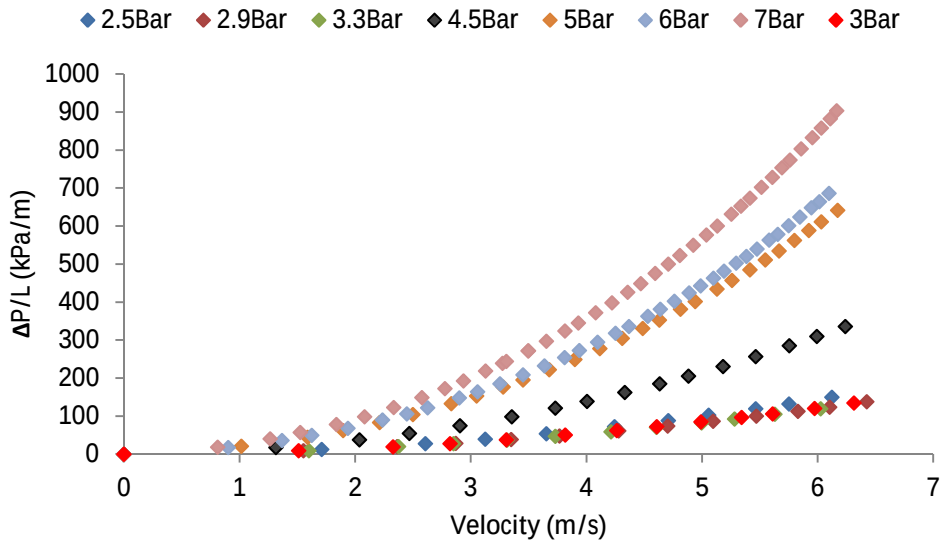

Fig. 3.6, Pressure-drop versus fluid flow velocity for samples made under different infiltration pressure.

Table. 3.4 – Material properties of the samples manufactured under various infiltration pressures.

Sample Name	Weight (gr)	Length (mm)	Dia (mm)	Volume (mm^3)	Porosity
2.5 bar	55.4	32.0	51.1	65626.9	0.69
2.9 bar	44.9	24.8	51.1	50758.3	0.67
3.0 bar	45.9	26.5	51.1	54347.2	0.69
3.3 bar	47	27.0	51.1	55372.7	0.69
4.5 bar	49.1	25.6	51.1	52419.5	0.65
5.0 bar	57.7	27.3	51.1	55987.9	0.62
6.0 bar	71.9	34.2	51.1	70036.2	0.62
7.0 bar	60.9	28.5	51.1	58448.9	0.61

Chapter 4 - Oscillatory pressure drop in metal foam

The optimum design of a regenerator depends on the accuracy of the predicted pressure drop and thermal performance of the regenerators [49]. Early researchers used unidirectional friction factor correlations to estimate the pressure drop through regenerators. However, it has been found that pressure drop in oscillatory flow is different from unidirectional flow and factors such as the fluid displacement amplitude could affect the pressure drop in regenerators[49]. The majority of the studies have been done on wire mesh regenerators. Metal foams have not been tested to same extent and most of those studies were focused on high porosity (90%) foam [20,50,51]. To the knowledge of the author, foams made with the replication process with porosities of less than 90% have never been tested for pressure drop under oscillatory flow. The aim of this chapter is to discuss the pressure drop in oscillatory flow and present the experimental method used in this study to measure the pressure drop and flow velocity under oscillatory conditions.

4.1. Pressure drop and velocity profile inside a pipe

The pressure drop in oscillatory flows has been studied for nearly 100 years. These studies have been focused on two main areas; inside a pipe (or duct) and in packed beds (or regenerators). Although the nature for pressure drop inside a pipe is different from regenerators, it helps to understand the pressure drop mechanism in regenerators. Therefore, in the section, velocity profile and pressure drop inside a pipe under oscillatory flow will be discussed and this will be continued for regenerators.

As early as 1929 it was recognised that the velocity profile in a reciprocating flow was different to that for unidirectional flow down a pipe. Richardson and Tyler [52] experimentally investigated oscillatory flow in a pipe and they discovered the “annular effect”. In an oscillatory flow, velocity profiles constantly change with the crank angle. During the first quarter cycle, a viscous layer caused by the wall friction grows in thickness and the velocity profile changes from a rectangular to a parabola-like shape. On the next quarter cycle, flow starts to decelerate and because of inertial effects, the velocity profile becomes flatter at the centre and overshoots near the wall (the annular effect)[53].

In oscillatory flow, because of the annular effect, flow is more "like a turbulent flow" during the deceleration phase [54]. It seems that this type of flow behaviour could dissipate more energy and consequently, increases the friction factor during the deceleration phase in oscillatory flow. Isshiki et al. experimentally showed that the friction factor in a decelerating period was higher than that in the accelerating period [55]. Beside the deceleration effect, by increasing the frequency or kinetic Reynolds number, the "annular effect" becomes higher and thus the radial velocity gradients near to the pipe wall became steeper. As a result, friction factor increases with oscillation frequency.

In addition to oscillation frequency, oscillation amplitude influences onset of turbulence in oscillatory flow [56]. For instance, if we assume bore diameter of two pistons are the same but one has a long stroke and other has a short stroke. The oscillating flow inside the pipe would behave differently at the same oscillation frequency for these pistons. Zhao and Cheng [57] showed that flow at kinetic Reynolds number of 302.2 and dimensionless oscillation amplitude of 21.4 exhibited a laminar flow but by only changing the amplitude to 97.1 the flow behaved like a turbulent flow. They defined the dimensionless oscillation amplitude as:

$$x_{max} = \frac{V_p}{A_{cs}} \qquad \text{Eq. 4.1}$$

$$A_{OA} = \frac{x_{max}}{D_h} \qquad \text{Eq. 4.2}$$

where, V_p is the piston swept volume, A_{cs} is the cross section area of the connecting pipe and D_h is the hydraulic diameter of the pipe. In equation 1, x_{max} is the maximum fluid displacement or maximum distance that fluid can travel inside the pipe.

4.2. Pressure drop in regenerators

Similar to oscillatory flow in a pipe, pressure drop was reported higher than unidirectional flow in regenerators. Tanaka et al. [20] measured pressure drops for frequencies up to 10 Hz and their results were higher than unidirectional flow results for a given Reynolds number. They also conducted a similar experiment with a pipe bundle (8370 pipes, inner diameter of 0.22 mm and outer diameter of 0.4 mm) and reported 30% higher pressure drop than the

value for unidirectional flow. Zhao and Cheng [49] did a similar experiment for frequencies between 1/3Hz and 9Hz and reported that the cyclic-average pressure drop was 4 to 6 times higher than a steady flow at the same Reynolds number (based on the cross sectional mean velocity). More recently, Ju et al. [58] experimentally measured the pressure drops and the phase shift characteristics for five different regenerators made of wire-mesh screens. They obtained a correlation equation of the friction factor for a 50Hz oscillating flow and reported pressure drops two to three times higher than that for steady flow at the same Reynolds number (cross-sectional mean velocity).

A number of workers have shown that at low frequencies the maximum pressure drop in the reciprocating case is the same as that for the unidirectional situation. For instance, Gedeon and Wood [59] measured the pressure drop under oscillatory flow conditions and compared their results with the unidirectional flow result (1-120Hz). They found that their results were similar within their frequency range. In other work, Hsu [60] measured pressure drop of wire mesh (Table 4.1) under oscillatory up to 4.0 Hz and also steady flow, and reported no difference between the results.

Table 4.1 Properties of the wire mesh and packed columns [60]

Mesh Size(No.)	Pitch distance (mm)	Wire diameter (mm)	Porosity	Hydraulic diameter (mm)
20	1.243	0.32	0.792	1.213
30	0.849	0.22	0.788	0.8263
40	0.613	0.224	0.694	0.509

It has been reported that the dimensionless oscillating amplitude also affects the pressure drop in oscillatory flow. For instance, Zhao and Cheng [49] used a yoke sinusoidal mechanism to adjust the fluid displacement and reported that the pressure drop not only depends on the shape and structure of the sample but also on the kinetic Reynolds number and dimensionless oscillating amplitude A_{0A}. They compared their data with Tanaka et al. [20] correlation equations argued that Tanaka's data were only applicable to a limited range of dimensionless oscillating amplitude of 145.

In oscillatory flow the maximum pressure drop occurs at 90^o phase angle but it became increasingly delayed as the frequency went up. Zhao and Cheng reported significant phase lags for higher values of the kinetic Reynolds number ($Re_\omega = \omega D_h/\nu$). For example, the

phase angle lagged by 18° at $Re_\omega = 0.03770$ and lagged by 24° at $Re_\omega = 0.05529$. However, they observed that phase lag was relatively independent of A_{0A}[49].

4.3. Air velocity measurement

In order to present the pressure drop data, cross-sectional mean velocity was estimated based on piston's swept volume and angular velocity of the crank shaft. In addition to this, air velocity was measured with Hot-wire anemometer for studying the fluid behaviour under the oscillatory condition. The fluid velocity was only measured at the centre of the pipe with Hot-wire anemometer. These two methods will be discussed further in this section

4.3.1. Cross-sectional mean velocity estimation

By assuming that the oscillating air in the pipe is an incompressible fluid and the flow motion is driven by a sinusoidal displacer, the cross-sectional mean velocity u_m can be calculated using:

$$u_m = u_{max}\sin(\varphi) \qquad \text{Eq. 4.3}$$

where φ is the phase angle of the cross-sectional mean velocity, and is related to the oscillatory angular frequency ω. The maximum mean cross-sectional velocity depends on the maximum fluid displacement x_{max} and oscillatory frequency which can be calculated by [56]:

$$u_{max} = \frac{x_{max}\omega}{2} \qquad \text{Eq. 4.4}$$

x_{max} can be calculated from Eq. 4.1.

4.3.2. Hot-wire anemometer

Hot-wire anemometer (HWA) is one of the key methods for measuring fluid velocity under rapid motion. The main advantages of conventional HWA for this experiment are:

1- Low Cost – Hot-wire systems are relatively cheap in comparison with laser based techniques.

2- High frequency response – Constant Temperature (CT) anemometers can achieve up to 20-50 kHz [61].
3- Small size – A typical size of the hot-wire probe is about 5 μm and can be placed easily inside a narrow pipe.
4- High accuracy – This system can achieve accuracy of 0.1% to 0.2% in careful controlled experiments and 1% for practical applications [61].

HWA is based on the changes in the convection heat transfer from a heated wire which is placed in a fluid. The heat transfer rate between a high temperature surface and a low temperature moving fluid is proportional to temperature difference, heat transfer coefficient, *h*, and surface area. The heat transfer coefficient increases with fluid velocity reflecting the increased the heat transfer rate. The heat transfer relationship between the hot-wire and the fluid for both infinitely long and finite length wire element have been derived [61].

The changes in heat transfer coefficient are detected by monitoring changes in the wire resistance. The hot-wire probe is connected to a Wheatstone bridge circuit as illustrated in Fig. 4-1. The relationship between the hot wire resistance, R_w, and the mean wire temperature, T_w is provided by Eq. 5[62].

$$R_w = R_0[1 + \alpha(T_w - T_0)] \qquad \text{Eq. 4.5}$$

where R_0 is a reference resistance measured at temperature T_0 and α is the temperature coefficient. The reference temperature is often selected as room temperature (20 ºC) and adding the probe lead, support and cable resistances the Eq. 5 can be rewritten as

$$R_T = R_{lead} + R_{support} + R_{cable} + R_{20}\alpha_{20}(T_s - T_{20})] \qquad \text{Eq. 4.6}$$

The mean sensor temperature,T_w, can be estimated by measuring the sensor resistance. In order to heat the sensor a current is passed through the wire. The temperature adjustment of the wire is called overheat adjustment and has an effect on response time of the HWS (see Section 4.3.2.1). The relationship between the heat transfer rate from the sensor to the cooling fluid velocity is given by King's law [62,63] as

$$\dot{Q} = I^2R = A + BU^n \qquad \text{Eq. 4.7}$$

where *A*, *B* and *n* are empirical constants that depend on the fluid, operating temperature, and sensor physical properties and dimension [62]. The coefficients in Equation 4.7 are obtained by calibration which will be discussed in Section 4.3.2.2.

There are three types of operating mode for the anemometers: Constant Current (CC), Constant Temperature (CT) and Constant Voltage (CV). The two most common types of HWA are Constant Temperature (CT) and Constant Current (CC). The CT mode maintains the hot-wire at constant operational temperature and as a result at a constant hot resistance [61]. In this mode the thermal inertia of the sensor element is automatically adjusted and therefore has a faster frequency response than CC [61]. Thus CT is generally adopted for the rapid flow measurements.

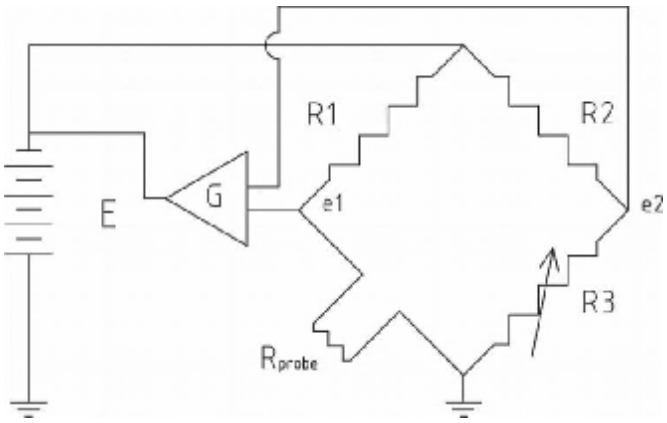

Fig. 4-1, A diagram of a CT anemometer Wheatstone bridge with feedback amplifier.

Fig. 4-1 illustrates the principle of a CT circuit which consists of a Wheatstone bridge, how-wire probe and differential amplifier. The fluid passing over the sensor varies the error voltage e_2-e_1 which is a measure of the corresponding change in the wire resistance. The error voltage forms a feedback to a differential feedback amplifier. The amplifier feeds an output current, *i* (*i* is inversely proportional to the resistance changes of the sensor) back to the top of the bridge to restore the sensor's resistance (temperature) to its original value [61]. The instantaneous power (I^2R_s) required to maintain the sensor's temperature is equal to the rate of heat transfer from the sensor (Eq. 4.7). The fluid velocity then can be found

(Eq. 4.8) by knowing the instantaneous applied bridge voltage, *E,* which is required to keep the sensor at constant resistance.

$$E^2 = A + BU^n \qquad \text{Eq. 4.8}$$

The resistance ratio R_2/R_1 is called the bridge ratio. The bridge configuration can be selected based on required bandwidth, power to the probe and the distance between the probe and CT anemometer [64]. The resistance on the right-hand-side of the bridge is normally larger than the other side in order to utilise the available current from the amplifier[61]. O'Dea and Fleming [65] studied the sensitivity and precision of the Wheatstone bridge and concluded that a bridge ratio of 1 gives the maximum sensitivity and zero ratio provides the highest precision. For the current experiment the bridge ratio of 1:20 or 0.05 was a default setting and had 5% departure from highest precision possible. This error was negligible for measuring the mean velocity of oscillating air for this experiment.

4.3.2.1. Overheat calculation

For setting up the anemometer an overheat adjustment (static bridge balancing) and a square wave test (dynamic balancing) should to be done prior to the test. The anemometer (DANTEC 54T30) used in this experiment did not have the option for the square wave test, so only the overheat adjustment was done here. However, the manufacturer reported 5-10 kHz frequency response for the anemometer which was sufficient for this study.

The working temperature of the sensor can be determined by adjusting the overheat ratio, R_w/R_{20}. This was done by adjusting the decade resistor, R_3. The resistors R_w (sensor resistor at desirable working temperature) and R_{20} (sensor resistor at 20°C) are related via the overheat ratio, *a* [64]:

$$a = \frac{R_w - R_{20}}{R_{20}} \qquad \text{Eq. 4.9}$$

The temperature difference between T_w and T_{20} (over temperature) can be calculated as:

$$T_w - T_{20} = \frac{a}{\propto_{20}} \qquad \text{Eq. 4.10}$$

where $\propto_{20}$ is the sensor temperature coefficient of resistance at T_{20}.

In this experiment the hot-wire probe specification was provided by the manufacturer:

$$R_{20} = 3.33\ \Omega,\ R_{lead} = 0.9\ \Omega,\ R_{cable} = 0.2\ \Omega,\ R_{support} \approx 0.0\ \Omega,\ \alpha_{20} = 0.0036\ /^{o}C$$

The recommended overheat ratio was 0.8 giving an operating temperature of T_w=242 ºC for air. Based on Eq. 4.6, the total resistance was:

$$R_T = 0.9 + 0.2 + 3.33[1 + 0.0036(242 - 20)] = 7.09\ \Omega$$

Since the bridge ration is 1:20, the decade resistance was set at:

$$R_3 = 20.R_T = 141.8\ \Omega$$

4.3.2.2. Hot-wire calibrator and operating principles

The relationship between the output of the anemometer *E* and *V* the velocity component in the mean-flow direction is:

$$E=F(V) \qquad \text{Eq. 11}$$

The purpose of a calibration is to obtain a set of calibration points (*E* and V*)* over the required velocity range. This involves placing the probe in a flow of known velocity and measuring *E* for the minimum of 10 velocities. To determine the calibration constants a least-squares curve-fitting method was applied (Fig. 4-3).

A YSI 1125 calibrator was used to calibrate the hot-wire. A schematic is shown in Fig. 4-2. Dry compressed air was supplied to the calibrator. The calibrator had an internal heat exchanger with auxiliary fan and flow control valve to adjust the air flow. The air temperature reached the ambient temperature by passing it through the heat exchanger and the air temperature was measured by a K-type thermocouple placed inside chamber 1. The temperature was required to calculate the air density and compensate the hot-wire calibration if it deviated from the overheat adjustment. Air pressure was measured by a

differential micro-manometer (Furness FC0510) which had a range of 0.00 Pa to 2383 Pa and an accuracy of ±0.0002 Pa. The manometer was calibrated by the manufacturer and was valid during the experimental period.

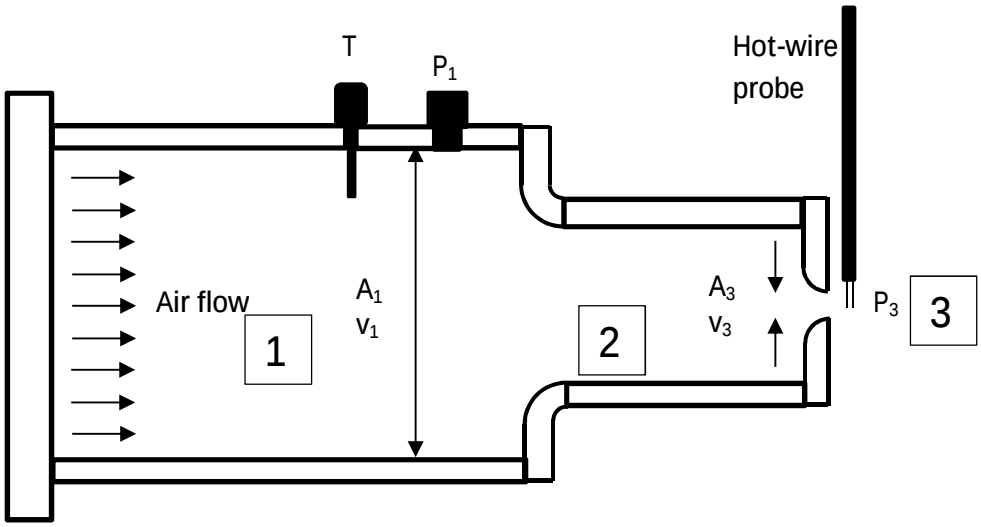

Fig. 4-2, A schematic view of YSI 1125 calibrator.

The calibrator had three chambers that permitted the user to calibrate over three ranges of velocities. In this work a velocity range from 1.5 ms^{-1} to 300 ms^{-1} was used.

The velocity can be calculated using Bernoulli's equation between section 1 and section 3.

$$P_1 + \frac{1}{2}\rho v_1^2 + \rho g H_1 = P_3 + \frac{1}{2}\rho v_3^2 + \rho g H_3 \qquad \text{Eq. 4.12}$$

By applying the law of continuity to section 1 and 3 we have:

$$v_1 A_1 = v_3 A_3 \qquad \text{Eq. 4.13}$$

The diameter of section 1 is 72 mm and for section 3 is 3.8mm. By assuming that the maximum velocity in section 3 is 30 ms^{-1}, we have:

$$v_1 = \frac{v_3 A_3}{A_1} = \frac{30 \times 3.61}{1296} \approx 0$$

Point 3 is about one diameter (3.8 mm) downstream from the nozzle and the static pressure of that point is equal to the atmospheric pressure. Therefore, by measuring the

corresponding total pressure (P_T=P_1-P_3) which is equal to the stagnation pressure at point 3 and assuming that *H* is 0, the velocity at point 3 can be calculated from:

$$v_3 = \sqrt{2P_T\rho} \qquad \text{Eq. 4.14}$$

In order to achieve a good accuracy with hot-wire anemometry, it is important to minimise any calibration errors and select an appropriate curve fit. King's law (Eq. 4.8) [63] has been used extensively to characterise the relationship between the fluid velocity and the anemometer output. With this method, it is necessary to carry out an inversion process to obtain the required velocity [61]. However, the hot-wire relationship expressed in the form *v=F(E)* can be used to obtain velocity directly. George et al. [66] introduced a polynomial equation for hot-wire relationship as:

$$v = A + BE + CE^2 + DE^3 + \cdots \qquad \text{Eq. 4.15}$$

The accuracy of a polynomial fit was investigated by Bruun [61] and he suggested to apply either a full fourth-order polynomial in *E* or a third-order in E^2 for best accuracy. Here a fourth-order polynomial fit was used and is shown in Fig. 4-3. In this graph *R* is R-square value of the fit, where a value closer to 1 indicates a better fit.

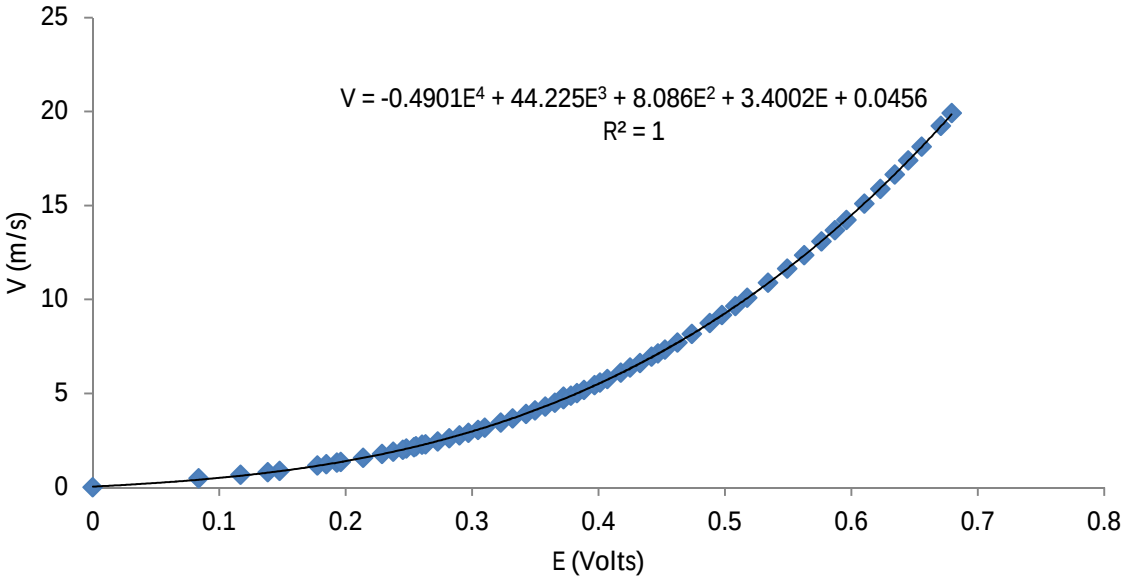

Fig. 4.3, Hot-wire calibrating curve with polynomial equation and fitting R-square value.

As a result of small fluctuations in the velocity during calibration and the electronic noise, the values of *V* and *E* for each point were measured over 10 s interval. The data was logged at 100 Hz.

4.4. Experimental set-up

From the literatures it can be seen that two methods, double-acting air pump [20,49,51,60,67]and a single cylinder compressor[52,58,59,68], have been used to generate oscillatory flow. One method uses a double-acting air pump to push and pull the air through the sample. This method is popular since it generates exactly 180^{o} phase different between the pushed and pulled air. Another advantage of this method is the possibility of adjusting the fluid displacement. However, because of dynamically unbalancing of this mechanism it is difficult to achieve high frequency.

The other method is using a single cylinder compressor to generate oscillatory flow. This method is simple and high frequencies can be achieved but it has the limitation of fixed fluid displacement. In addition, this method does not replicate the oscillatory flow in Stirling engines since there is no mechanism to push the air while the compressor pulls it and vice versa. In this method atmospheric pressure works as a large buffer tank that helps to push the air through the sample while the compressor pulls it.

In this study, two twin-cylinder compressors were connected via a toothed belt to generate high frequency oscillatory flow. A twin-cylinder compressor has 90^{o} phase different between the pistons. Therefore, the compressors were adjusted to have 180^{o} phase angle. Despite the best effort to synchronise the compressors, a slight phase difference always existed which affected the pressure results. Even after careful synchronising the compressors, slight tension in the toothed belt could change the phase difference between them. Therefore, this method was abandoned and a single twin-cylinder compressor was used for this study.

The test rig (Fig. 4.4) consisted of two V-type twin-cylinder compressor (Clarke CE20-91cc swept volume), a 1 kW three phase AC motor, hot-wire anemometry system, pressure transducer and the test section. The compressor and the motor were coupled by a toothed belt and two pulleys. The motor speed and torque were controlled by a variable-frequency-

drive controller (VFD) (Mitsubishi FR-D700). The test section in which the sample was held was a copper pipe (52 mm internal diameter and 80 mm length). It was connected to the compressor via a copper reducer and 600 mm length copper pipe (internal diameter 20 mm). A 5 µm hot-wire probe (DANTEC 55P16) was mounted at the middle of the connecting and positioned at the centre of the cross section of the pipe to measure the flow velocity. As the swept volume of the compressor was 91 cc, the maximum distance the air inside the compressor could travel inside the 20 mm pipe was 300 mm and this was where the hot wire probe was placed.

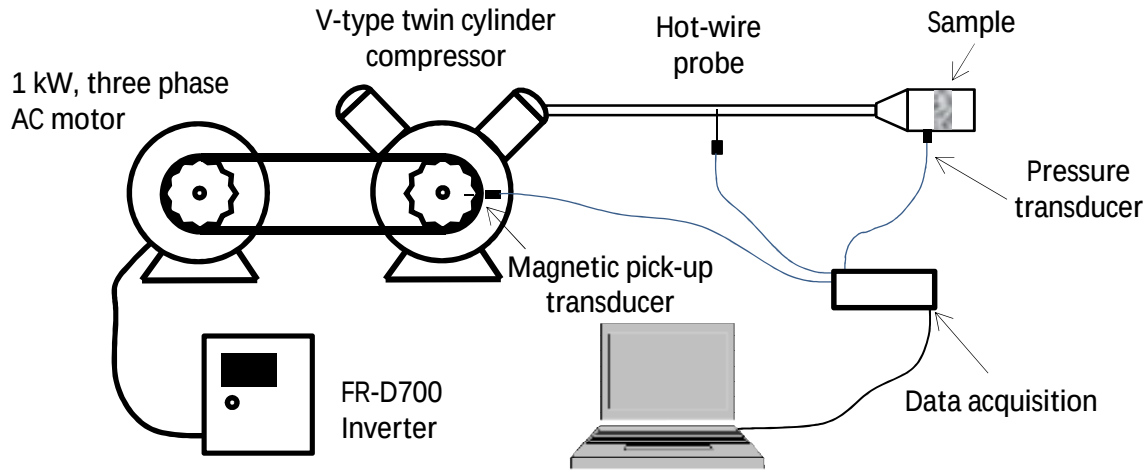

Fig. 4.4, Oscillatory test rig for measuring pressure drop and flow velocity.

A pressure tap was placed 10 mm before the sample and a high-frequency pressure transducer (Kulite ETM-375-100GS) installed. A 16 bit data accusation card (DAQ) (National Instrument PCI-6221) was used to log the data and a LabView code was developed to communicate with the DAQ card and also process and analyse the data.

In order to measure the pressure drop, samples were placed inside the tube between two thin rings used to hold the sample in place. The rings had three screws which were positioned every 120° from each other and were used to fix the rings. The circumference of the sample was wrapped with PTF tape to prevent air leakage. To place the sample inside the tube, first, one of the rings was inserted inside the pipe and tightened. Then the sample inserted into the tube. After that, the second ring slid into the pipe and tightened.

After fixing the sample in the tube, the frequency of the electric motor was adjusted with the converter. Once the motor reached the required speed, the signals from the pressure transducer, thermocouple and the hot-wire probe were recorded by the DAQ. The sample rate and sampling time were adjusted for each motor frequency to ensure the whole cycle data was recorded with sufficient data points. The magnetic pick-up triggered the DAQ card when the compressor's piston reached the top-dead-centre to ensure that DAQ card recorded the data at top-dead-centre (TDC). As a result, data was recorded from beginning of each cycle. The time that it took to complete each cycle was used to calculate the compressor running frequency. This time was divided into 360 segments to represent crank angle degree.

4.5. Velocity measurement system

The HWA used to measure the air velocity in the rig consisted of a probe with probe support and cabling, CTA anemometer and a signal conditioner, a data acquisition card (A/D board) and a computer (FIG. 4.5). The analog signal from the anemometer was converted to digital signals by the DAQ card and analysed and stored in the computer.

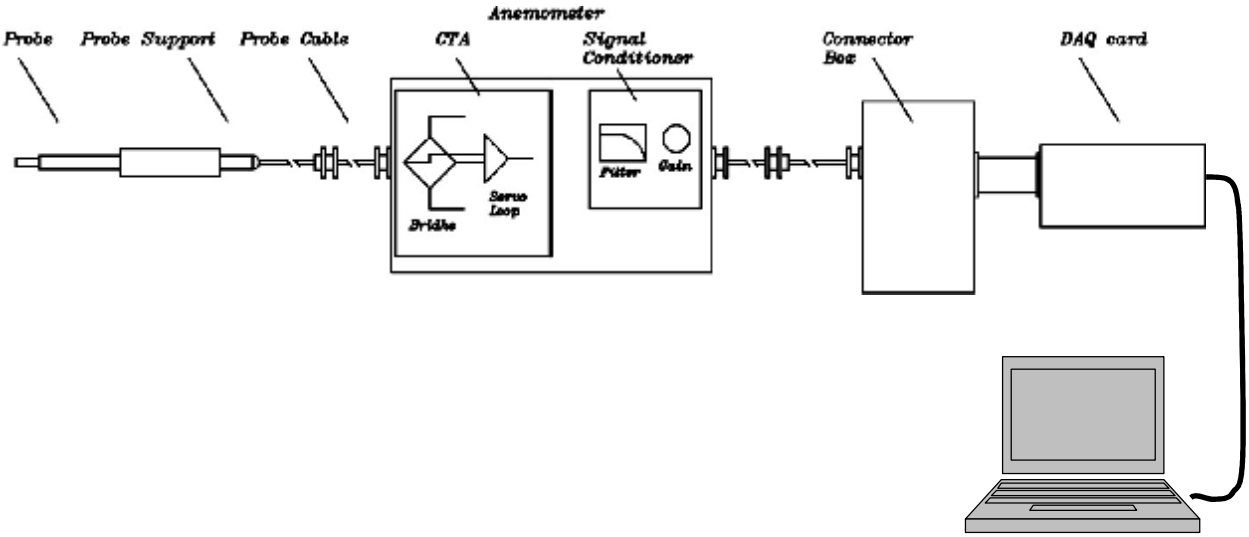

Fig. 4.5, The hot-wire measuring system.

The probe holder, showed in Fig. 4.6, consisted of a modified 20 mm brass Tee fitting. A piece of brass bar was soldered into the Tee then drilled and threaded to hold the fitting. The empty space inside the Tee was filled with plastic and a drill hole was made to pass the

hot-wire probe. This minimised any flow disruption through the Tee. A technique was developed to position the probe at the centre of the Tee. Both sides of the Tee were covered by two caps which had a small hole at the centre. The probe was then slid into the Tee till the probe and two holes visually lined up.

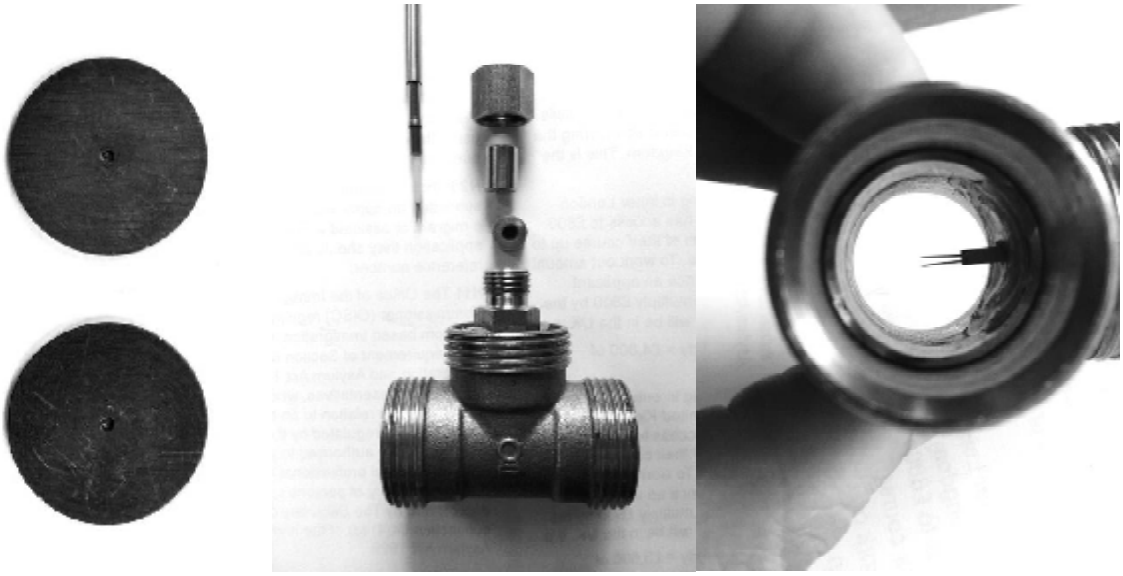

Fig. 4.6, Hot-wire probe holder and caps for positioning the probe.

It was found that small dust and fibres floating in the lab air contaminated the hot-wire probe and affected both the calibration value and frequency response. On some occasions the fibres were so entangled that cleaning of the probe became impossible without damaging it. To avoid contaminating the probe, a fine gauze mesh was placed after the test section and the compressor to filter the air going into the measurement length.

Chapter 5 - Oscillatory flow data

5.1. Pressure drop

In this chapter the experimental results for the pressure drop across the samples subjected to a periodically reversing flow are presented. Experiments were carried out for the nine metal foam samples and wire mesh sample at frequencies ranging from 1.1 to 19 Hz. Pressure and velocity were measure for 20 cycles at each frequency and results were averaged.

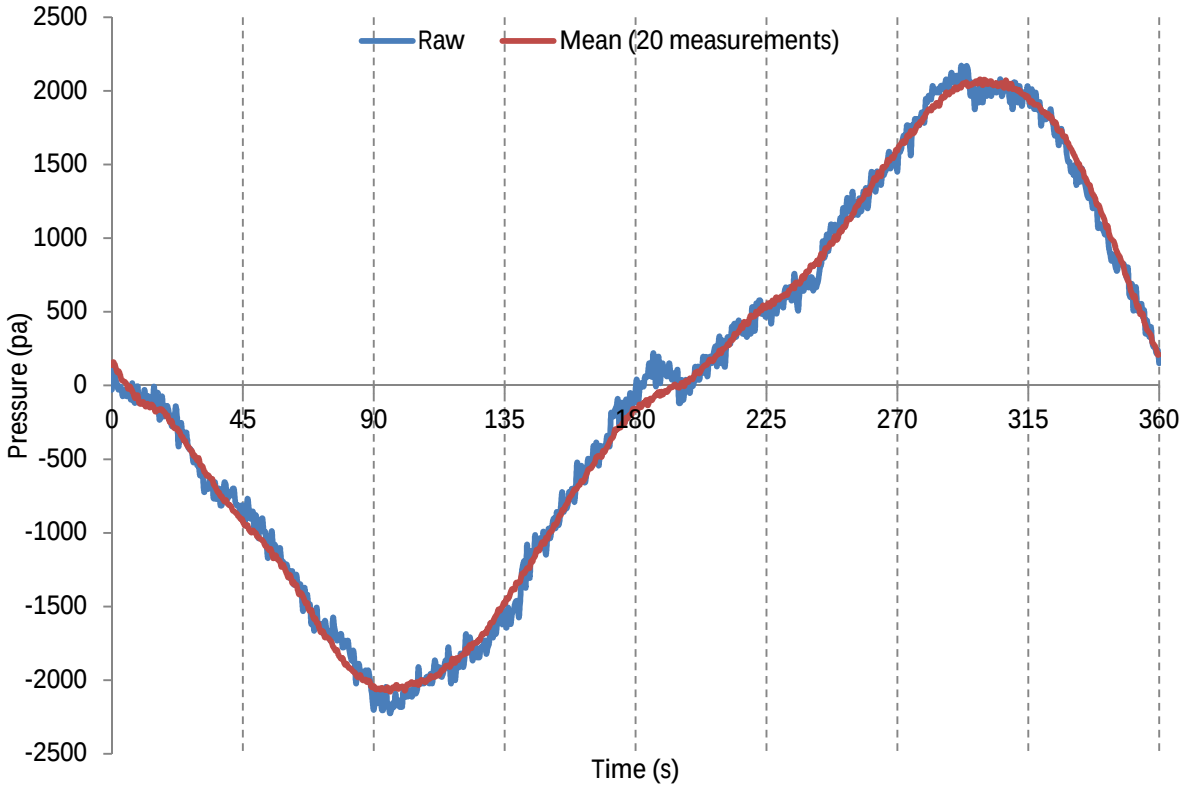

Fig. 5.1, Raw and averaged pressure drop of Sample 1 at 14 Hz.

In this experiment the DAQ card was trigged at pistons top-dead-centre and pressure data, hot-wire data and time were logged for a full cycle. Since the rig didn't have a shaft encoder to record the crank angle, the time of each complete cycle was measured (from top-dead centre to next top dead-centre) and converted to 360°. To do this conversion, it was assumed that compressor was running at a constant speed. The time for completing each cycle was divided to 360 to calculate the time for completing each degree crack angle. In Fig.

5.1 the blue line is a raw pressure data for a complete cycle and the red line is the average pressure data of 20 measurements.

Shown in Fig. 5.2 is the averaged pressure drop for sample Mid 3 at various frequencies plotted against crank angle. This graph shows that increasing the frequency resulted in increased pressure drop. The profile of pressure drop for frequencies lower than 14 Hz were nearly sinusoidal due to the reciprocating motion of the piston. At higher frequencies the pressure drop profile became unsymmetrical notably where the piston accelerated (before 90^o). Similar trends were observed for the second half of the cycle between 180^o and 270^o.

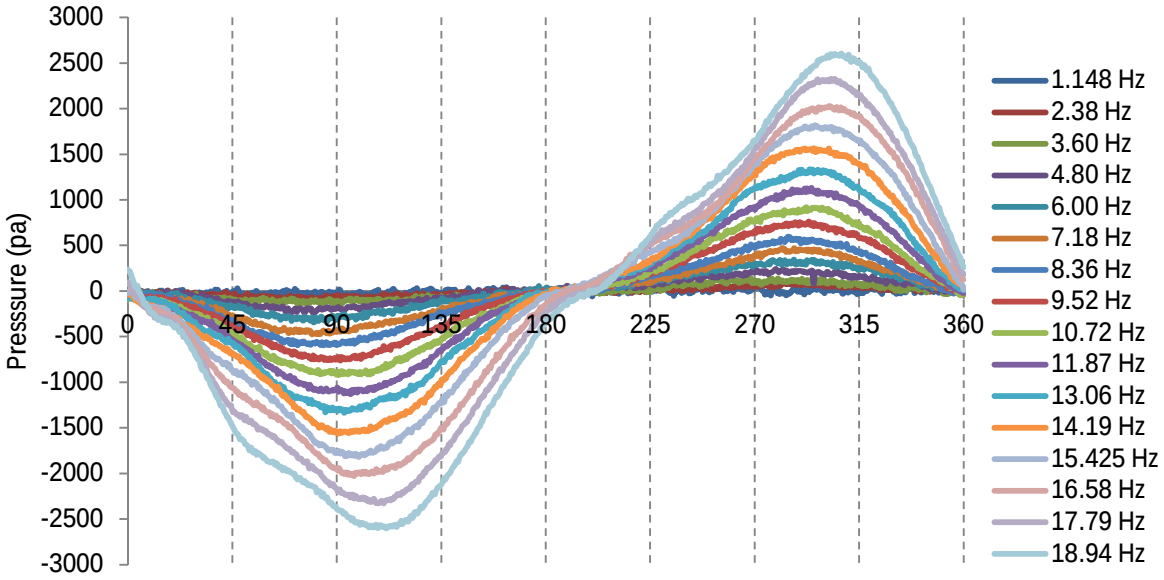

Fig. 5.2, Pressure drop vs. crank angle for a sample Mid3 (zero degree is the top-dead centre)

From simple harmonic motion the maximum velocity should occur at 90^o and 270^o which is where the maximum pressure drop should also be. However, Fig. 5-2 shows that as the frequency increased the maximum pressure drop was shifted by a few degrees. Data from other samples showed similar phase shifts which also increased by increasing the pressure drop. For instance sample Large 1 had 2^o, Mid 3 had 18^o and Small 3 had 20^o phase shift. Despite the best effort of the author, the position of the top-dead-centre did not set precisely and was slightly out of phase due to belt tension.

Figure 5.3 shows the pressure drop of the samples against frequency. Samples with small pore size had larger pressure drop compared to the samples with medium and large pore size.

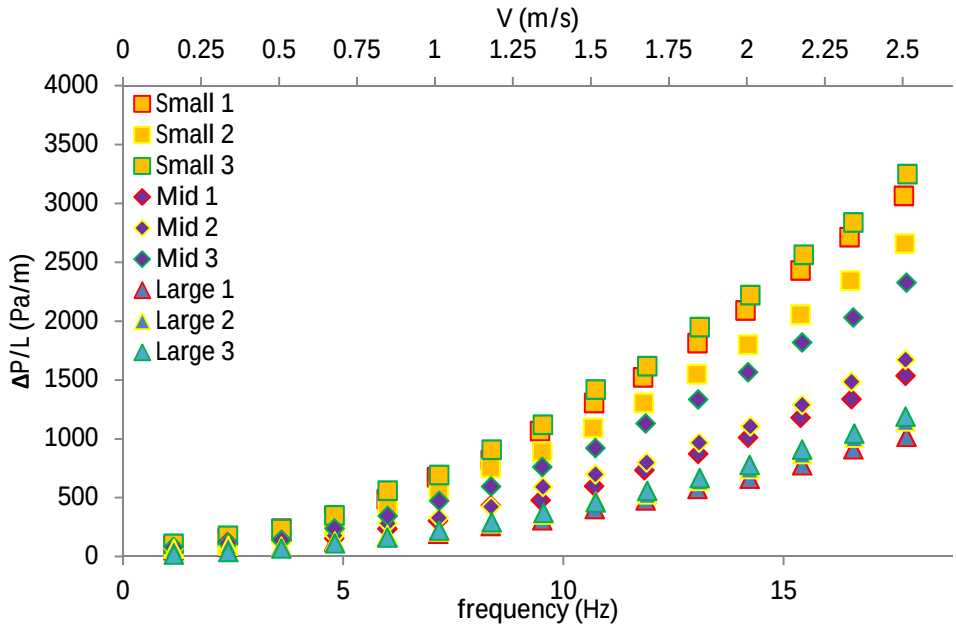

Fig. 5.3, Pressure drop of the metal foams against frequency and flow velocity

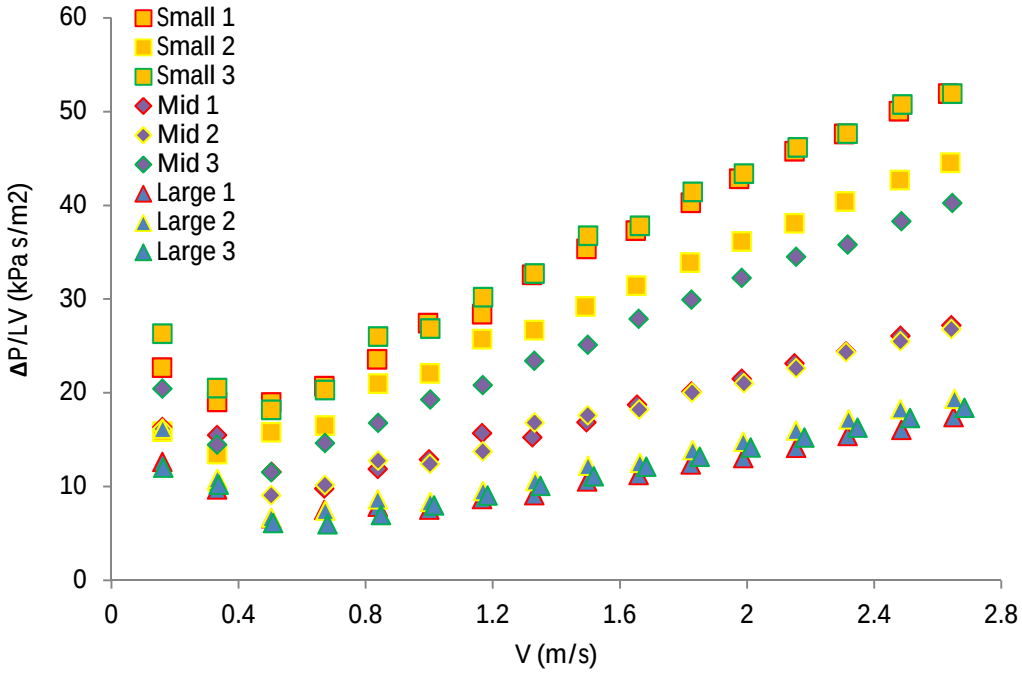

Fig. 5.4, Reduced pressure maximum pressure drop against Darcian velocity

Due to the variation in velocity profile through a cycle, an oscillatory flow is not strictly the same as used modelled by the Darcy-Forchheimer equation. However, applying the Darcy-Forchheimer equation to the oscillatory pressure data shows that pressure under oscillatory flow follows this model. Shown in Figure 5.4 is reduced pressure drop (based on Eq. 3.7)

plotted against velocity. From 0.5 m/s the reduced pressure increases linearly with velocity. In Chapter 3 it was shown that the Darcy-Forchheimer model is only valid for velocities above a certain threshold velocity. In Fig. 5.4, flow regime change from Darcy to Darcy-Forchheimer can be seen to occur around 0.5 m/s and the form drag term becomes important. A similar trend also was reported for metal foams by Dukhan and Minjeur for steady flow [69]. Due to the orifice plate limitation, samples pressure drop did not measured for flow velocity lower than one m/s velocity. Therefore, oscillatory results showed the regime change from Darcy to Darcy-Forchheimer.

The pressure data was linearized by dividing the normalised pressure data by velocity and a least-square line was fitted to each data set. The permeability and the form drag were calculated by applying a linear-regression to the data (method was described in Chapter 3). The calculated values are tabulated in Table 5.1 and compared to the steady pressure drop data. The results show that for the medium and large pore size both *K* and *C* were higher for oscillatory pressure drop. However, for the samples with small pore size both *K* and *C* were higher for steady flow than the oscillatory data.

Table 5.1 – Permeability and form drag coefficient for steady and oscillatory flow.

Name	Oscillatory flow				Steady flow			
	a	*b*	$K\times10^{8}(m^{2})$	$C\times10^{-3}(m^{-2})$	*a*	*b*	$K\times10^{8}(m^{2})$	$C\times10^{-3}(m^{-2})$
Small 1	11.38	15.69	1.57	13.31	2.78	18.29	1.11	12.59
Small 2	9.06	13.58	1.97	11.52	3.68	22.04	1.60	11.28
Small 3	12.56	15.28	1.42	12.96	2.82	23.66	1.19	13.11
Mid 1	4.46	8.62	3.99	7.31	2.76	9.25	4.16	7.07
Mid 2	4.31	8.54	4.13	7.24	2.76	9.30	3.97	6.95
Mid 3	6.05	12.99	2.94	11.02	3.31	15.21	0.91	1.04
Large 1	1.55	5.88	11.49	4.99	1.50	5.66	7.84	4.43
Large 2	1.80	6.59	9.90	5.59	1.76	6.35	6.86	4.98
Large 3	1.63	6.23	10.93	5.28	1.49	6.45	6.67	4.92

The difference between pressure drop under oscillatory flow and steady flow were tabulated against velocity in Table 5.2. It can be seen from the table that the difference between the steady and oscillatory result was lower for samples with larger pressure drop (sample Small 1, S and 3). In addition, for these samples (Small 1, 2 and 3) the pressure drop for steady flow was higher than the oscillatory flow after 2.15 m/s. The reasons for these

differences were not clear but it could be down to internal structure of the foams. A further study is needed to study the internal structure of the samples with non-destructive test such as 3D X-ray tomography.

Table 5.2- Difference between the oscillatory and steady flow pressure drop (percentage).

V (m/s)	Small 1	Small2	Small3	Mid 1	Mid 2	Mid 3	Large1	Large2	Large3
1.00	9.50	6.34	14.46	17.44	11.88	11.36	14.21	13.88	9.42
1.17	1.33	10.79	13.27	27.74	10.93	7.60	17.14	15.49	9.70
1.32	6.02	3.86	9.80	12.71	23.16	9.49	11.04	15.71	9.96
1.50	4.73	3.83	11.27	13.33	17.74	6.76	17.21	21.67	10.20
1.65	2.29	2.87	4.48	16.14	12.12	9.12	14.98	14.39	10.41
1.82	1.86	2.33	5.15	15.24	14.12	8.16	17.03	17.19	10.60
1.98	1.40	1.51	1.99	14.85	11.64	8.74	15.02	16.29	10.77
2.15	0.96	-0.13	0.80	15.48	12.37	8.33	16.25	17.18	10.92
2.31	-0.99	-0.38	-2.47	14.46	13.74	5.53	19.22	18.32	11.06
2.48	-2.18	-1.15	-2.70	14.98	12.13	6.05	16.76	18.55	11.19
2.63	-3.70	-2.36	-6.02	13.56	11.53	5.48	19.86	18.47	11.30

5.2. Velocity data

As it was discussed in chapter four, section 4.4.4, air velocity was measured with hot-wire anemometer to investigate the fluid behaviour under oscillatory motion. To do this, air velocity was measured inside the pipe connecting the test section to the compressor. Since the hot-wire probe was placed at the centre of the pipe it measured the actual air velocity at that particular point. Therefore, the results were different from the average velocity which was estimated by knowing the frequency. However, the results were used to cross check the velocity measured by the other method.

Show in Fig. 5.5 is the air velocity measured at the centre of the pipe at 18.84 Hz. Air velocity values was presented as absolute value since the hot-wire anemometer cannot detect the flow direction. The graph shows that the air velocity starts to fluctuate before and after it reaches the maximum value. Zhao and Cheng [56] investigated this fluctuation in air velocity under oscillatory flow condition. They explained that at high kinetic Reynolds number (high frequency) the annular effect became pronounced and this makes the fluid flow near the wall become unstable and eddies occur near the wall. These eddies then transferred to the centre of the flow which causes small fluctuations. During the

acceleration period (the first quarter and third quarter par of each cycle) the turbulence dissipates and the flow recovers to a laminar-like flow. The annular effect and the turbulence that generated during the deceleration period are key factors of increasing the pressure drop comparing to the steady flow pressure drop[56].

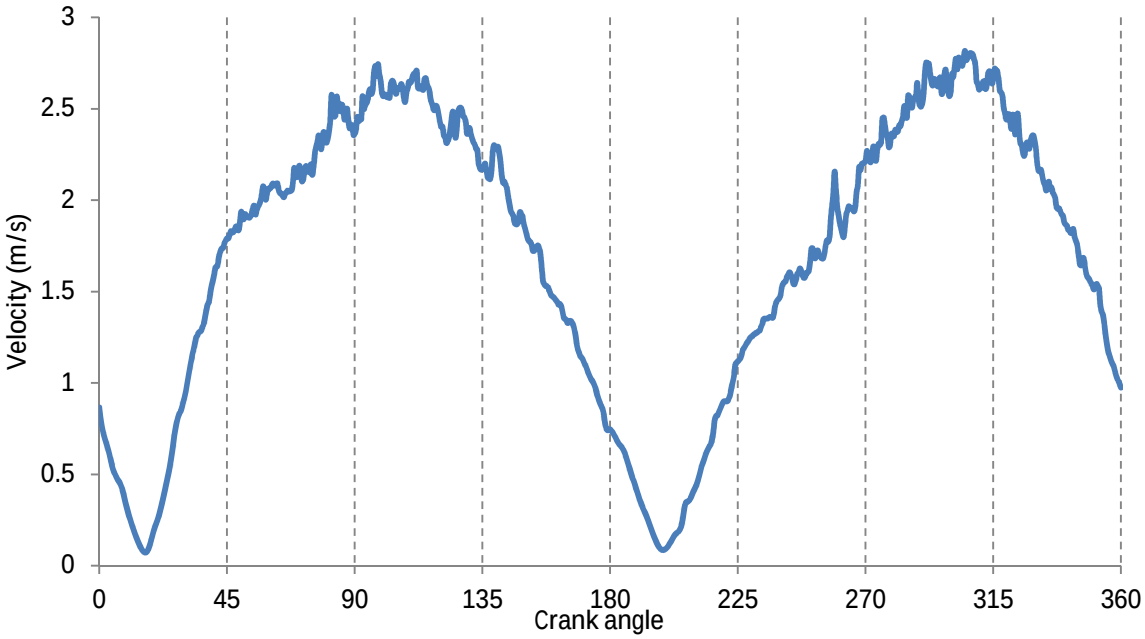

Fig. 5.5, Air velocity measured at the centre of the pipe at 18.84 Hz.

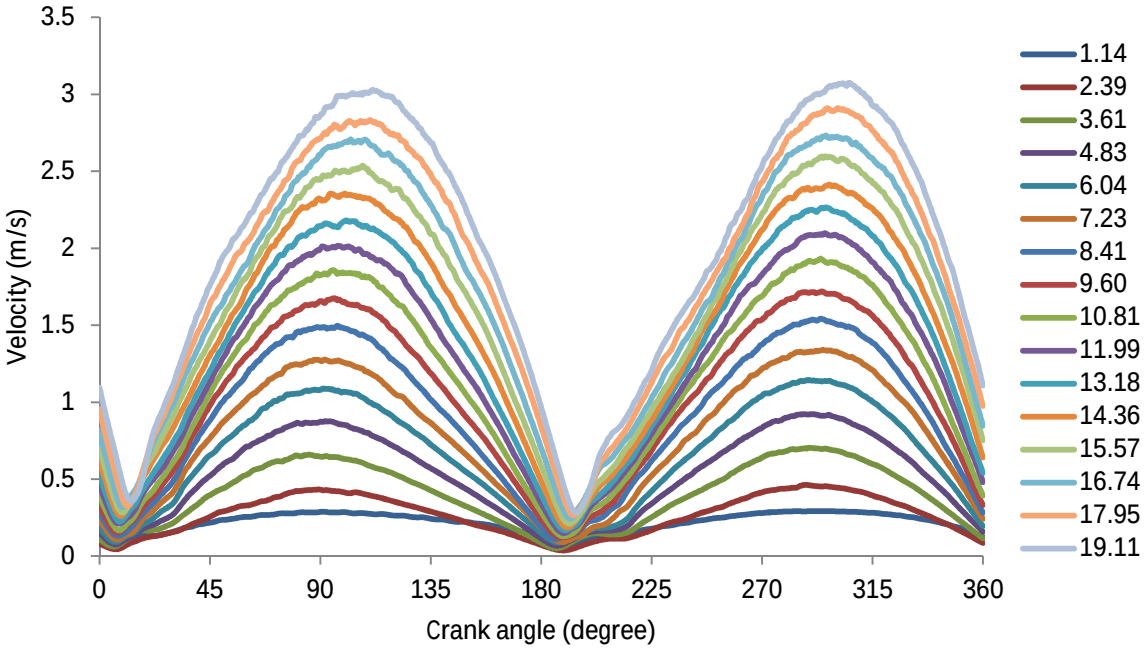

Fig.5.6, Temporal variation of air velocity at different frequency.

Air velocity was measured for 20 cycles for each frequency and the data were averaged and plotted at Fig. 5.6. It can be seen from the graph that even after averaging the results of 20 measurements the air velocity fluctuated during acceleration and deceleration period. The graph also shows that the maximum air velocity was shifted at high frequencies and this phase shifting increased by increasing the oscillation frequency. For instance the phase shift at 19.11 Hz was 16^{o} and at 3.61 Hz no phase shift was detected.

Since the air velocity was measured in the connecting pipe with inner diameter of 20 mm, it was converted into the velocity at the test section with inner diameter of 51.9 mm. The maximum air velocity at each cycle was slightly higher than the value calculated by the crank angle velocity. The reason for this could be the shape of the velocity profile inside the pipe. Since the air velocity was measured at the centre of the pipe, it only represented one single point of the velocity profile. Therefore the results could be higher than the average air velocity which was calculated by the other method.

5.3. Comparing results with other researchers

To the best knowledge of the author this type of metal foam has not been tested under oscillatory condition before. As a result, there is no available data to compare the experimental results of this study. In contrast, there have been many studies on wire mesh screens. In order to check the results produced by the rig were similar to other workers the wire mesh sample was tested under oscillatory flow. The results were compared with Tanaka et al [20] and Choi et al [70].

To generate the pressure drop data based on the Tanaka empirical correlation, Eq. 5.1 was used to calculate the pressure drop for the wire mesh sample. In order to present Tanaka's result based on pressure drop and air velocity, Reynolds number converted to velocity by Eq. 5.3 and 5.4; and friction factor converted to pressure drop by Eq. 5.2.

$$f = \frac{198}{Re} + 1.737 \qquad \text{Eq. 5.1}$$

$$f = \frac{\Delta P D_h}{\rho u_{max}^2 L/2} \qquad \text{Eq. 5.2}$$

$$Re = \frac{\rho u_{max} D_h}{\mu} \quad \text{Eq. 5.3}$$

$$D_h = \frac{4\varepsilon d_{wire}}{4(1-\varepsilon)} \quad \text{Eq. 5.4}$$

Similar steps were taken to calculate the pressure data from Choi et al friction factor correlation. Reynolds number and hydraulic diameter were calculated with Eq. 5.3 and 5.4 and friction factor and pressure data from Eq. 5.5 and 5.6.

$$f = \frac{39.52}{Re} + 0.01 \quad \text{Eq. 5.5}$$

$$f = \frac{\Delta P D_h}{2\rho u_{max}^2 L} \quad \text{Eq. 5.6}$$

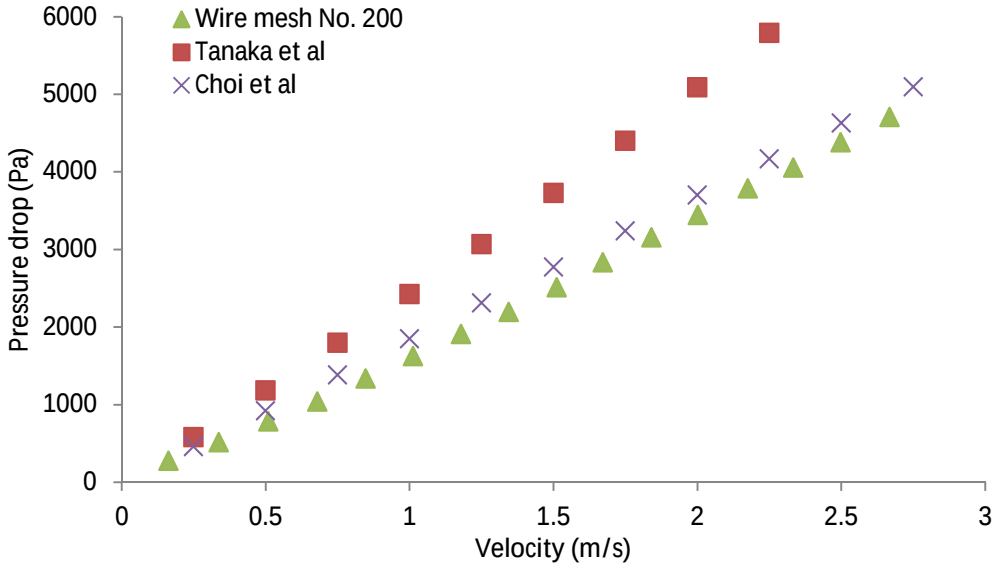

Fig. 5.7, The maximum pressure drop of 100 layers of wire mesh (No.200) under oscillatory flow

The result of the maximum pressure drop of the wire mesh sample under oscillatory flow against the maximum air velocity is depicted in Fig. 5.7. The pressure drops measured in this study were similar but slightly lower than those measured by Choi et al correlation results, both were lower than Tanaka's results. Ju and Shen [71] compared four friction factor correlations [20,49,70,72]and showed even greater variation in the pressure drop data. They argued that the reason for this discrepancy came from the differences in the geometric properties of the packed wire mesh, the operating frequencies and pressures, the different

definition of friction factor and dimensionless numbers; and uncertainty dealing with experimental data [73].

Chapter 6 - Single-blow method

6.1. Introduction

Measuring the local heat transfer in a regenerator is difficult due to its small pore size and complex geometry. To measure the temperature and velocity at pore level, would require inserting many probes inside pores and simultaneously measuring them across the regenerator. Currently this type of probe is not readily available. Therefore, the average heat transfer coefficient between the regenerator and flow is usually measured [74]. Two methods, the single-blow and oscillating flow techniques are commonly used to evaluate thermal performance of heat exchangers and regenerators. Although the oscillating flow method is closer to the actual operating conditions in Stirling engines, the difference in heat transfer coefficient is not significant. As a number of workers have shown that for Reynolds number (within the pore) higher than 60, the difference in heat transfer coefficient is less than 15% [2,20]. Moreover, the oscillating testing facility is more complicated and temperature measurement at high frequency is more challenging than the single-blow method.

The single-blow method is composed of three elements [75], an experiment, a heat transfer model and an evaluation scheme (matching technique). The experiment is relatively simple; a fluid flows steadily through the sample which is allowed to equilibrate with the passing fluid. A step change in temperature is applied to the inlet flow and heat transfer takes place between the fluid and the regenerator. The outlet temperature history (the breakthrough curve) is measured until the new equilibrated temperature is achieved. The heat transfer coefficient is estimated by matching the breakthrough curve with the curve predicted by the model.

Depending on the working fluid and regenerator type, a mathematical model can be developed to predict the outlet temperature. Schmidt and Willmott [76] presented and analysed several types of the single-blow model which will be discussed in the following section. The single-blow models of other researchers will be presented here. The consequences of using different assumptions will be presented and the numerical solution of the model used for this study will be discussed.

6.2. Mathematical model for the single-blow method

In the single-blow method the sample experiences a step change in temperature. Depending on fluid properties, thermal storage material and experimental setup, different mathematical model can be developed to predict the outlet temperature history.

Shown in Fig. 6.1 are the range of single-blow models possible depending on the initial assumptions. The single-blow model can be divided into two main models, finite and infinite fluid heat capacity dependent on the working fluid. Infinite fluid heat capacity models have two sub models based on the thermal conductivity of the thermal storage material. Finite fluid heat capacity models can be divided into two sub models dependent on the thermal resistance between the fluid and the thermal storage material. The Schumann-Hausen model can be divided into five sub models depending on the properties of experimental setup and regenerator's properties.

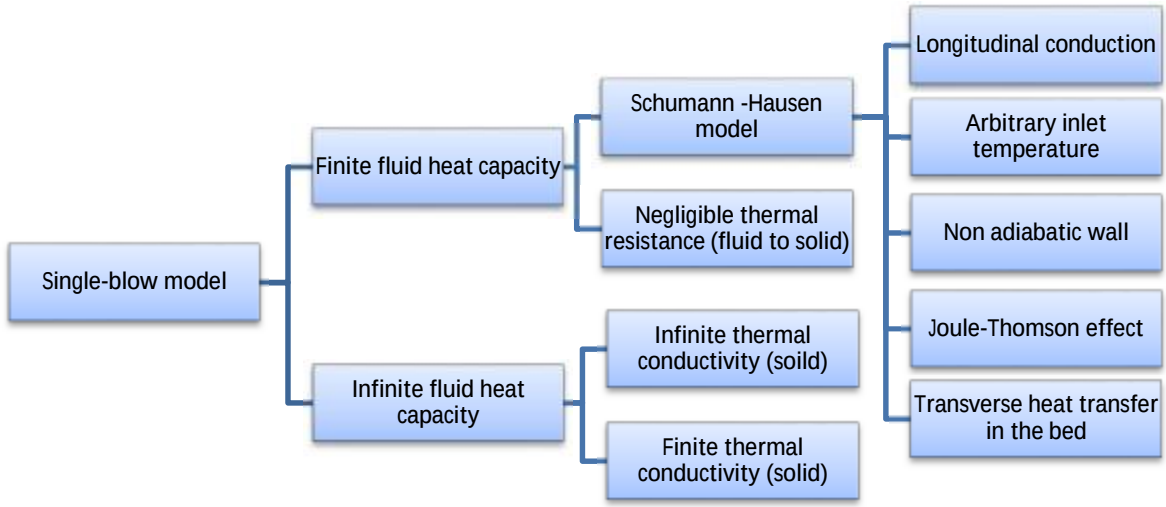

Fig. 6.1, Single-blow models based on different assumptions.

6.2.1. Infinite fluid heat capacity

Here it is assumed that the fluid temperature remains constant as it passes through the regenerator. This assumption is only valid if the fluid changes its phase as it passes through the regenerator or for fluids with high thermal capacity[76]. Heat transfer to the storage material can be modelled by the following two assumptions:

6.2.1.1. Negligible temperature gradients in the storage material (infinite thermal conductivity)

The temperature gradient within the sample is assumed negligible, when the following statements are valid:

I. The major heat transfer resistance is offered by the convection film between fluid and solid interface and negligible thermal conductivity of the storage material
II. Infinite fluid heat capacity.

Under these conditions the mathematical model for a storage unit can be obtained by

$$\left\{\begin{matrix}\text{Net rate of accumulation of} \\ \text{energy by the matrix}\end{matrix}\right\} = \left\{\begin{matrix}\text{Net rate of heat removed} \\ \text{from the fluid}\end{matrix}\right\} \qquad \text{Eq. 6.1}$$

$$A_{cs} L \rho_s C_s \frac{dt_s}{d\tau} = hA(t_{fi} - t_s)$$

performing an energy balance:

By introducing the following dimensionless quantities:

$$\acute{T}_s = \frac{t_s - t_0}{t_{fi} - t_0} \qquad \text{Eq. 6.2}$$

$$\eta = \frac{hA_{hs}\tau}{A_{cs} L \rho_s C_m}$$

Equation 6.1 becomes:

$$\frac{d\acute{T}_s}{d\eta} = 1 - \acute{T}_s \qquad \text{Eq. 6.3}$$

Thus the model is independent of the geometric configuration of the matrix.

6.2.1.2. Internal temperature gradients in storage material (finite thermal conductivity)

Large temperature gradient exist in the storage material if the heat transfer resistance offered by the convective film is of the same order of magnitude as that offered by the storage material[76]. In other words, thermal resistance of the material is much higher than the film heat transfer coefficient between fluid and the solid. The mathematical model of this type of application is depends on the geometry of the unit and the initial temperature distribution within the storage material. Figure 6.2 shows the case if the matrix is a rectangular flat slab.

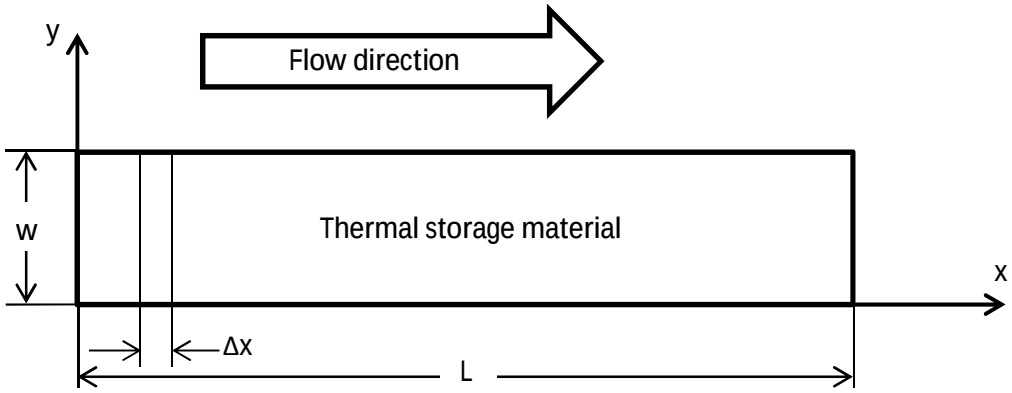

Fig. 6.2, Cross section of the storage unit

Since there are no temperature changes in the fluid (fluid phase change), the differential equation for the storage material is

$$\rho_s C_s \frac{\partial t_s}{\partial \tau} = k_s \frac{\partial^2 t_s}{\partial y^2} \qquad \text{Eq. 6.4}$$

By applying a dimensionless length *Y=y/w* (*w* is the slab thickness) and the Biot number ($Bi = \frac{hw}{k_s}$) the dimensionless energy equation becomes as:

$$\frac{\partial \acute{T}_s}{\partial \eta} = \frac{1}{Bi}\frac{\partial^2 \acute{T}_s}{\partial Y^2} \qquad \text{Eq. 6.5}$$

with the initial and boundary conditions of:

$$\text{for } \eta = 0 \qquad \acute{T}_s = 0 \qquad \text{Eq. 6.6}$$

$$\text{for } Y = 0 \qquad \frac{\partial \acute{T}_s}{\partial Y} = 0$$

$$\text{for } Y = 1 \qquad \frac{\partial \acute{T}_s}{\partial Y} = Bi(1 - \acute{T}_s)$$

Since the heat capacity of the fluid is infinite (fluid temperature is constant in *x* direction) and the thermal conductivity of the material is low, the temperature of the thermal storage material is the same in *x* direction at the same distance from the fluid-solid surface. As a result, the temperature gradient only exists in *y* direction. This also can be seen in Eq. 6.5.

6.2.2. Finite fluid heat capacity

In applications in which the working fluid is gas and has low heat capacity it is more appropriate to assume that the thermal energy storage unit operates with a finite fluid heat capacity. In this model the fluid and the thermal storage material have temperature gradient in *x* direction.

6.2.2.1. Negligible thermal resistance

This is the simplest model of finite fluid heat capacity model. If the thermal conductivity of the thermal storage unit and the convection heat transfer coefficient are very large, negligible heat resistance occurs between the fluid and the unit. Therefore, the temperature

of the fluid and the unit will be the same. As a result, one energy equation can be written for both the fluid and the storage material:

$$\dot{m}_f C_f \frac{\partial t}{\partial x} + A_{cs} L \rho_s C_s \frac{\partial t}{\partial \tau} = k_s \frac{\partial^2 t_s}{\partial x^2} \qquad \text{Eq. 6.7}$$

The following dimensionless variables are introduced:

$$X = \frac{x}{k_s}(\dot{m} C_f) \qquad \text{Eq. 6.8}$$

$$T = \frac{t - t_0}{t_{fi} - t_0}$$

$$\Theta = \frac{\tau(\dot{m} C_f)^2}{k_s A_{cs} L \rho_s C_s}$$

Substituting the above variables in Eq. 6.7 yields:

$$\frac{\partial T}{\partial X} + \frac{\partial T}{\partial \Theta} = \frac{\partial^2 T}{\partial X^2} \qquad \text{Eq. 6.9}$$

6.2.2.2. Schumann-Hausen model

This model was developed and analytically solved separately by Schumann [10] and Hausen in 1929. The theory was applied to a practical scenario the following year when Furnas [12] used the solutions in a study on heat transfer from a gas stream to a bed of iron balls. Furnas compared the experimental output curve from the single-blow rig to the theoretical curve generated from Schumann's work to determine the practical heat transfer coefficients and derive empirical solutions. Tong and London [16] used Schumann's model to experimentally evaluate the thermal performance of six types of wire-screen matrixes and a packed bed of steel balls with different porosity for a range of Reynolds number. They obtained correlation equations of heat transfer and pressure drop for the samples.

In this model the thermal conductivity of the thermal storage material is infinite in the *y* direction (high thermal conductivity) and zero in the *x* direction. Therefore, the temperature gradient of the fluid and the heat storage material will be only in *x* direction.

The following assumptions were made [76]:

1- Adiabatic walls
2- Step change in inlet fluid temperature
3- Sample has infinite traverse thermal conductivity and zero longitudinal thermal conductivity
4- Fluid and sample material have constant properties
5- The gas flows at a constant speed along the sample
6- Uniform heat transfer coefficient

Mathematical expressions for the temperature distribution in the cross-section of a regenerator will be presented in the following section.

6.2.2.2.1. Deriving the equations

By writing the energy balance for an incremental volume of length Δx the one-dimensional energy equation can be derived. The heat entering the incremental volume is equal to the heat leaving plus the heat accumulated within the sample.

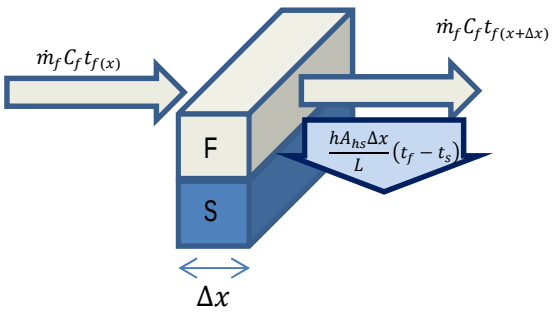

Fig. 6.3, The incremental volume of solid and fluid

Fig. 6.3 shows the energy content entering and leaving the section and the portion of heat transferred from the fluid to the solid and accumulated in the section. Since the fluid has

low thermal capacity, the rate of accumulation of heat by the fluid is negligible (finite heat capacity of the fluid).

The energy balance for the fluid is [76]:

$$\dot{m}_f C_f t_{f(x)} = \frac{hA_{hs}\Delta x}{L}\left(t_f - t_s\right) + \dot{m}_f C_f t_{f(x+\Delta x)} \quad \text{Eq. 6.10}$$

The fluid temperature leaving the section is equal to:

$$t_{f(x+\Delta x)} = t_{f(x)} + \frac{\partial t_f}{\partial x}\Delta x \quad \text{Eq. 6.11}$$

The Eq. 6.10 can be simplified to:

$$\frac{\dot{m}_f C_f L}{hA_{hs}}\frac{\partial t_f}{\partial x} = \left(t_s - t_f\right) \quad \text{Eq. 6.12}$$

A similar method can be applied to the solid within the incremental volume. The left side of the Eq. 6.13 is the rate of accumulation of heat by the solid which is equal to the heat transferred from the fluid to the solid. The energy balance for the solid is:

$$A_{cs}\Delta x \rho_s C_s \frac{\partial t_s}{\partial \tau} = \frac{hA_{hs}\Delta x}{L}\left(t_f - t_s\right) \quad \text{Eq. 6.13}$$

which can be simplified to:

$$\frac{LA_{cs}\rho_s C_s}{hA_{hs}}\frac{\partial t_s}{\partial \tau} = \left(t_f - t_s\right) \quad \text{Eq. 6.14}$$

The following dimensionless variables are introduced [76]:

Dimensionless distance:

$$\xi = \frac{hA_{hs}x}{\dot{m}_f C_f L} \quad \text{Eq. 6.15}$$

Dimensionless length (*NTU*): $$NTU = \frac{hA_{hs}}{\dot{m}_f C_f}$$

Dimensionless time: $$\eta = \frac{hA_{hs}\tau}{A_{cs}L\rho_s C_s}$$

Dimensionless fluid temperature: $$T_f = \frac{t_f - t_0}{t_{fi} - t_0}$$

Dimensionless solid temperature: $$T_s = \frac{t_s - t_0}{t_{si} - t_0}$$

The dimensionless form of the Eq. 6.12 and 6.14 become:

For the fluid: $$\frac{\partial T_f}{\partial \xi} = T_s - T_f \qquad \text{Eq. 6.16}$$

For the solid: $$\frac{\partial T_s}{\partial \eta} = T_f - T_s \qquad \text{Eq. 6.17}$$

Initial and boundary conditions are:

$$\xi = 0 \qquad T_f = 1 \quad T_s = 1.0 - e^{-\eta} \qquad \text{Eq. 6.18}$$
$$\eta = 0 \qquad T_s = 0$$

6.2.2.2.2. Analytical solution

Shown in Eq. 6.19 is analytical solution for Eq. 6.16 and 6.17 which was offered by Kohlmayer [77]. It was used to generate the predicated break out temperature history.

$$T_f = e^{-NTU}\left[1 + NTU\eta \sum_{i=0}^{\infty} \frac{\eta^l}{l+1} \times \left(\sum_{i=k}^{\infty} \frac{(-1)^{l-k} NTU^k}{k!\,(k-1)!\,(l-k)!}\right)\right] \qquad \text{Eq. 6.19}$$

A Matlab code was written to generate the outlet flow temperature for different *NTU* value based on E. 6.19 and plotted against the dimensionless time (η), show in Fig. 6.4. The power series in Eq. 6.19 is valid for i and k larger than 60.

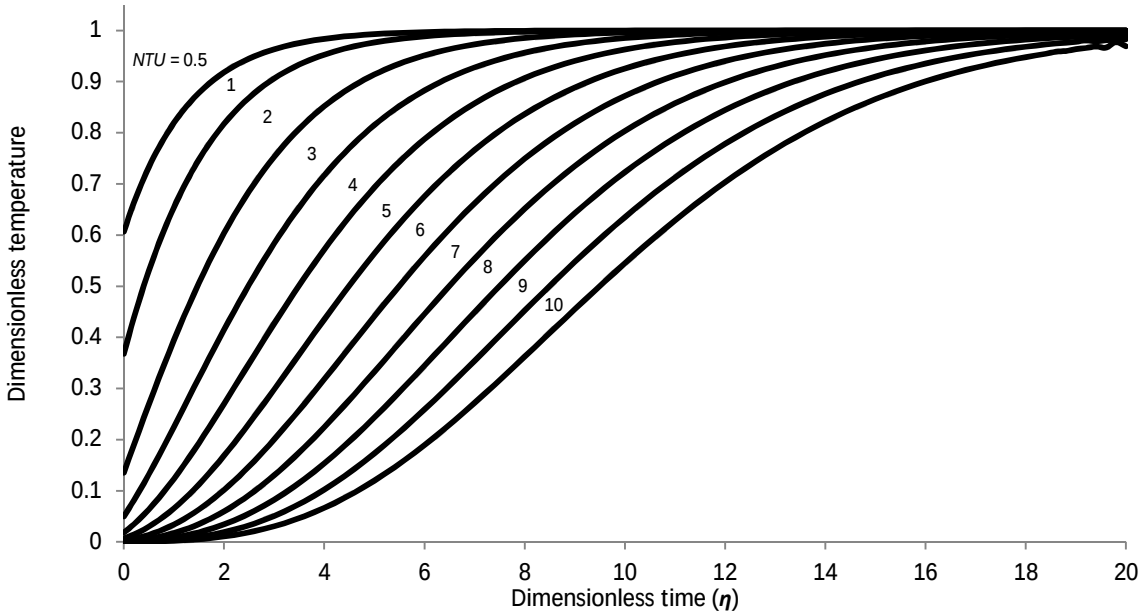

Fig. 6.4, Outlet fluid temperature against dimensionless time with different NTU values.

6.2.2.3. Extended Schumann-Hausen:

A number of the assumptions in the Schumann-Hausen model are unrealistic. For instance, it is near physically impossible to execute an experiment that achieves an ideal temperature step change [75]. Moreover, in the actual experiment there is always heat loss from the test section which influences the outlet fluid temperature. That the wall is adiabatic is a poor assumption for many applications. In addition, if a large pressure drop exists across the regenerator the Joule-Thomson effect influences the outlet temperature. This effect is more common in cryogenics application. Some regenerators have large longitudinal conduction and neglecting this effect in the simplified model may introduce an error in the estimation of heat transfer coefficient. Sample holders and wind tunnel walls may also participate in increasing the sample core mass and may introduce an error to measuring the heat capacity of the regenerator. Since the development of the Schumann-Hausen model researchers have improved this model to more correctly represent the single-blow experiment. In the next section five improved models will be discussed.

- Inter-particle conduction model (longitudinal conduction model)

Neglecting the longitudinal thermal conductivity could introduce large error in predicting the *NTU* value. For instance, Loehrke showed that ignoring this effect could introduce nearly a factor of 2 error in the *NTU* estimation [75]. Pucci et al. [78] added this effect in their model and showed that it was dominant for *NTU*>2. In another study Cai et al. [79] showed that this effect must be included for *NTU* $\geq$3.

- Arbitrary inlet temperature

  Since experimentally achieving a step change temperature is not physically possible; Liang and Yang [80], Cai et al. [79] and Mullisen and Loehrke [81] used an exponential variation to define the inlet fluid temperature. By knowing the mathematical expression of the inlet fluid temperature curve it became possible to have an arbitrary inlet fluid temperature instead of a step function in the previous model.

- Non adiabatic wall

  Depending on the test rig design and fabrication, heat from the sample could dissipate through the wall and neglecting this heat loss could introduce error to the result. Chen and Chang [74] added the effect of axial conduction and heat flux into the wall in their single-blow model by introducing the thermal conductivity of the wall (λ_w), NTU_w and *Rtc* (capacitance ratio of matrix to the tube wall). They showed that for their test rig *NTU* value was underestimated by 31% due to the adiabatic wall assumption.

- Joule-Thomson effect

  Depending on the Joule-Thomson coefficient (positive or negative), a fluid temperature could drop or rise when it encounters a restriction in the flow [82]. This effect was introduced in the single-blow model by Chen et al. [2] and they showed the effect of neglecting this effect on regenerator. However, they reported for a pack of 200 wire mesh (No. 200) which had a pressure drop around 0.2 MPa the air temperature drop was only 3%. Therefore, this effect is only applicable for samples with high pressure drop.

- Transverse heat transfer in the bed

  The radial conduction in the fluid flow and the regenerator was added in the single-blow model by Chang et al. [18]. They observed that the temperature distribution along the direction normal to the fluid flow was not uniform. The results from the new model were 8% lower than the results predicted when this effect omitted from the model. However, these results were for the regenerator with high *NTU* (*NTU*>150) and the effect would be negligible for lower *NTU*. In addition, tested samples were made of stainless steel which had nearly 4 times lower thermal conductivity compared to aluminum. As a result, this effect has negligible effect on predicted *NTU* result here.

6.3. Single-blow model used for this study

In this study the model which developed by Chang and Chen [18] was used to predict the outlet temperature history. However, as explained in the previous section the effect of radial conduction within the sample and the Joule-Thomson expansion effect were omitted because of their negligible effect for this type of regenerator. The samples used in this study were made from aluminium which had high thermal conductivity. Therefore the radial thermal conductivity effect would be negligible. In addition, Joule-Thomson expansion effect was insignificant because of relatively low pressure drop across the samples. The following PDEs are used to model the outlet temperature history:

For the fluid,

$$\frac{\partial T_f}{\partial x} + NTU\left(T_f - T_s\right) + NTU_w\left(T_f - T_w\right) = 0 \qquad \text{Eq. 6.20}$$

For the regenerator,

$$\frac{\partial T_s}{\partial \tau} + \lambda \frac{\partial^2 T_s}{\partial x^2} + NTU\left(T_s - T_f\right) = 0 \qquad \text{Eq. 6.21}$$

For the side wall,

$$\frac{\partial T_w}{\partial \tau} - R_{tc}\lambda_w \frac{\partial^2 T_w}{\partial x^2} + R_{tc} NTU_w \left(T_w - T_f\right) = 0 \qquad \text{Eq. 6.22}$$

Dimensionless variables:

$$R_{tc} = \frac{M_s C_s}{M_w C_w} \quad \lambda = \frac{k_e A_{cs}}{\dot{m}_f C_p L} \quad \lambda_w = \frac{k_w A_w}{\dot{m}_f C_p L} \quad \tau = \frac{\dot{m}_f C_p t}{M_s C_s}$$

Initial conditions:

$$t = 0, \; T_f(x) = T_s(x) = T_w(x) = 0$$

Boundary conditions (Neumann type):

For *t*>0

$$x = 0, \quad T_f = 1 - e^{(-\tau/\tau_i)}$$

$$x = 0, \quad \frac{\partial T_s}{\partial x} = 0, \quad \frac{\partial T_w}{\partial x} = 0$$

$$x = 1, \quad \frac{\partial T_s}{\partial x} = 0, \quad \frac{\partial T_w}{\partial x} = 0$$

This is a system of three partial differential equations (PDE) with two independent variables (*x* and *t*), there are three dependent variables, T_f *(x, t)*, T_w *(x,t)* and T_s*(x,t)* to be determined. Since the PDEs are parabolic the solution was marched forward in time from the initial condition and guided and modified by the boundary conditions [83] (Fig. 6.5b).

6.4. Numerical scheme

6.4.1. Discretization

Since Eq. 6.21, 6.22 and 6.23 are parabolic partial differential equations, first an explicit method was used to solve them for the solution domain. Then the results were recalculated by an implicit method (The Crank-Nicolson) to improve their accuracy. Finally, the results were evaluated by the Kohlmayer's [77](Eq. 6.19) analytical solution.

To numerically solve the Eq. 6.21, 6.22 and 6.23, first the physical domain was discretized into a difference grid. Since the samples of interest here have high thermal conductivity (so that there is no traverse temperature gradient), the solution domain was discretised only in the flow direction (*x*) (Fig. 6.5b). It was assumed that there is no heat transfer through the wall.

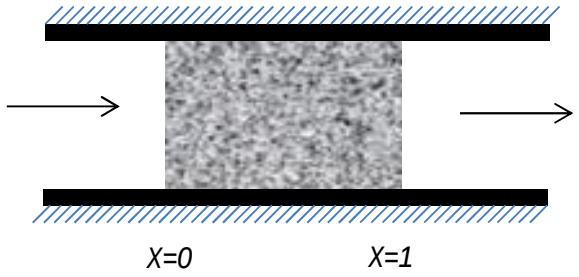

Fig. 6.5a, Position of the sample and holder

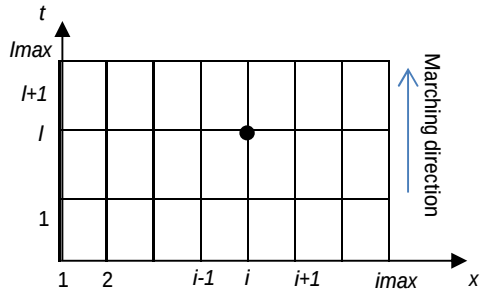

Fig. 6.5b, One-dimensional physical domain

Each part of the partial differential equations (PDE) was approximated by algebraic finite difference approximations (FDAs). The second-order centred-space approximation was used to determine $\frac{\partial^2 T_s}{\partial x^2}$ (Eq. 6.23) and the first-order forward-time approximation was used to give $\frac{\partial T_s}{\partial \tau}$ and $\frac{\partial T_w}{\partial \tau}$ (Eq. 6.23 and 6.24). The first-order forward-space approximation was used for $\frac{\partial T_f}{\partial x}$ (Eq. 6.25).

$$\frac{\partial^2 T}{\partial x^2} = \frac{T_{i+1}^l - 2T_i^l + T_{i-1}^l}{\Delta x^2} \qquad \text{Eq. 6.23}$$

$$\frac{\partial T}{\partial \tau} = \frac{T_i^{l+1} - T_i^l}{\Delta \tau} \qquad \text{Eq. 6.24}$$

$$\frac{\partial T}{\partial x} = \frac{T_{i+1}^{l} - T_{i}^{l}}{\Delta x} \qquad \text{Eq. 6.25}$$

The FDAs (Eq. 6.23, 6.24 and 6.25) were substituted into the PDEs (Eq. 6.20, 6.21 and 6.22) to obtain algebraic finite difference equations (FDE).

$$\frac{T_{f_{i+1}}^{l} - T_{f_i}^{l}}{\Delta x} + NTU\left(T_{f_i}^{l} - T_{s_i}^{l}\right) + NTU_w\left(T_{f_i}^{l} - T_{w_i}^{l}\right) = 0 \qquad \text{Eq. 6.26}$$

$$\frac{T_{s_i}^{l+1} - T_{s_i}^{l}}{\Delta\tau} - \lambda\left(\frac{T_{s_{i+1}}^{l} - 2T_{s_i}^{l} + T_{s_{i-1}}^{l}}{\Delta x^2}\right) + NTU\left(T_{s_i}^{l} - T_{f_i}^{l}\right) = 0 \qquad \text{Eq. 6.27}$$

$$\frac{T_{w_i}^{l+1} - T_{w_i}^{l}}{\Delta\tau} - R_{tc} \times \lambda_w\left(\frac{T_{w_{i+1}}^{l} - 2T_{w_i}^{l} + T_{w_{i-1}}^{l}}{\Delta x^2}\right) + R_{tc} \times NTU_w\left(T_{w_i}^{l} - T_{f_i}^{l}\right) = 0 \qquad \text{Eq. 6.28}$$

For the boundary conditions (by the first-order forward- space approximation) at $x = 0 \; and \; 1$:

$$\frac{T_{s_2}^{l} - T_{s_1}^{l}}{\Delta x} = \frac{T_{w_2}^{l} - T_{w_1}^{l}}{\Delta x} = 0 \xrightarrow{yields} \begin{cases} c = T_{s_1}^{l} \\ T_{w_2}^{l} = T_{w_1}^{l} \end{cases}$$

By knowing the initial temperature of the fluid at time step 1 ($T_{f_0}^{1}$), the sample and wall temperature at time 2 ($T_{s_1}^{2}$ and $T_{w_1}^{2}$) can be calculated by Eq. 6.27 and 6.28. Knowing the value of $T_{s_1}^{2}$ and $T_{w_1}^{2}$, $T_{f_1}^{1}$ can be calculated from Eq.18. These steps were depicted in Fig. 6-6. In this figure the stars show the solution at each point for the sample (blue), wall (green) and fluid (red); and the circles represent the required data for finding the solution of each stars.

As it can be seen from the Eq. 6.27 and 6.28 the solution at each point at time level *l+1* depends only on the solution at neighbouring points at time level *l*. This finite difference method is called an explicit method because the solution at each point is specified in terms of the known solution at neighbouring points at previous time step [83].

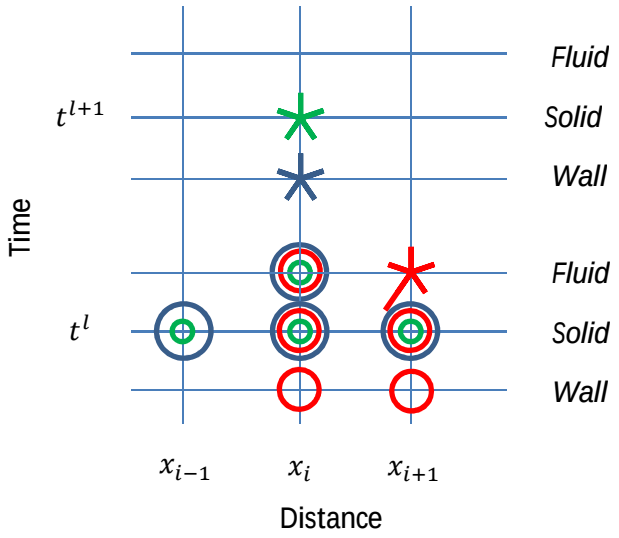

Fig. 6.6, Description of the explicit method used of the mode

6.4.2. Convergence and Stability

In explicit method if Δx and Δt approach zero, the results approach the true solution. However, this also increases the computation cost of the numerical solution. Setting Δx and Δt too large reduces the computation cost but the solution may not be stable or even converge. In order to have a stable and convergent numerical solution, $\lambda \frac{\Delta \tau}{\Delta x^2}$, which is in some text book called diffusion number [84], should be equal or smaller than 0.5. It is also reported that that setting the diffusion number, *di*, to 0.5 could stop growing the errors but the result may oscillate. To minimise the error oscillation *di* should be smaller or equal to 1/4. It is also suggested that setting *di* ≤1/6 minimised the truncation error [85]. Depending on the value of λ for each sample, Δx and Δt were calculated to ensure the convergence and stability of the solution. An example of this calculation presented in Appendix 2.

6.4.3. The Crank-Nicolson Method

For further correction, the Crank-Nicolson method was applied to Eq. 6.21 and 6.22 and iterated several times until T_s, T_w and T_f converged. The Crank-Nicolson is an implicit method which is consistent and unconditionally stable. However, in this method the special derivative is approximated at *l+1* time level and solving the equation would not be possible without knowing the values at *l+1* time level. Unlike the previous method, the Crank-Nicolson method needs eight unknowns (marked by doughnut shapes) at *l* and *l+1* level to

calculate T_s, T_w and T_f (marked by star shapes – green for solid, blue for wall and red for fluid temperature). Therefore, unlike the implicit method, the equations cannot be solved in this method without knowing the variable at level *l+1*. Consequently, this method was applied to the initial predicted value which was calculated by the first method to further improve the results. Similar procedure was also applied to this model by Chen and Chang [86] and Chen et al. [2].

$$T_{s_i}^{l+1} = T_{s_i}^{l} - \left(\frac{2\lambda\Delta\tau}{\Delta x^2} + NTU.\Delta\tau\right)\left(\frac{\overline{T_{s_i}^{l+1}} + T_{s_i}^{l}}{2}\right) + \frac{\lambda\Delta\tau}{\Delta x^2}\left(\frac{\overline{T_{s_{i+1}}^{l+1}} + \overline{T_{s_{i-1}}^{l+1}} + T_{s_{i+1}}^{l} + T_{s_{i-1}}^{l}}{2}\right) + NTU.\Delta\tau\left(\frac{T_{f_i}^{l+1} - T_{f_i}^{l}}{2}\right) = 0 \quad \text{Eq. 6.29}$$

$$T_{w_i}^{l+1} = T_{w_i}^{l} - R_{tc}\left\{\left(\frac{2\lambda_w\Delta\tau}{\Delta x^2}\right)\left(\frac{\overline{T_{w_i}^{l+1}} + T_{w_i}^{l}}{2}\right) + \frac{\lambda_w\Delta\tau}{\Delta x^2}\left(\frac{\overline{T_{w_{i+1}}^{l+1}} + \overline{T_{w_{i-1}}^{l+1}} + T_{w_{i+1}}^{l} + T_{w_{i-1}}^{l}}{2}\right)\right\} + NTU.\Delta\tau.R_{tc}\left(\frac{T_{f_i}^{l+1} - T_{f_i}^{l}}{2}\right) = 0 \quad \text{Eq. 6.30}$$

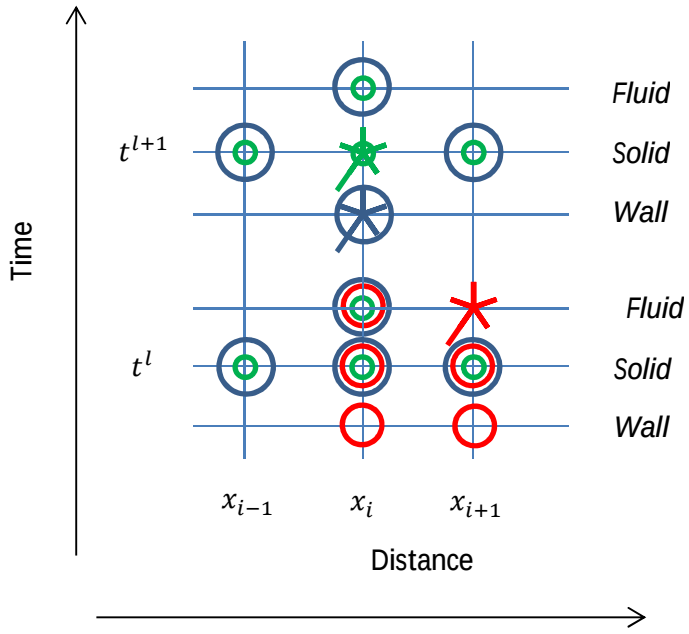

Fig. 6.7, Description of the Crank-Nicolson method used for correction

In this method the circle with the star represented the value of that point which was previously calculated by the explicit method. The equations 6.21 and 6.22 were iterated until the values were converged whilst for Eq. 6.20 the explicit method was used.

The numerical solution was tested against the analytical solution presented in section 6.2.2.2.2. For *NTU=10, Δτ=0.01* and *Δx=0.01* the outlet temperature was 0.6% lower than the analytical result and by setting *Δτ=0.001* the result was only improved 0.1%.

6.5. The effect of different variables on the outlet temperature

To understand the impact of the modelling assumptions and sample properties a parametric study was run using the final model described above. The temperature history curves were characterised by their maximum gradient (S_{max}) which has been shown to have a unique relationship with the *NTU* of the sample [77]. Better performing regenerators will have larger values of S_{max}.

6.5.1. Relationship between the maximum gradient (S_{max}) and *NTU*

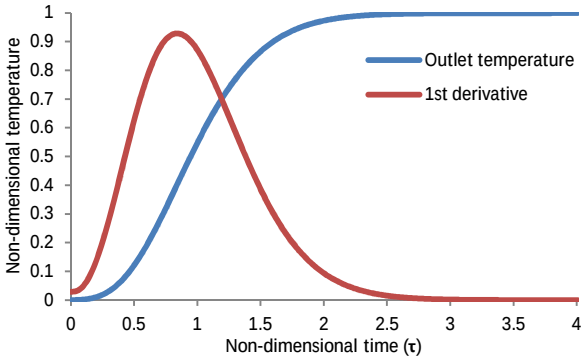

Fig. 6.8, The temperature response and 1st derivative of the curve.

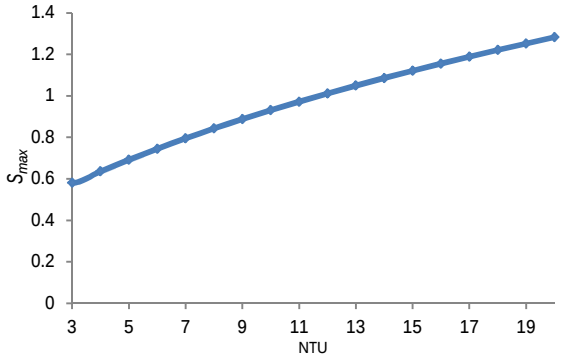

Fig. 6.9, S_{max} of the response curve for different *NTU*.

Fig. 6.8 demonstrates the outlet temperature curve for *NTU* = 10 (NTU_w=0.001, λ=0.001, λ_w=0.001, ψ =0.0001 and R_{tc}=0) with the first derivative from which the maximum gradient was obtained. As the *NTU* was increased (either by increasing the sample specific surface area or reducing the flow rate) the break out curve gradient becomes steeper resulting in an increase in S_{max}.

6.5.2. Heat loss from the walls

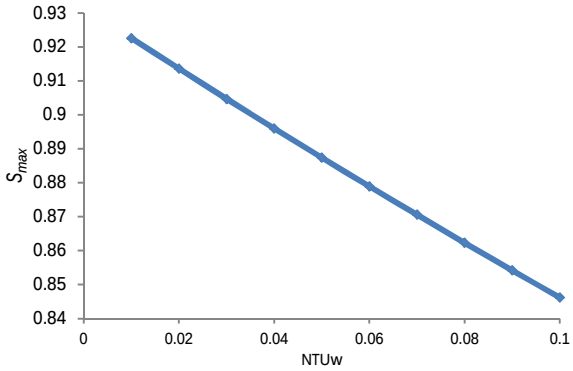

Fig. 6.10, The effect of wall *NTU* on S_{max} of the sample.

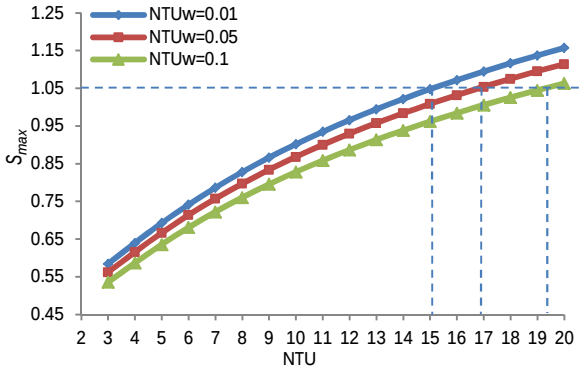

Fig. 6.11, The effect of *NTUw* on estimated *NTU*.

The heat flux into the tube wall can be modified by adjusting NTU_w, R_{tc} and k_w. Heat lost to the wall reduces the thermal performance of the sample. Shown in Fig. 6.10 is the impact of increasing NTU_w on S_{max}, all the other variables were kept constant (*NTU*=10, *Rtc*=1 , λ=0.001, λ_w=0.001 and ψ =0.0001). The maximum gradient decreases as NTU_w increased. Thus the heat loss from the wall will reduce the performance of regenerators. The maximum gradients for three different NTUw values are shown in Fig. 6.11. The selected values were a realistic value for heat lost through the wall based on the value achieved from the experimental results. Also shown in Fig. 6.11 is the impact of different NTU_w values on predicted *NTU*.

6.5.3. Longitudinal heat transfer effect

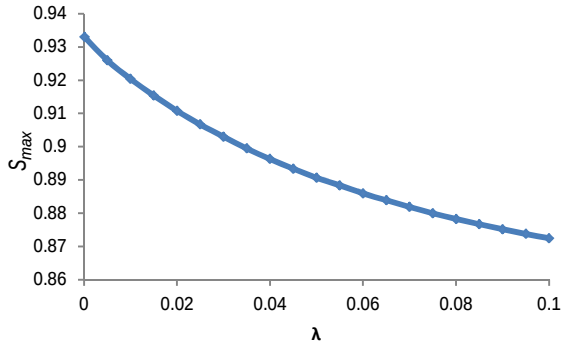

Fig. 6.12, The effect of sample's ND effective axial thermal conductivity on S_{max}.

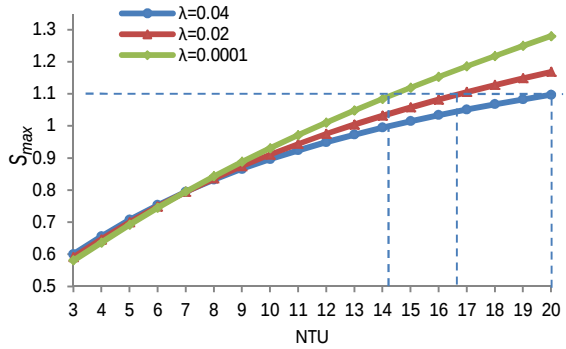

Fig. 6.13, The effect of sample's ND effective axial thermal conductivity on estimated *NTU*.

The longitudinal heat transfer depends on both the sample material and its method of manufacture. It can be modified in the model by changing the thermal conductivity; this is

shown in Fig. 6.12, where S_{max} decreases as the dimensionless effective thermal conductivity increases. Stainless steel which has a low thermal conductivity will perform better than samples manufactured from aluminium which was used here. Moreover, in Stirling engines the regenerator connects the high and low temperature parts of the engine and using regenerators with low axial conduction reduces the thermal bridging effect form the hot to cold part. Any heat leakage from one side to the other part reduces the overall efficiency of the engine. Fig. 6.13 shows that like NTU_w neglecting λ in the model will result in as underestimated of the sample *NTU.*

6.5.4. Sample heat capacity ratio effect

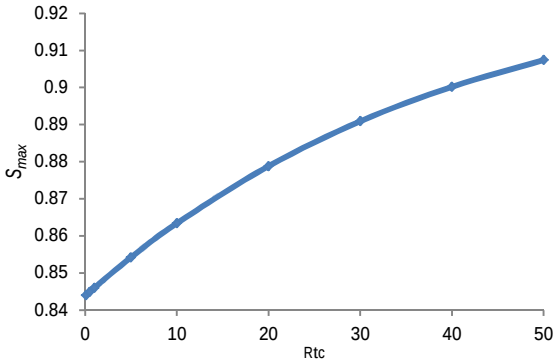

Fig. 6.14, The effect of capacity ratio of sample to the wall on S_{max}.

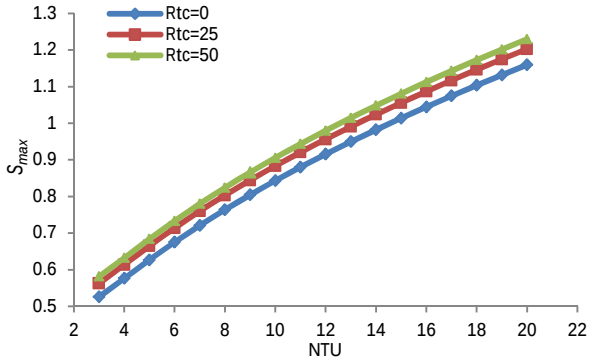

Fig. 6.15, The effect of capacity ratio of sample to the wall on S_{max}.

The effect of capacity ratio (R_{tc}) on the maximum gradient is depicted on Fig. 6.15. It shows by increasing the sample's heat capacity and reducing the wall heat capacity the maximum gradient increases. The negligence of this effect would yield an overestimation of the *NTU*.

6.5.5. Inlet temperature profile effect

Shown in Fig. 6.16 is the effect of inlet temperature profile on predicted maximum gradient, (S_{max}) results. The graph shows the impact of reducing the inlet temperature response time and keeping the other variable constant (*NTU*=10, NTW_w, *Rtc*=1.1, λ=0.001 and λ_w=0.001). Next graph, Fig. 6.17, shows the inlet temperature profiler at various response times. These data were calculated by $T_f = 1 - e^{(-\tau/\psi)}$ which was given earlier as the boundary condition for inlet air profile. This profile depends on the test rig performance and it means the time that takes the inlet temperature reaches the maximum temperature.

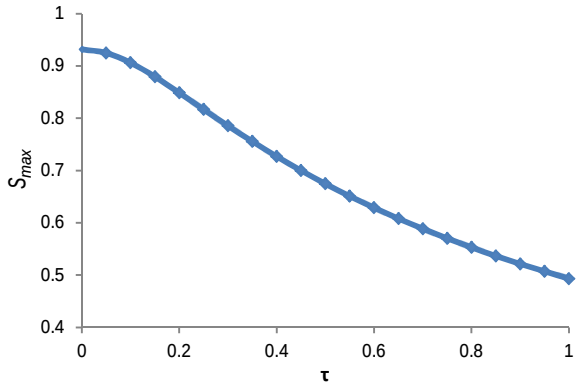

Fig. 6.16, The effect of inlet temperature profile on S_{max}.

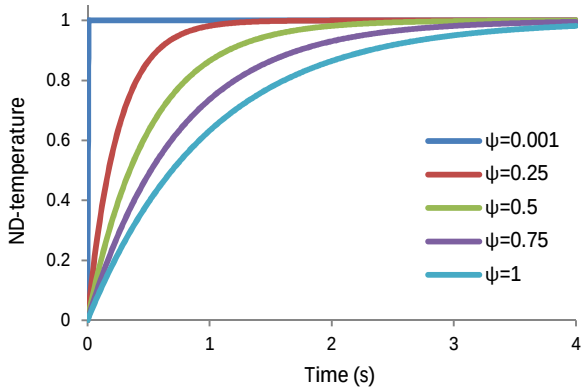

Fig. 6.17, The inlet temperature profile at various response times.

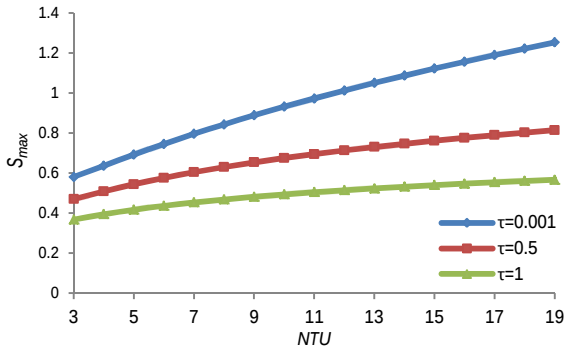

Fig. 6.18, The effect of inlet temperature profile on predicted *NTU*

Predicted *NTU* value can be underestimated by neglecting the inlet temperature profile in the single-blow. This can be seen in Fig. 6.18. For instance, if the response time of the rig is 0.5 and sample has maximum gradient of 0.8. The predicted *NTU* with a near step-change (ψ =0.001) will be 7 but the actual *NTU* value of the sample by considering the response time would be 18. Therefore, for accurate *NTU* prediction the inlet flow temperature should be included in the prediction model.

6.6. Matching technique

Once the appropriate model is defined and solved, outlet fluid temperature can be predicted by the model. Assuming the model parameters have been correctly accounted for (e.g. heat loss to walls) the heat transfer coefficient can be found by matching the experimental temperature curve with curve predicted by the model. Matching the entire curve is practically very difficult due to experimental errors and modelling uncertainties. Therefore researchers have developed several methods to match the measured and

predicted curve in the single-blow method. A list of the popular matching methods will be given in this part and their strengths and weakness will be discussed.

6.6.1. Maximum gradient

A unique relationship existed between the maximum slopes of the response curves and the number of heat transfer units (*NTU*). This method called "maximum slope technique" and developed by Locke [13]. In this technique the maximum first derivative of the experimental data is matched with the predicted data from the model. This method reduces the computational effort in the analysis by reducing the matching to a single point. Coppage and London and Tong and London [14,16] both used the maximum gradient technique to match their experimental and predicted results. However, Kohlmayr [77] pointed out that this method was not suitable for $NTU<2$ since the outlet fluid temperature had no point of inflection. He extend the matching for lower *NTU* range ($0.5 < NTU < 5$) by introducing a method called centroid.

6.6.2. Selected point matching technique

As it was explained before, matching the entire curve is not always possible. Therefore, part of the curve or data points at certain interval can be used to match the curve. For instance, Darabi [87] introduced an alternative method to the Locke method. Instead of using entire breakthrough curve, he measured the time interval between 20 and 80% of dimensionless gas temperature and related this to the relationship called shape factor-*NTU* (Eq. 6.31). However, this method is only valid for an ideal step input and *NTU* range from 1.8 to 20. Liang and Yang [80] proposed a technique called selected point matching technique, which later developed by Cai et al. [79], to match the curves by matching selected points at different times on the response curve. In this method the measured value selected at a certain time matches with the corresponding theoretical value. When the difference between these value is within an acceptable value (<0.005), the theoretical value of *NTU* is take to be the result at that specific time. Then a new point at a larger time is selected and the procedure is repeated for minimum of five points. The arithmetic mean value of the calculated *NTU* is considered to be the *NTU* value of this test run [79].

$$Sf = \frac{\dot{m} C_{pf} \Delta\tau_{20-80}}{\rho_s C_{ps} L}$$ Eq. 6.31

6.6.3. Differential fluid enthalpy method (DFEM)

A matching technique called the differential fluid enthalpy method (DFEM) was developed by Baclic et al [88,89]. In this method both the temperature readings, upstream and downstream of the sample, were measured and intergraded with respect to time. These values were multiplied to fluid capacity rate and subtracted from each other to obtain the differential fluid enthalpy change up to a particular instance. This value then related to the parameters of the model to determine the *NTU* of the sample for arbitrary inlet fluid temperature variations. However, this analysis requires definition of the apparatus parameters such as *NTU* of fluid-to-wall, time constant of thermocouples, core matrix specific heat capacity, maximum fluid temperature rise and the time constant of the exponential inlet temperature signal. As a result, defining each of these parameters could introduce lots of uncertainties to the final result.

6.6.4. Direct curve matching

In this method the entire experimental and predicted data are matched by minimizing the least-square error. Heggs and Burns [90] analyzed their experimental data by four commonly used data reduction techniques, direct curve matching (least squares method), the maximum slope, shape factor and DFEM. They reported that *NTU* predicted by using the least squares method and DFEM were consistent but over predicted. However, the example of inlet and outlet temperature in this paper showed that they failed to generate a good step change and the inlet temperature increased gradually during the experiment and this could affect the outlet temperature curve. Any small variation in the outlet temperature curve is magnified by the first derivation therefore consistency of the maximum gradient is highly depends on the quality of the inlet temperature curve as it was shown in the section 6.5.5.

Loehrke [75] showed that mismatching the model and experimental result may predict different results with different matching method for the same heat exchanger. He generated the data from an analytical model and matched the data with the three matching technique (curve matching at multiple points, maximum gradient and DFEM) under different modeling assumption such as non-ideal inlet fluid temperature history, longitudinal conduction, variable heat transfer coefficient and effective core mass. He presented the effect of common mismatching between the model and the experiment. He also provided guidelines for determination of the potential error that could occur because of various mismatching between the experiment and the model. He stated that even if two different matching methods yielded similar estimates these estimates may be far from correct.

In more recent years, researchers [2,18,22,91,92] either used both the maximum gradient technique and curve matching at multiple points or just implement the later method. Therefore, the maximum slope method and whole curve matching were used in this study to obtain the heat transfer coefficient. The Joule-Thomson expansion effect was negligible for the samples tested for this experiment (low pressure drop) and excluded from the model. Since the effect of radial conductivity was only 8% for NTU=150 and samples for this study were small, this effect was not added in the model. The effects of heat flux from the sample to the sample holder, arbitrary inlet flow temperature and axial thermal conductivity were added in the model.

Chapter 7- Thermal test Apparatus

7.1. Experimental set-up

In order to measure the heat transfer rate a test apparatus was designed and manufactured. The single-blow method explained in the previous chapter was used for analysing the experimental data. The rig consists of a heating system, two fans, an orifice plate and the test section. All fittings, valves and pipes were made out of ABS for its low thermal conductivity. The rig was tested for leaks by pressurising it to 0.3 bar, which it held for 30 min.

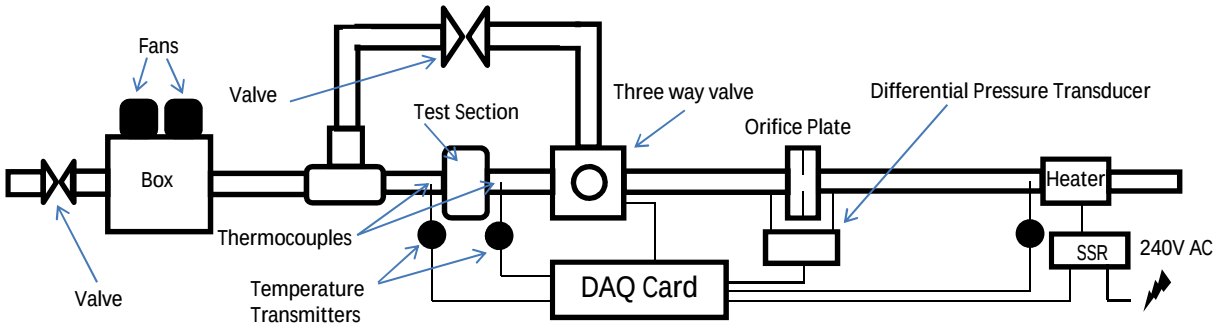

Fig. 7.1, A schematic diagram of the test rig used for the thermal and pressure drop measurements.

The suction power needed for the experiment was provided by two 1000 W high speed centrifugal fans placed inside a box, see Fig. 7.3a. Three fans were installed in the box but only two of them were used and the third fan was a redundant. The fan speed was controlled by adjusting the input current using an 8 Amp Variac variable transformer. It was found that at low current, the fans speed fluctuated and disturbed the flow rate. This was avoided by running the fans at high speed and controlling the flow by a ball-valve connected to the box (Fig. 7.3a). The valve reduced the negative pressure inside the box and lowered the suction power. To fine tune the flow rate the fans speed were adjusted by the Variac.

Moving from right to left, atmospheric air was sucked in by the fans and passed an inline AC heater. Having a constant inlet air temperature is essential for accuracy of the single-blow method. In order to provide this, a heating system was designed and manufactured to providing a constant inlet air temperature. The inline heater (AHF-14240 Omega) was used for heating the incoming air up to 20°C above ambient. On/Off control was used to control

the heater, which is powered by a 240V alternating current (AC). The heater was controlled by adjusting the duty cycle of the power supply. Duty cycle is the ratio of the pulse duration to the pulse period. In heaters, 25% duty cycle means the power is on 25% of the time and off 75% of the time (Fig. 7.2). Since the thermal mass of the heater element and the incoming air were low, a shorter cycle was required to generate constant temperature.

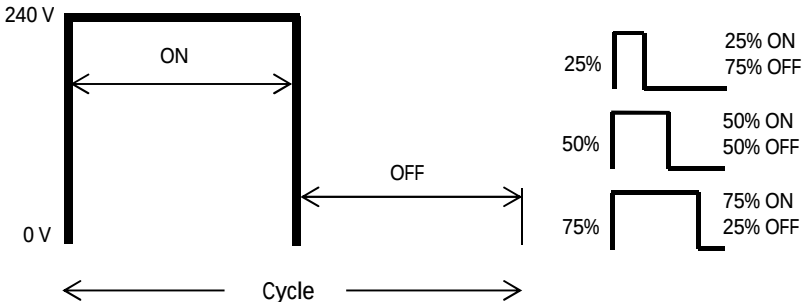

Fig. 7.2, Duty cycle is an expression of the On time to the Off time.

A LabView code was developed to generate the variable duty cycle pulse. This was linked to a PID code that controlled the heater temperature by adjusting the duty cycle. Since the AC current alternates at 50 Hz, the heater cycle was synchronised with the main current by using a Zero-Crossing Solid-State Relay. This type of relay switches the relay on or off when the AC mains voltage reaches the zero-crossing point of the sine-wave. The cycle for this experiment was set at 1/7th s (7Hz). The PID sent the signal from the DAQ card to the relay and controlled the temperature by adjusting the duty cycle of the signal. A 0.5 mm K-type thermocouple, positioned after the heater, provided the feedback loop to the PID code.

After the heater, air flowed through a stack of 10 layers of wire-mesh (No. 20) to condition the flow. The flow then passed through a 1500 mm length of pipe (2 inch nominal pipe) to fully developed the flow before reaching a calibrated flanged-type orifice plate that was used to measure the flow rate. The pressure tappings and their position were compatible with BS EN ISO 5167-1:19979. The pressure drop was measured by a differential pressure transmitter (Furness Controls - Model 332-4W) with an accuracy of ±0.25% (reading). To calculate the flow rate, the air density was calculated from the atmospheric pressure, temperature and humidity of the air after the heater.

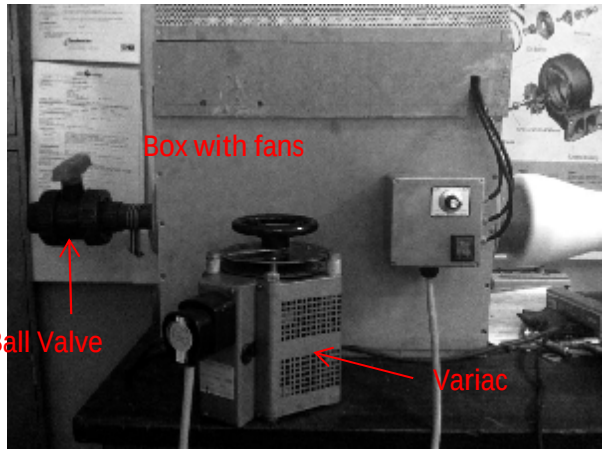

Fig. 7.3a, A view of the fan box with the ball-valve.

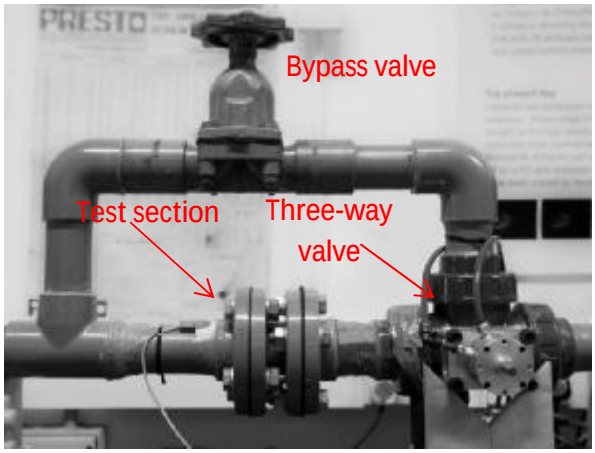

Fig. 7.3b, A view of the test section, bypass valve and the three-way valve with rotary actuator

To generate a repeatable temperature step change a three-way valve was installed to direct the incoming air either through the test section or the bypass. To operate the valve swiftly and at constant speed, a rotary pneumatic actuator (Norgren M/60284/90) was mounted on top of the valve and controlled by a solenoid valve, which could redirect the incoming air in less than 0.15 seconds (Fig. 7.3b). Since there was less restriction through the bypass than the test section, switching the flow from the bypass to the sample resulted in a sudden reduction in the air velocity. Due to the response time of the PID controller and heater, it took several seconds for the controller to stabilise the temperature. This significantly affected the profile of the inlet flow temperature. To eliminate this problem a globe valve was placed in the bypass and the flow rate adjusted such that it was similar to the flow rate though the sample.

Porous matrix samples were placed inside the test section in line after the three-way valve. The sample holder can be attached or detached from the rig by the flanges at both end of the holder. The flanges should be fastened by a torque meter up to 6 N/m to ensure the airtightness of the rig. Before placing a sample in the holder its circumference was wrapped in PTFE tape to seal the gaps between the sample and pipe wall and reduce the heat loss from the sample to the pipe wall.

The temperature before and after the sample was measured using two K-type butt-welded unsheathed 0.25 mm thermocouples which were positioned at the centre of the pipe. Fine thermocouples were used to ensure that the transient thermal response of the

thermocouple did not influence the results. The time constant of the test thermocouples was found to be 0.003 seconds at an air velocity of 20 m/s. Two 2-wire temperature transmitters (Farnell 300TX with ±0.2% accuracy of thermocouple range) were used to amplify and linearise the signals.

A 16-bit PCI-6221 National Instrument (NI) data acquisition card (DAQ) was used to receive and send the signals. A NI LabView code monitored and logged the data, and a PID LabView code controlled the On/Off switching of the heater. Experiments were performed at five different air velocities (from 1 to 6 m/s) and for each velocity four tests were conducted.

7.2. Experimental procedure

Each sample was wrapped in with PTFE tape and pushed in the holder. Then the holder was placed between the flanges and nuts were tightened up to 6 N/m. The test rig was run for 30 minute to warm up the rig for ensuring constant inlet air temperature. Once the air temperature stabilized, the three-way valve directed the air to the sample and the air flow adjusted to the desirable flow rate by changing the fan speed. After adjusting the flow through the sample, the hot air was redirected to the bypass valve by the three-way valve. Then the flow rate matched with the air flow passing through the sample. This was done since a sudden change in flow rate affected the heater's PID controller and it needed time to readjust the air temperature based on the new flow rate. Therefore, the air flow through the sample and the bypass valve were matched to prevent this sudden change in air flow rate.

The sample then was cooled to the room temperature by sucking the room air into the sample. After cooling the sample, the three-way valve switched the air from the bypass to the test section. This was done by sending an electric signal to a solenoid valve which operated the three-way valve. The signal also triggered the DAQ card to start logging the data. The air flow rate and temperature history across the sample were measured till the air temperature after the sample did not changed with time. After logging the data, the process repeated for the next flow rate.

Chapter 8 – Thermal Data reduction

8.1. Experimental temperature data

Shown in Fig. 8.1 is an example of the temperature data recorded for the Mid 2 sample. The graph shows the step change temperature change applied to the sample and the resulting outlet temperature response. Both temperature data had electronic noise but inlet temperature had more fluctuation than the outlet temperature. This could be the effect of turbulence and circulation of the air flow after the three-way valve. However, the air flow turbulence was conditioned by the sample and the outlet temperature had mainly electronic noise. The outlet temperature can be seen to be lower than the inlet temperature even after 40 seconds. The reason of this temperature difference was the heat loss from the sample to the wall. The heat loss was estimated by matching the temperature curve with the curve generated by the model and will be discuss.

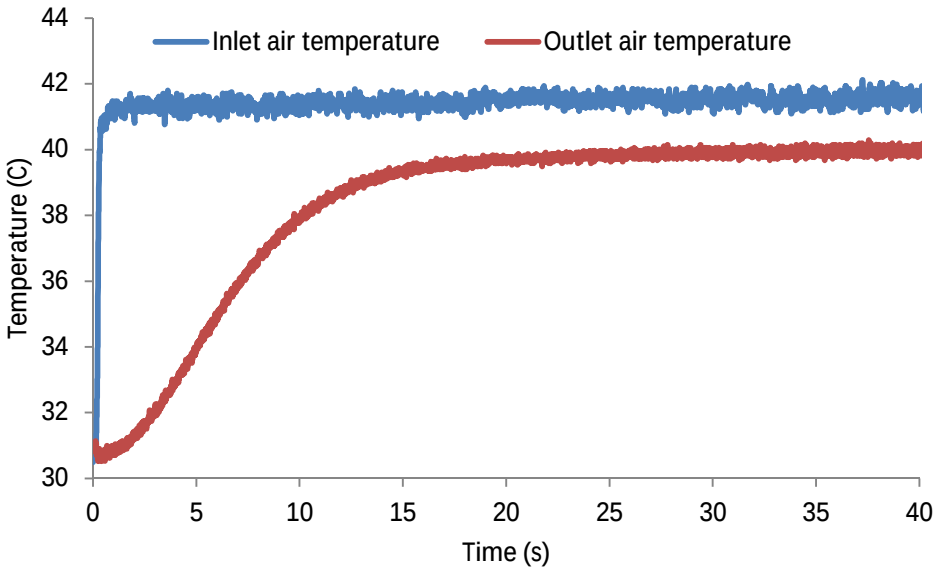

Fig. 8.1, A typical inlet and outlet temperature data recorded from the test rig.

8.2. Non-dimensionalising data (time-temperature)

Experimental data, time and temperature should be non-dimensionalised before matching it with the predicted data. Dimensionless time can be calculated by Eq. 8.1. The data from the experiment showed that there was some discrepancy between the trigger time and opening the three-way valve. The reason for this variation was thermal expansion of the valve

components. Although the same signal was sent to the DAQ card and the valve, sometimes the valve jammed and delayed the opening time. During the experiment, the valve components were heated by the incoming air and as a result of this they expanded which consequently increased the operating time. This variation was rectified by subtracting the time from the time before rise of the inlet air temperature. This will be discussed in section 8.6.2. In addition, the possible effect of this delay on inlet temperature profile was compensated by estimating inlet temperature response time which will be discussed later in this chapter.

$$\tau_n = \frac{\dot{m}_f C_p t_a}{M_s C_s} \qquad \text{Eq. 8.1}$$

The air temperature was non-dimensionlised by Eq. 8.2. In this equation t_{fmax} is the maximum air temperature before the sample (blue line in Fig. 8-1) and t_0 is the initial temperature of the air inside the sample. The inlet air temperature was averaged for calculating t_{fmax} and the minimum outlet temperature was used as t_0.

$$T_f = \frac{t_f - t_0}{t_{fmax} - t_0} \qquad \text{Eq. 8.2}$$

8.3. Smoothing the data

Once nondimensionalised, the temperature data was smoothed. Since the first derivation of the temperature data is going to be calculated, even a moderate amount of noise could severely corrupt the result. Smoothing was performed using the Matlab Curve Fitting Toolbox.

The data from the experiment showed that occasionally they contained outliers which existed as a result of electronic noise. The smoothed values can become distorted, and not reflect the behaviour of the bulk of the neighbouring data points if these points do not remove from the bulk data. To overcome this problem, the outliers were eliminated before applying the above method. The outliers were found automatically by defining the upper and lower limits (10% from the mean) of the data based on their neighbouring data. If the data point was out of the range it was eliminated from the data.

After eliminating the outliers Moving Average method was used to smooth the data by replacing each data point with the average of the neighbouring data points which were defined within the span. The process was done by the following equation [93]:

$$y_{ma}(i) = \frac{1}{2N+1}(y(i+N) + y(i+N-1) + \cdots + y(i-N)) \quad \text{Eq. 8.3}$$

where $y_{ma}(i)$ is the smoothed value for the *ith* data point, *N* is the number of neighbouring data points on either side of $y_{ma}(i)$, and the span is *2N+1*.

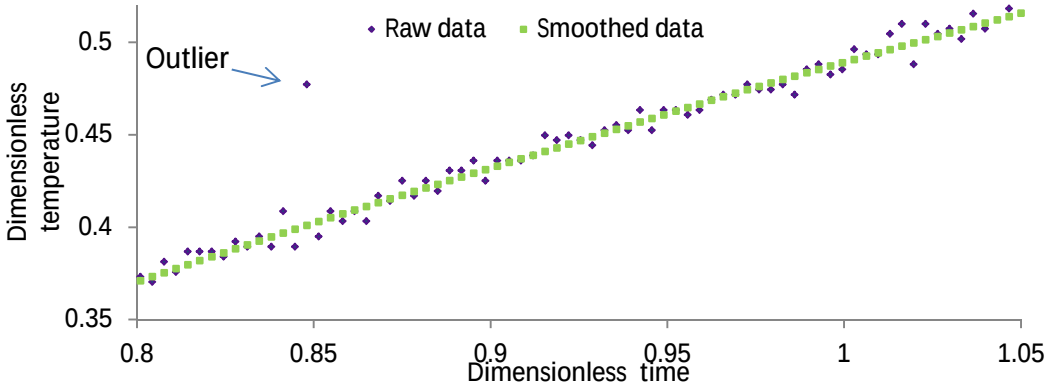

Fig. 8.2, A typical dimensionless temperature data smoothed by the Moving Average method

8.4. Curve fitting the data

Following the use of the Moving Average method further smoothing was necessary to make it possible to perform the first derivation. To do this a curve was needed to fit through the data to ensure that the first derivatives are continuous at each data point. Nonparametric fitting (splines) were used for this as it was not necessary to interpret the curve coefficients.

A spline function is method of applying low-order polynomials to subsets of data point. The polynomials between the points can be as simple as a straight line (Linear Spline) or a third-order curve. To ensure that the *n*th derivatives are continuous at each point, a spline of at least *n+1* order must be used. Third-order polynomials or cubic splines that ensure continues first and second derivatives are most frequently used in practice and used for this study [84].

Once the data were imported to the software the level of smoothness (order of the spline) could be adjusted by varying the parameter p. This changed the curve from a least square

straight-line approximation (*p=0*) to a cubic spline (*p=1*) interpolant. The following equation was used in Matlab to fit the spline curve to the data[93].

$$p\sum_{n}(y_n - s(x_n))^2 + (1-p)\int(\frac{d^2s}{dx^2})^2 dx \qquad \text{Eq. 8.4}$$

$x_n$and y_n are the data point and *s* is the function applied to the data.

After fitting the curve through the data, the goodness of the fit should be evaluated. The Curve Fitting Tool provides the goodness of fit measures:

- Residuals
- Goodness of fit statistics

The software provides both numerical and graphical measures. The goodness of the fits statics are numerical measures and the residuals are graphical measures. The graphical measure is more beneficial than the numerical measure since it allows the user to view the entire data set at once. The numerical measures are more narrowly focus on a particular aspect of the data such as The Sum of Squares due to Error *(SSE)* or *R-square*.

8.4.1. Residuals

The difference between the response value *y* and the predicted response value $\hat{y}$ is mathematically called the residual for a specific predictor value.

$$r = y - \hat{y} \qquad \text{Eq. 8.5}$$

Here the residual is the difference between the fitting and the dimensionless experimental data. If the residual approximate the random errors it suggests that the data fits well with the fitting. However, if it displays a systematic patter, it is a clear sign of poorly fitted curve. Fig. 8.3 shows the dimensionless data (blue dots), smoothed data (green dots) and the fitting curve (red line). A graphical display of the residuals is also shown in Fig. 8.3 for a short period of time. The graph shows that this part of the data fit well with the curve and as a result the residuals appeared randomly around zero.

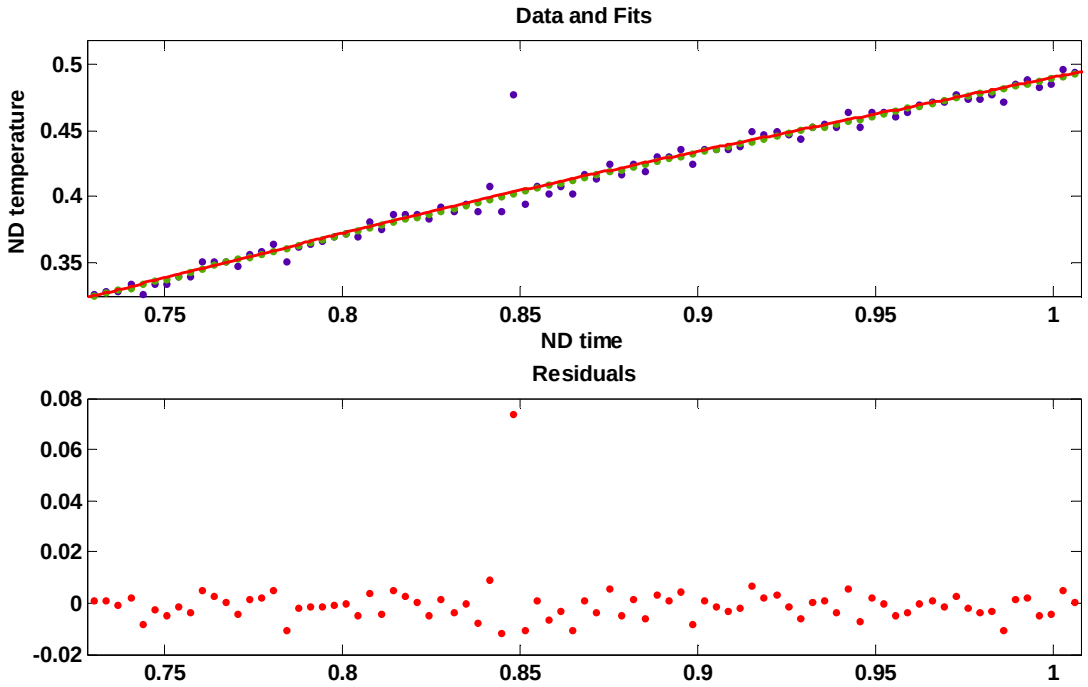

Fig. 8.3, An example of a fitted curve (red line) to the smoothed data (green dots), the dimensionless data (blue dots), the residuals error of the fitted curve and the smoothed data

8.4.2. Goodness of Fit Statistics

In order to evaluate the goodness of the fit statistic, four methods which were provided by The Curve Fitting Toolbox were used for this study:

8.4.2.1. The sum of squares due to error (SSE)

Sum of Squares Due to Error measures the total deviation of the response values from the fit to the responses values. A fit that produces SSE closer to 0 is a better fit.

$$SSE = \sum_{i=1}^{n} (y_i - \hat{y}_i)^2 \qquad \text{Eq. 8.6}$$

8.4.2.2. R-Square

This is the square of the correlation between the experimental data and the data from the fitted curve. *R-square* is defined as the ratio of the sum of squares of the regression (SSR) and the total sum of squares (SST).

$$R - square = \frac{SSR}{SST} = \frac{\sum_{i=1}^{n}(\hat{y}_i - \bar{y})^2}{\sum_{i=1}^{n}(y_i - \bar{y})^2} \quad \text{Eq. 8.7}$$

R-square value could be any number between 0 and 1 and a value closer to 1 indicating a better fit. For instance, an R-square=0.92 means that the fitting covers 92% of the total variation in the data about the average.

For the medium pore size sample in Fig. 8.3 SSE=1.986E-4 and R-square=1.000.

8.5. Differentiating the curves:

In order to find the maximum gradient of the curve, the first derivative of the curve should be calculated. The maximum value of the first derivative or inflection point of the temperature is the maximum gradient of the data.

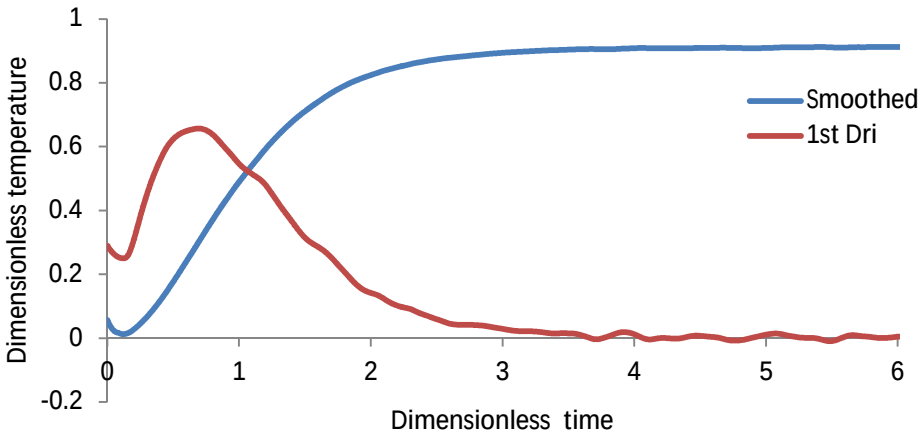

Fig. 8.4, An example of smoothed data with the 1st derivative of the data

The first derivative of the curve was calculated in Matlab by a built in function "fx=differentiate(FO, X)". This function applied the centred difference equation to numerically calculate the first derivative:

$$\frac{df}{dx} = \frac{f(x + \Delta x) - f(x - \Delta x)}{2\Delta x} \quad \text{Eq. 8.8}$$

An example of the maximum gradient and the fitted curve can be seen in Fig. 8.4. Even after careful smoothing the data and fitting the curve, fluctuations were noticeable after the inflection point. This was due to slight variations in the fan velocity and the heater temperature fluctuation. For this case the first derivation was carried out for entire data and it can be seen that for the first 0.2 seconds the first derivation decreased before increasing till the inflection point. This decreasing was happened due to slight temperature difference between the sample initial temperature and the air trapped between the three-way valve and the sample. To avoid the effect of this on the fitted curve the first 0.2 seconds of the data was removed before fitting the curve.

8.6. Predicting outlet air temperature with the model

In order to predict the outlet temperature history accurately with the single-blow model samples physical properties should be estimated correctly.

8.6.1. Inlet air temperature response

It is physically difficult to execute an ideal step change but as it can be seen from the Fig. 8.1 the test rig generated an acceptable step change and the inlet temperature was constant for the entire measurement. As it discussed in the Chapter 6, the inlet fluid temperature history was characterised as an exponentially increasing function of time:

$$T_f(0,t) = 1 - e^{-\frac{\tau}{\psi}} \qquad \text{Eq. 8.9}$$

By applying the above equation the effect of deviating from an ideal step can be compensated in the prediction model. By fitting a curve generated by the Eq. 8.9 to the inlet air temperature history ψ can be calculated. Fig. 8.5 shows a typical inlet temperature history and a curve with ψ=0.007. The temperature measurement started 0.27 s before opening the valve to record the initial temperature of the fluid and sample. The inlet temperature response was calculated for each experiment and the results were applied to the model.

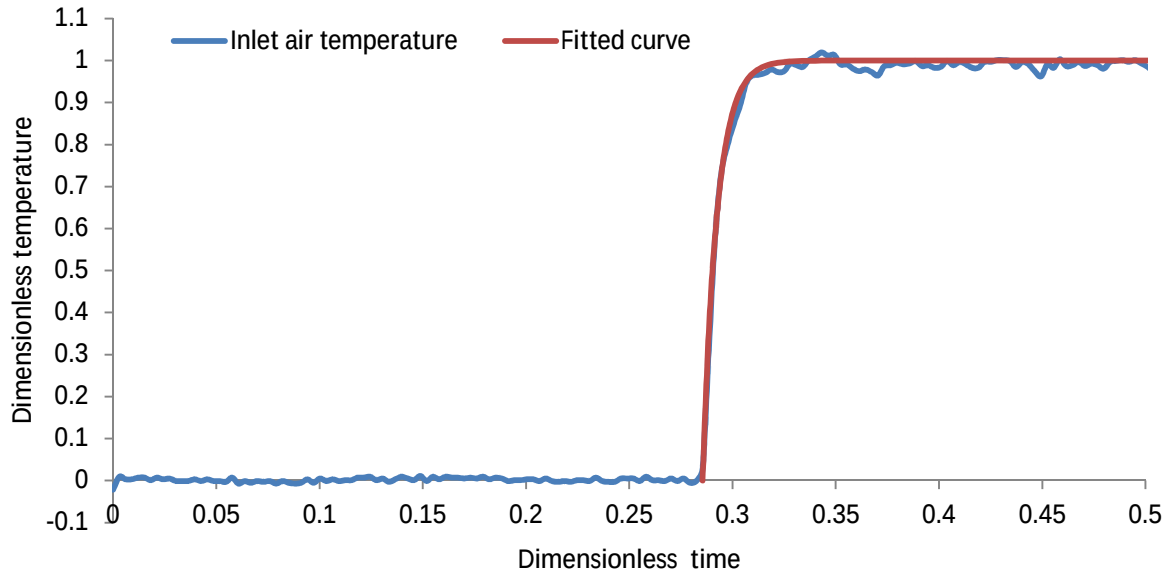

Fig. 8.5, A typical inlet flow temperature profile and a curve fitted to model the data

8.6.2. Dimensionless effective thermal conductivity

Majority of the parameters needed for the model can be measured or estimated with reasonable accuracy. However, one of the parameters, effective thermal conductivity of the sample, was difficult to estimate.

As Aichlmayer and Kulacki [94] explained in their introduction to measuring the thermal conductivity of the packed beds, predicting the effective thermal conductivity of saturated porous media is one of the greatest unsolved problems in heat transfer science despite decades of experimental and theoretical work. They argued that the problem is unsolved because the effective conductivity is a phenomenological characterisation of a solid-fluid medium rather than a thermo-physical property. As a result, it is characterised in macroscopic terms such as the thermal conductivity and volume fraction. However, the effective thermal conductivity also depends on the geometry and arrangements of sold-fluid medium; and generally these information are not available from experiments. Consequently, for accurate measurement of this parameter one should measure it experimentally and this is beyond the scope of this research. However, in order to run the model this parameter should be estimated.

To the best knowledge of the author, the effective thermal conductivity of this type of metal foam has not been carried out yet. Majority of the studies have been done on packed beds,

sintered metals and cell type metal foams. The structure of the metal foam manufactured for this study was different to cell type metal foam and sintered metal balls but it has similarities to both of them. For instance, cell type metal foam has high porosity (80%-95%) but sintered metal balls has low porosity (40%-55%) and the foams manufactured for this study had 63% porosity. Therefore, results from both types of porous media were studied to estimate the effective thermal conductivity of the foams.

$$k_e = k_f\left(\frac{k_s}{k_f}\right)(1-\varepsilon)^{0.53} \qquad \text{Eq. 8.10}$$

$$k_e = 0.35\left(\varepsilon k_f + (1-\varepsilon)k_s\right) + \frac{1-0.35}{\left(\frac{\varepsilon}{k_f} + \frac{1-\varepsilon}{k_s}\right)} \qquad \text{Eq. 8.11}$$

Boomsma and Polikakos [95] developed a geometrical effective thermal conductivity model of a saturated cell type metal foam, based on the idealised three-dimensional basic cell geometry of a foam, the tetrakaidecahedron. They validated their model with Bhattacharyaet al. [4] empirical correlation (Eq. 8.11). Both results and the results from the Alexander [96] [97] model were plotted in Fig. 8-6. As it can be seen from the graph, the data for both models were extrapolated beyond the porosity of cell metal foams and sintered metal balls. This was done to cover the porosity (63%) of the foams for this study. The result from sintered metal balls (k_e=18.4) was lower than the results from cell type metal foam (k_e=25.6). Since the foams had the structure between these porous media, an average value from both models at 63% porosity was estimated for the foams effective thermal conductivity. The experimental estimated value of the metal foams will be calculated in section 9.3 and the results will be compared with both sintered metal balls and cellular metal foams correlations.

After estimating the effective thermal conductivity of the samples, dimensionless effective thermal conductivity can be calculated from Eq. 8.11. Dimensionless effective thermal conductivity of the wall was negligible and did not have an effect on thermal results.

$$\lambda = \frac{k_e A_{cs}}{\dot{m}_f C_{pf} L} \qquad \text{Eq. 8.11}$$

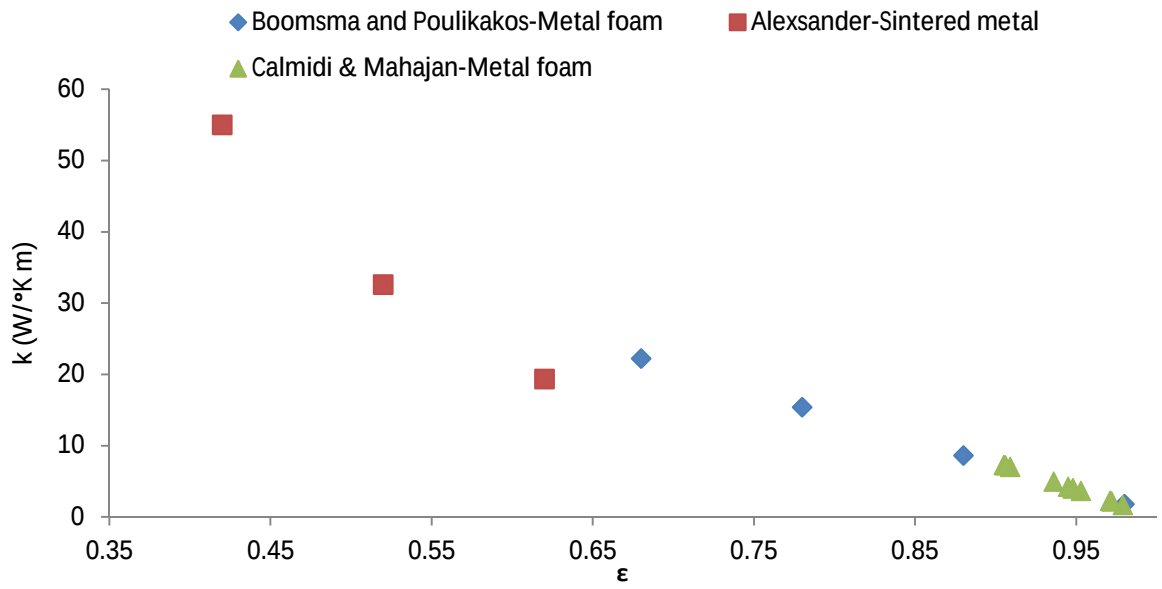

Fig. 8.6, Estimated effective thermal conductivity of the metal foams plotted with the correlation results from other studies

8.6.3. Heat capacity ratio

The ratio of sample's heat capacity to wall heat capacity ratio is called heat capacity ratio. This value was calculated by estimating length of the sample holder based on sample length and wall thickness. In this experiment the mass of PTFE tape which was wrapped around the sample was negligible compared to the mass of the holder. Therefore the ratio calculated based on the sample and wall mass.

$$R_{tc} = \frac{M_s C_{ps}}{M_w C_{pw}} \qquad \text{Eq. 12}$$

8.7. Estimating heat transfer coefficient

Once the all required parameters for the model were calculated, the outlet flow can be predicted by guessing the *NTU* and NTU_w values. The first derivative of the predicted data was calculated and if both, the maximum gradient and maximum exit flow temperature, matched with the experimental data, the guessed results represented the sample *NTU* value. If the values did not match, the process iterated till the data matched within the error of ±0.1.

After matching the maximum gradient and the maximum outlet temperature, next step would be matching entire curve. This step was done to check the accuracy of the results from the maximum gradient.

Chapter 9 – Thermal results

9.1. Matching experimental and prediction data

As it was discussed in chapter 8, two methods were used to match the model and experimental data. It was found that the maximum gradient method was faster and easier than fitting the entire curve. However, the sample's effective thermal conductivity (k_e), heat capacity ratio (R_{tc}) and heat loss to the wall (NTU_w) should be known for an accurate value of NTU to be obtained. This is less of a problem for samples with negligible k_e and NTU_w. A classic example of this type of sample is a pack of stainless steel wire mesh. This type of sample has very low contact surface area (wire mesh screen edges) between the wall and the sample which significantly reduces the heat loss to the wall. In addition, stainless steel has relatively low thermal conductivity and high heat capacity. As a result, the maximum gradient method can be applied to estimate NTU for this type of samples by assuming k_e and NTU_w are negligible.

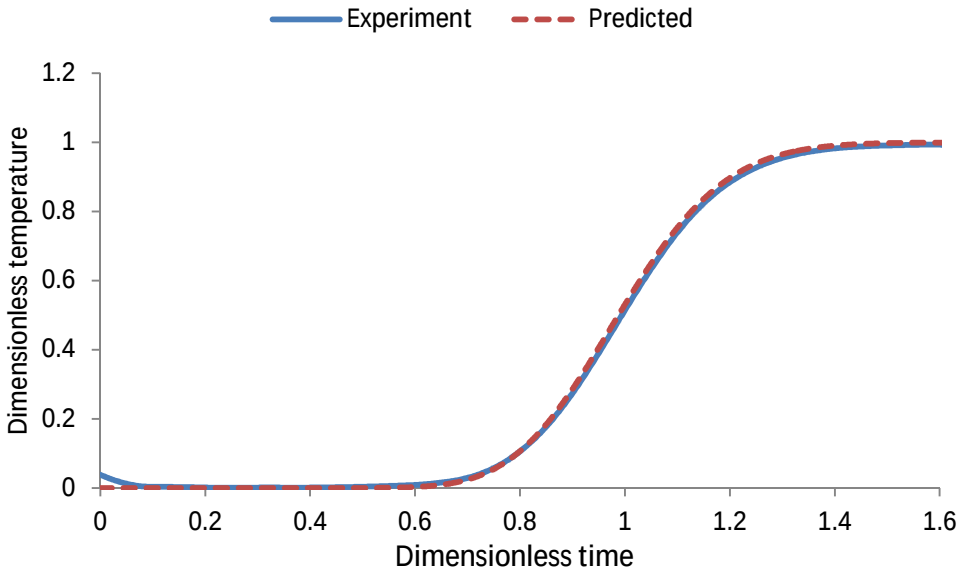

Fig. 9.1, Experimental and predicted outlet air temperature history of the stainless steel wire mesh sample at 2.65 m/s air velocity.

Shown in Fig. 9.1 is the predicted result (red line) which was collapsed on the experimental data (blue line) for a wire mesh sample at air velocity of 2.65 m/s. The graph shows that the outlet air temperature reached the inlet air temperature, indicating that this sample had

negligible heat lost to the wall. To obtain the predicted temperature curve R_{tc}, k_e and NTU_w were assumed negligible.

However, this is not the case for the metal foam samples. These had large heat transfer surface area between the sample and the wall which increased heat transfer loss to the wall even with PTFE tape wrapped around the sample. Moreover, they were made from aluminium which has high thermal conductivity and has low heat capacity (for the same volume) compared to stainless steel. In other words, R_{tc}, k_e and NTU_w should be known to predict the outlet temperature history profile.

In Chapter 8 (section 8.6.2) the effective thermal conductivity was estimated using a correlation which did not fully represent this type of metal foam hence it only gave a crude estimation.

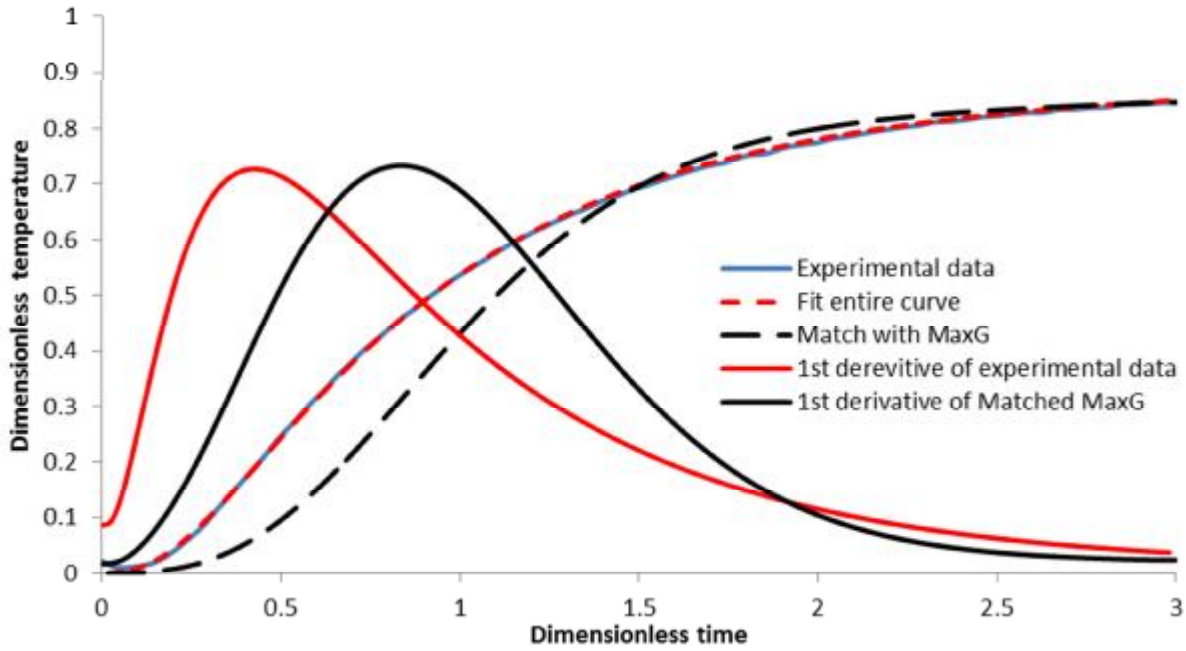

Fig. 9.2, Experimental outlet air temperature history (sample Small 3 at 2.64 m/s air velocity) fitted with two different matching methods and different k_e

Show in Fig. 9.2 is the effect of using inaccurate k_e on *NTU* value predicted with the maximum gradient method. The blue line is the outlet air temperature history for the Small 1 sample at 2.64 m/s. The red line is the 1st derivation of the experimental data and its maximum value was 0.73. The sample *NTU* value then can be predicted by matching the maximum gradient of the experimental data and predicted data. The black dashed line is the

predicted temperature curve which was predicted by the model based on the maximum gradient and maximum temperature of the experimental data, samples and R_{tc}=1.57 value and assuming that the sample k_e is 0.1 W/(m.K). In this example all the modelling inputs were correct apart from the k_e assumption. Based on this wrong k_e assumption, NTU=9.34 and NTU_w=0.23 were wrongly estimated. The graph clearly shows that predicted curves, dashed red curve (correct match) and the dashed black curve (wrong match), had the same maximum gradient but different shape. In this example, NTU =6.8, NTU_w=0.18 and k_e=25 W/(m.K) were predicted from direct curve matching. In other words, in this example applying the maximum gradient without knowing k_e could lead to 27% error in NTU result and 21% error in NTU_w. Therefore the maximum gradient method only predicted a correct NTU when all the correct variables (in this case k_e =25) were added into the model.

It was found that the effective thermal conductivity of the samples could be predicted by direct curve matching method. Shown in Fig. 9.2, the red dashed line was fitted to the experimental data (blue line) by guessing the three modelling variables, NTU, k_e and NTU_w. The author was aware that there could be a risk of having a similar answer with different combination of these three variables. However, this was not possible due to the nature of the heat transfer within the sample and to the wall. At Zone one, since the time is very short the heat mainly transfers by the convection to the sample. Therefore the NTU value is mainly dominant at this Zone. Once part of the air heat absorbed by the sample, the heat within the sample transfers mainly by conduction through the sample. Therefore sample's thermal conductivity is dominant at Zone 2. When the heat saturated the sample, it transfers from the sample to the wall. Since the conduction between the sample and the wall is lower than the conduction within the sample, it takes longer to reach the equilibrium state with the wall and surrounding. Therefore, this Zone is mainly affected by the NTU_w. This was tested by changing one of the variables and keeping the others constant. The results showed that the influence of each variable was dominant at certain part (Zone 1, 2 and 3) of the breakout curve, which are depicted in Fig. 9.3, 9.4 and 9.5.

For instance, the effective thermal conductivity was dominant at mid temperature (Zone 2). Fig. 9.3 shows the predicted curves with different λ (Eq. 8.11). It can be seen from the graph that the effect of λ is more visible at middle of the Zone 2.

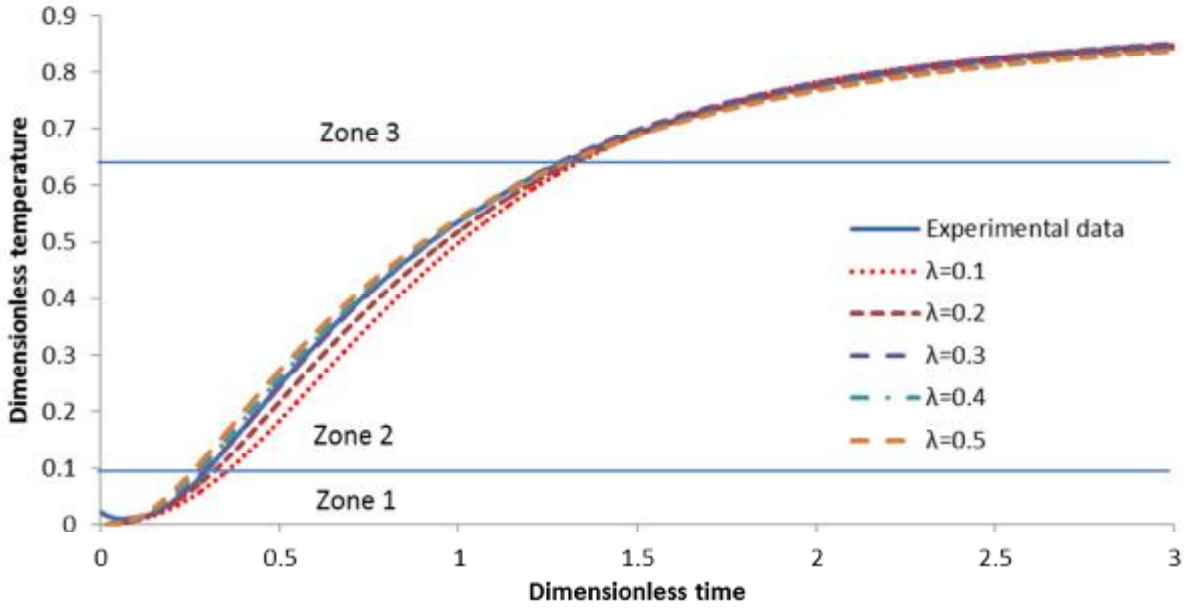

Fig. 9.3, Experimental outlet air temperature history (sample Small 3 at 2.64 m/s air velocity) fitted predicted curve with different λ (dimensionless k_e).

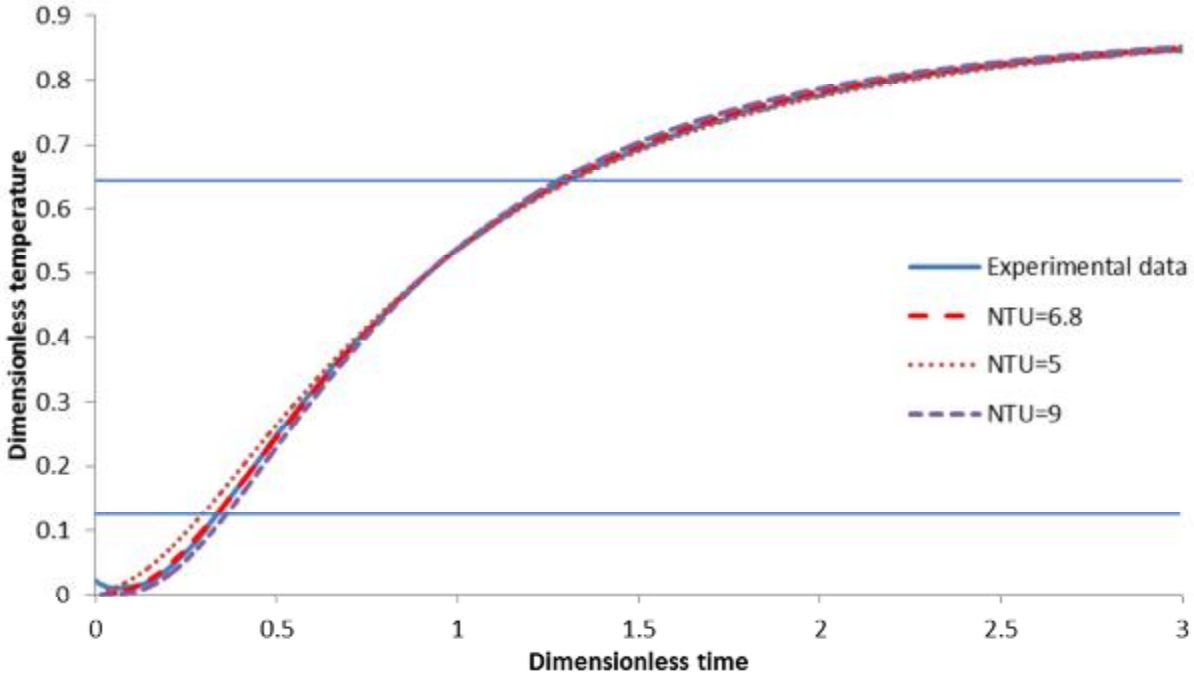

Fig. 9.4, Experimental outlet air temperature history (sample Small 3 at 2.64 m/s air velocity) fitted with predicted curve with different *NTU*.

The modelling results show that *NTU* mainly affects the predicted curve at Zone 1. The predicted curves were generated by keeping all the variables constant and just changing the *NTU*. The *NTU* effect on the predicted curves is shown in Fig. 9.4. The graph shows that by increasing *NTU* the predicted curve is shifted from left to right and the gradient of the curve

increased. In fact by increasing *NTU* the predicted curve stays longer in Zone 1 which means the sample can absorb more heat. It was found that it was faster to start matching curves from Zone 1 since the shape of the curve in this zone is relatively independent from the other variables. The graph shows that *NTU* also affects the predicted curve at Zone 3 but the effect is less negligible in that area.

Shown in Fig. 9.5 are the experimental data fitted with a predicted curve and two other predicted curve calculated at NTU_w. All three curves were predicted based on Small 3 sample properties but with different wall heat transfer rate scenarios. The graph shows that NTU_w effect is dominant at Zone 3 and it has almost no effect on Zone 1. A possible reason for this behaviour could be the time that take the heat to transfer within the sample and then to the wall. Therefore, the shape of the curve at Zone 3 is mainly depends on the heat transfer rate to the wall. Reducing this heat transfer could improve the thermal performance of the sample but as Fig. 9.5 shows, having higher NTU_w does not affect sample's *NTU* (Zone 1).

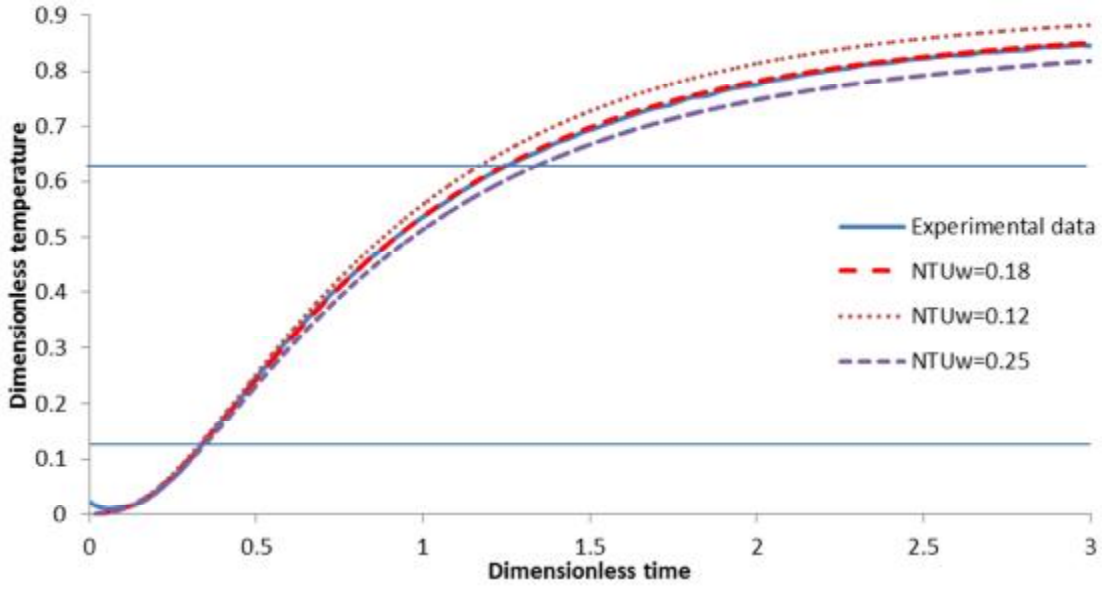

Fig. 9.5, Experimental outlet air temperature history (sample Small 3 at 2.64 m/s air velocity) fitted with predicted curve with different NTU_w.

9.2. *NTU* results

Shown in Fig. 9.6 are the *NTU* values plotted against Reynolds number for the foam samples. The Reynolds number was calculated for the flow within the sample. The average diameter

of the salt particles was used as a characteristic length. Reynolds number was calculated using:

$$Re = \frac{\dot{m}_f d}{\mu A_{cs} \varepsilon} \qquad \text{Eq. 9.1}$$

where, A_{cs} is the cross section area of the sample and *d* is the characteristic length.

The Small samples had the highest values of *NTU and* there was little difference between the samples *NTU* value particularly at low Reynolds number. As the salt diameter increased the *NTU* decreased also the scatter between samples grew.

The ball bearing and wire mesh sample were tested and their *NTU* results were plotted against Reynolds number in Fig. 9.7a and 9.7b. For the ball bearing sample the characteristic length was the ball bearings diameter (2mm) and for the wire mesh sample the hydraulic radius calculated with Eq. 9.3 was used. The wire mesh had more than ten times higher *NTU* than the highest *NTU* for the metal foam. However, the ball bearings had similar *NTU's* with the Large foam samples.

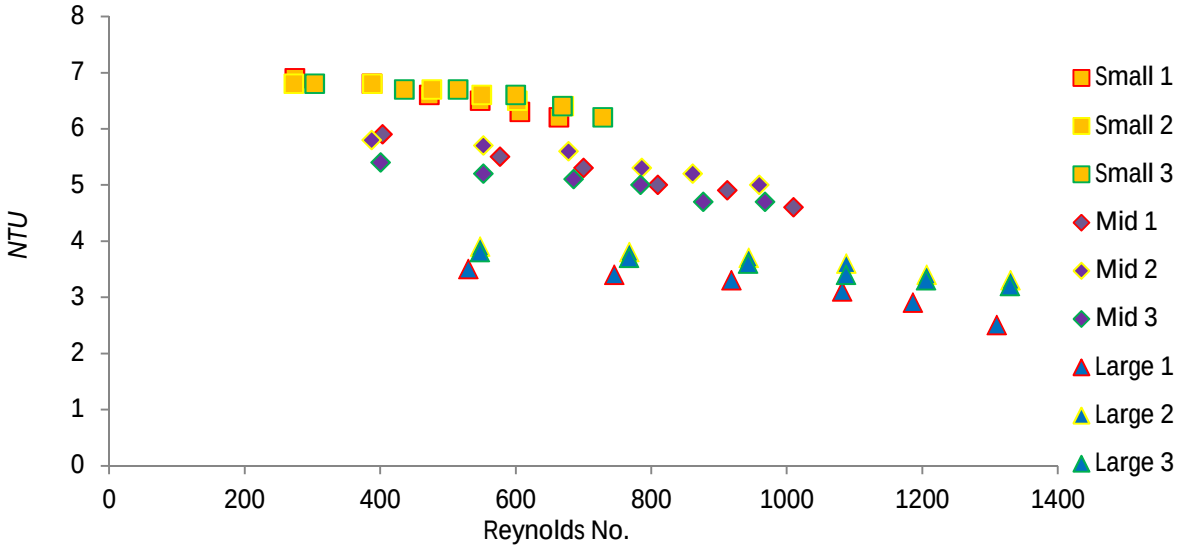

Fig. 9.6, Metal foams *NTU* values against Reynolds number based on average pore size diameter

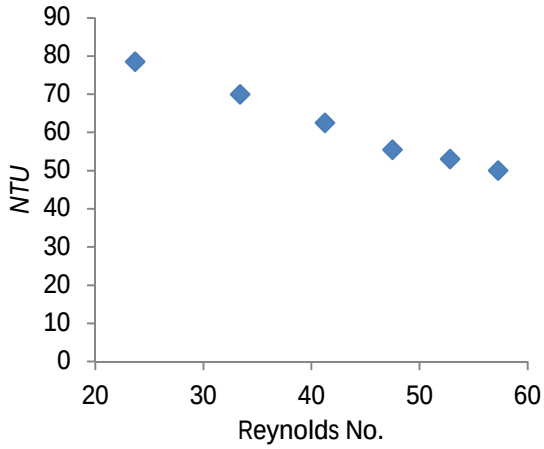

Fig. 9.7a, Wire mesh sample NTU against Reynolds number

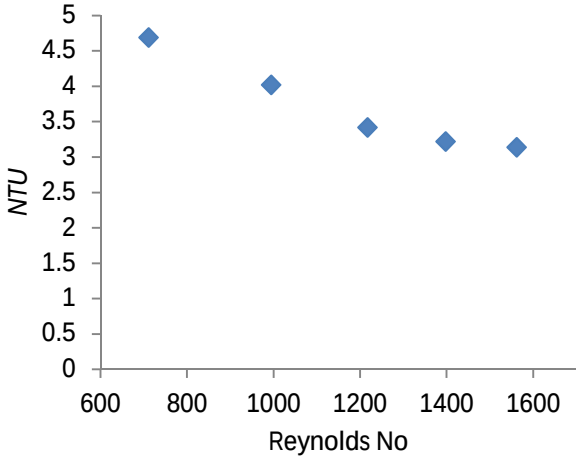

Fig. 9.7b, Ball bearing sample NTU against Reynolds number

9.3. Metal foams effective thermal conductivity

The effective thermal conductivity derived from the breakout curves of the metal foams was calculated at each flow rate and the results were averaged and tabulated in Table 9.1. The values were close to the results predicted in section 8.6.2 (Fig. 8-6). Shown in Fig. 9-8 is the effective thermal conductivity of the foams plotted with the correlation data found by three other researchers. The large samples had, due to their relatively small surface area, low *NTU's* and their outlet temperature was more susceptive to factors such as heat loss to the wall and inlet air profile. As a result it was more difficult to match the experimental and predicted data. Hence, k_e of the Large samples were more than the other samples.

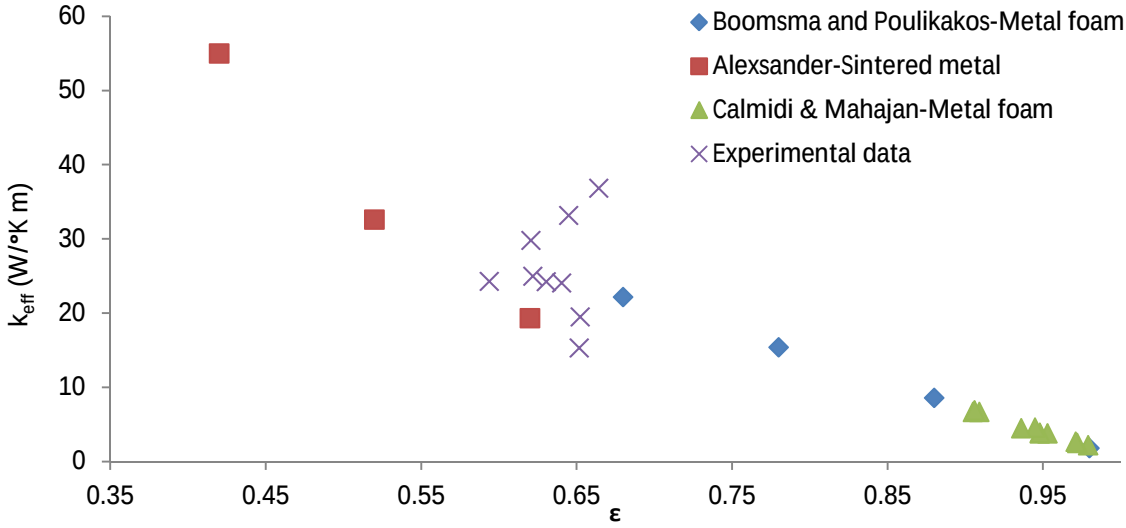

Fig. 9.8, Effective thermal conductivity of the metal foam samples against porosity

Table 9.1. Average effective thermal conductivity of the samples with their standard deviation.

	Small 1	Small 2	Small 3	Mid 1	Mid 2	Mid 3	Large 1	Large 2	Large 3
Mean k_e	25.00	24.25	24.28	29.83	33.17	24.07	36.83	15.33	19.50
Standard deviation	0.33	0.42	1.23	1.47	0.98	1.28	5.15	3.50	2.43

9.4. Heat transfer coefficient and samples specific surface area

Once the *NTU* value is predicted by matching the experimental data and modelling data the heat transfer coefficient, *h*, can be calculated from *NTU* (Eq. 6.15). In addition to *NTU,* the heat transfer surface area must be known for calculating *h*. For the ball bearing sample it was assumed that the steel balls were impenetrable spheres and the pack was statistically homogeneous. The heat transfer surface area was obtained by[98]:

$$A_s = 4\pi Rad^2\varphi \qquad \text{Eq. 9.2}$$

where φ is the number of spheres and *Rad* is the radius. The number of spheres was calculated knowing the mass of 2000 spheres and weighing the whole sample to estimate the total number. It was estimated that there were ten thousand ball bearings in the sample following this method. The surface area and specific surface area of the ball bearing sample were found to be:

$$A_s = 125663\, mm^2$$
$$A_{sp} = 1678.5\, m^{-1}$$

The specific surface area also can be calculated with [99]:

$$A_{sp} = \frac{6(1-\varepsilon)}{d} \qquad \text{Eq. 9.3}$$

which yields

$$A_{sp} = \frac{6(1-0.43)}{0.002} = 1687.8\, m^{-1} \quad \text{Eq. 9.4}$$

This result is in good agreement with the results from the previous method.

Table. 9.2 – Specific surface area of the metal foams

Sample Name	Porosity	Ave pore size (mm)	Surface area (m^{-1})
Small 1	0.622	1.05	3553.41
Small 2	0.631	1.05	3603.47
Small 3	0.594	1.05	3393.36
Mid 1	0.621	1.55	2402.17
Mid 2	0.645	1.55	2496.07
Mid 3	0.640	1.55	2478.53
Large 1	0.664	2.18	1828.36
Large 2	0.652	2.18	1793.95
Large 3	0.652	2.18	1795.24

The specific surface of the metal foams area was obtained by assuming that all the salt particles and hence the pores formed were spheres. Therefore the equation 9.3 was used to obtain the specific surface area, expect that the solid and gas phases are inverted and ε was used instead of (1-ε). The specific surface area of the foams were calculated and tabulated in Table 9.2.

Specific surface area and hydraulic radius of the wire mesh sample was calculated with the method outlined by Tong and London [16] method. The specific surface area (A_{sp}) can be calculated by knowing the ratio of the wire diameter (d_{wire}) to the distance between wires (X).

$$x_t = \frac{d_{wire}}{X} \quad \text{Eq. 9.5}$$

$$A_{sp} = \frac{\pi}{x_t d_w} \quad \text{Eq. 9.6}$$

Shown in Fig. 9.9a is an image of a layer of the wire mesh sample under microscope. The scale of the image shows that 4 pore per 500 μm. A simple calculation shows that based on this image it should be 203 pores per inch (PPI) which is in good agreement with the number provided by the wire mesh supplier (200 PPI).

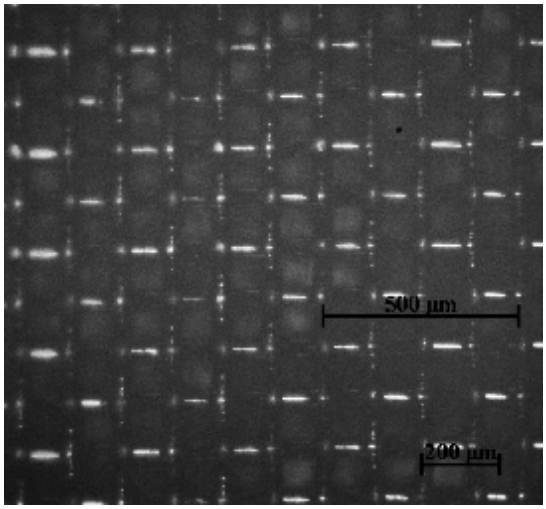

Fig. 9.9a, Wire mesh screen (No. 200) under microscope

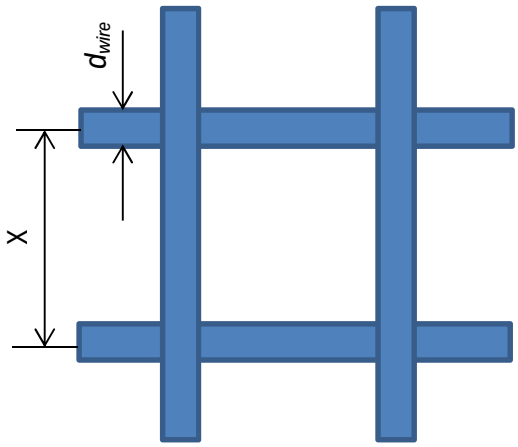

Fig. 9.9b, A schematic view of wire mesh

Based on this image *X* was 125 μm and d_{wire} was 41.6 μm. Specific surface area then can be calculated with Eq. 9.6:

$$A_{sp} = \frac{\pi}{3 \times 41.6\mu} = 25132\ m^{-1}$$

Hydraulic radius of the wire mesh was calculated by:

$$r_h = \frac{\varepsilon}{A_{sp}} = \frac{0.7}{25132} = 2.7852\ E-05\ (m) \qquad \text{Eq. 9.7}$$

9.5. Heat transfer coefficient results

Shown in Fig. 9.10 are the heat transfer coefficients of the metal foams increasing with Reynolds number (calculated for the flow within the foam). The graph shows that the Small samples had the highest *h* value. However, at lower Reynolds number *h* was similar for both the Small and Mid samples. The Large samples had much lower *h* than two other pore sizes. Even at low Reynolds number the Large samples had nearly half the h value of the Small samples. The graph shows that the rate of increasing *h* decreases with Reynolds number for all the samples.

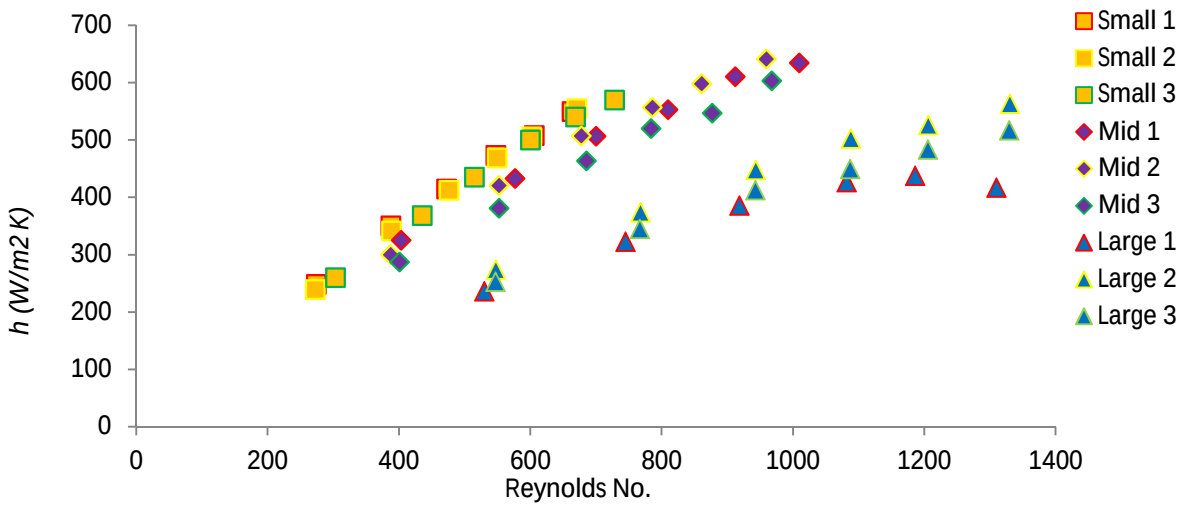

Fig. 9-10, Heat transfer coefficient of the metal foams against Reynolds number

The *h* is calculated for the wire mesh and ball bearing samples plotted with Reynolds number in Fig. 9.11a and 9.11b. It can be seen that Reynolds number was much smaller for the wire mesh than the ball bearing sample for the same air cross sectional mean velocity. The reason for this is the hydraulic diameter of the wire diameter was considerably smaller than the ball bearing. By assuming that each *h* point was measured at the same flow rate, figure 9.9a and 9.9b show that the wire mesh *h* was nearly three times higher than the ball bearing.

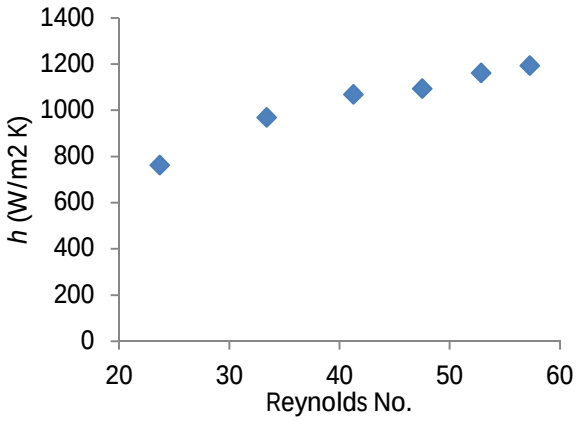

Fig. 9.11a, Heat transfer coefficient of the wire mesh sample against Reynolds number

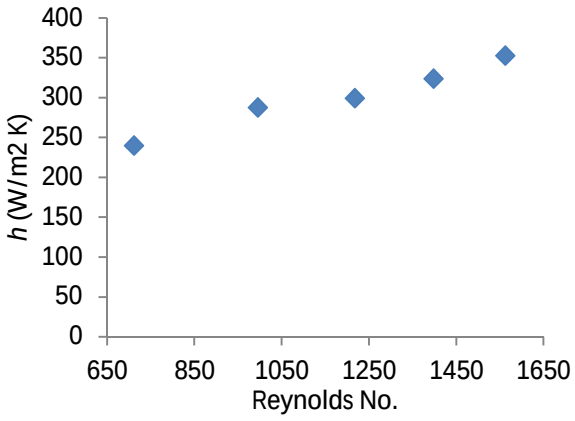

Fig. 9.11a, Heat transfer coefficient of the ball bearing sample against Reynolds number

Shown in Fig. 9.12 is the thermal performance of the wire mesh and ball bearing samples plotted with the correlation result obtained by Kays and London [100]. For doing this comparison, Stanton number (Eq. 9.8) was calculated for each sample and plotted with Reynolds number.

$$St = \frac{hA_{cs}\varepsilon}{\dot{m}C_p} \qquad \text{Eq. 9.8}$$

The graph shows a good agreement for the wire mesh sample. However, the ball bearing results was lower than their result. One of the possible reasons could be the error in calculating specific surface area. The specific surface area was calculated based on all surface area of each steel ball. However, the area between the ball bearings interface cannot transfer heat from the air to the ball bearing. Therefore the effective surface area was lower than the calculated area. Consequently, the estimated h was higher than the actual value and therefore *St* was lower than the Kays and London results. This is not the case for the wire mesh sample since the method used for calculating the specific surface area was the same for Kays and London. Therefore the wire mesh result was closer to their results.

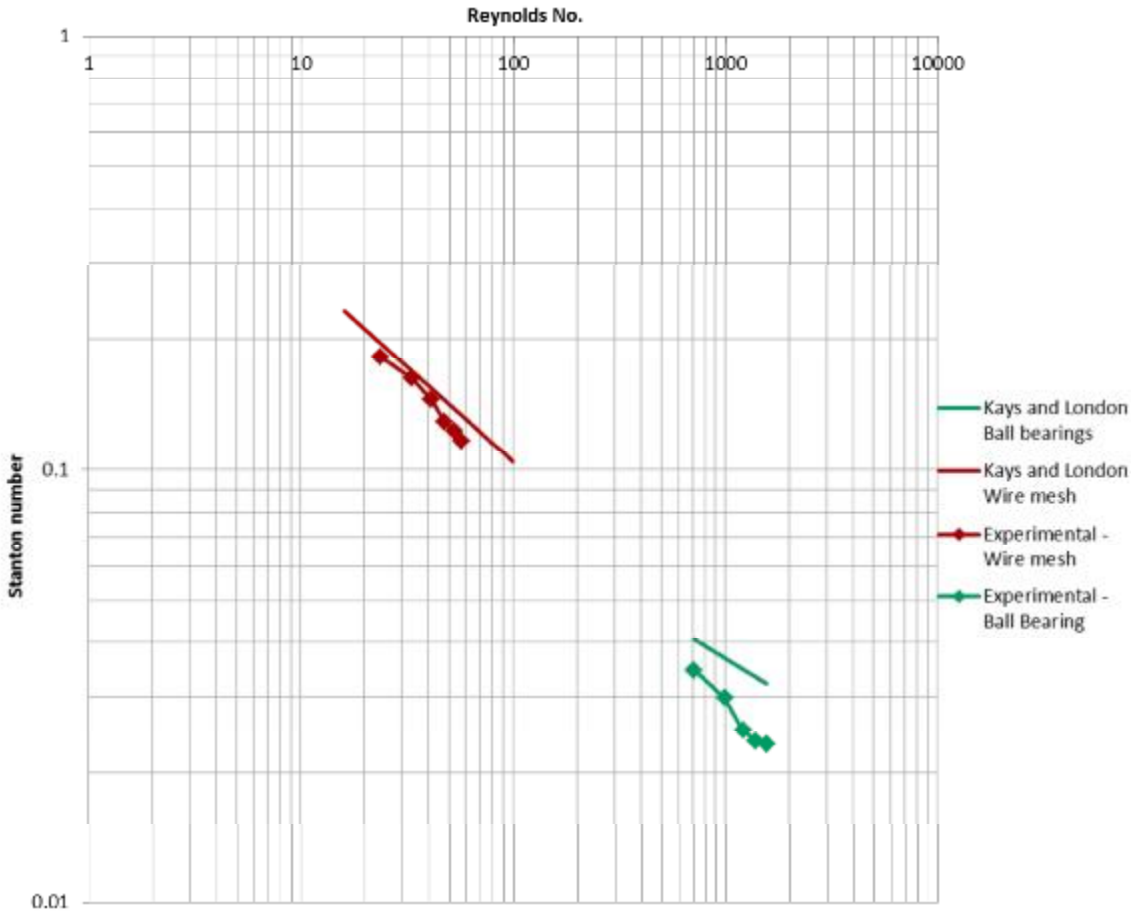

Fig. 9.12, Heat transfer characteristics of the wire mesh and ball bearing sample plotted with the correlation of Kays and London experimental data.

The thermal performance and pressure drop of the samples have been studied but for overall performance evaluation, the combination of both results should be considered. Performance of a regenerator depends on its capability of storing heat and the mechanical power expenditure to pass the fluid through it. Since regenerators mainly operating with low-density fluids such as air, the friction power expenditure is relatively high compared to the heat transfer rate. If we assume that in most thermal power systems the efficiency is around 25 to 35% this means mechanical energy is worth three to four times that of thermal energy. Therefore, it is easy to expend same amount of energy to overcome pressure drop as to store heat [100].

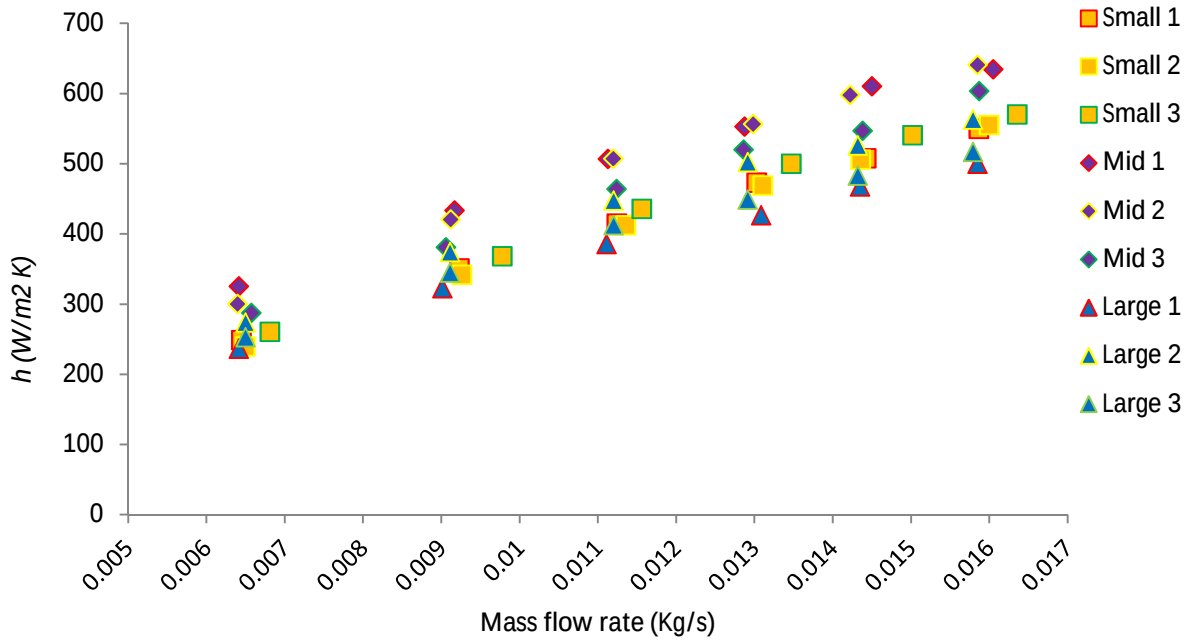

Fig. 10.1, Heat transfer coefficient of the metal foams against Reynolds number

Pressure data measurements showed that the Small samples had the highest pressure drop and they also had the highest *NTU*. Hence, reducing the pore size increases heat transfer but this also increases pressure drop. Therefore, sample's pore size has conflicting effects on pressure drop and *NTU*.

As it can be seen from Eq. 10.1 that transferred thermal energy from air to a regenerator depends on the heat transfer coefficient (h) and heat transfer area (A_{hs}). Therefore samples

with high *h* and surface area would have the highest ability to absorb heat from air flow (assuming that samples made from similar material). Shown in Fig. 10.1 is the *h* for the metal foams plotted against the air mass flow rate. The graph shows that Mid samples had the highest *h*. However, it should be remembered that Small samples on average have 30% more surface area than the Mid samples.

$$Q = hA_{hs}\Delta T \qquad \text{Eq. 10.1}$$

In this study metal foam samples had relatively similar length but different specific surface area. Therefore it was difficult to compare the overall performance of the sample. To compare two samples, first the total amount of thermal energy (*Q* in Eq. 10.1) which can be absorbed by one of the sample was calculated by knowing *h* (from the experimental result), A_{hs} (Table 9.2) and ΔT (for a single degree difference). Then the heat transfer surface area of the second sample which could store the same amount of energy was calculated by knowing the specific transfer surface area. Once the required heat transfer surface area was calculated the length was calculated to store the same amount of thermal energy of the first sample. By knowing the required length, sample pressure drop was calculated by assuming that pressure drop increase linearly with the sample length. Now the sample performance could be compared with the first sample in terms of pressure drop. The author is aware that applying this method for each individual sample may increase the risk of wrong estimating one particular samples performance due to unknown internal structure or possibly defect. However, it could provide a preliminary information regarding samples overall performance.

It can be seen from Fig. 10.1, at 0.016 (Kg/s) flow rate, *h* for sample Mid 1 and Small 3 was 661 and 571 ($W/m^2 K$) respectively. Multiplying this value to samples surface area (assuming the temperature difference (ΔT) is one degree) Eq. 10.1 yields %32 more thermal energy for Small 3 than Mid 2. Therefore, in order to store the same amount of thermal energy with Mid 1 sample it should be 32% longer than Mid 1 or in other word it should have 32% more surface area. Since the flow inside the foams is laminar, it can be assumed that the pressure drop increases linearly with samples length. Therefore, this imaginary longer sample would have 38% more pressure drop than Mid 2 sample. However, the imaginary sample would

have 45% less pressure drop than Small 3 and 30% less than Small 2. As a result, the imaginary sample would outperform Small 3 and 2 in terms of pressure drop and thermal performance. Similar analogy shows that Large 2 should be 89% longer to have a similar thermal performance to Small 3. This imaginary Large 2 sample would have 50% less pressure drop compared to Small 3 and 35% less compared to Small 2. This means that the imaginary Large 2 sample would perform better than the imaginary Mid 2. Using the same analogy, the wire mesh sample can absorbed the same amount of thermal energy as Small 3 but at 87% shorter length or 74% less pressure drop than Small 3 sample and 66% less compared to Small 2.

The above analogy shows that for metal foams, Mid 2 and Large 2 had better performance than Small 3. Large 2 performed slightly better than Mid 2. It also shows that by increasing the Large 2 length a similar thermal performance to Small 3 could be achieved with lower pressure drop. However, having longer length may not be an issue for some application like stationary heat recovery unit but it is not desirable for some application such as regenerator in Stirling engines. In Stirling engine any gas which does not generate work considered as a dead volume. Increasing sample's length would increase its dead volume (the air inside the regenerator which does not involve generating work). For instance the imaginary Large 2 have 89% more dead volume than Small 3. Therefore the design of a regenerator involves a consideration of all these factors.

In addition to the dead volume, regenerator effectiveness is the other important factor in regenerator design. Since in Stirling engine the working fluid moves across the regenerator at frequency as high as 50 Hz, it is important to select the right wire thickness or in the case of metal foam thickness of the material between pores. For instance, in Fig. 10.2 shows the cross section area of the connecting part between pores in metal foams with three different pore size. The orange arrows represent the heat penetration into the foam material. If the pore size is too large (the 3rd image from left) heat does not penetrate completely into the foam material within the blow time and the centre part will be unusable. Since the pores are too small, heat penetrates into the foam and saturates the foam before the blow time expires. In this case, part of the heat cannot be absorbed by the foam and effective heat storage would be insufficient. Therefore larger sample is needed to provide enough heat

storage capacity. However, this would also increase pressure loss through the sample. In order to investigate this effect, samples should be tested under oscillatory condition. Optimum pore size of the samples could be identified by testing samples under oscillatory flow. A similar analogy was presented by Miyabe et al. [72]for wire mesh screens.

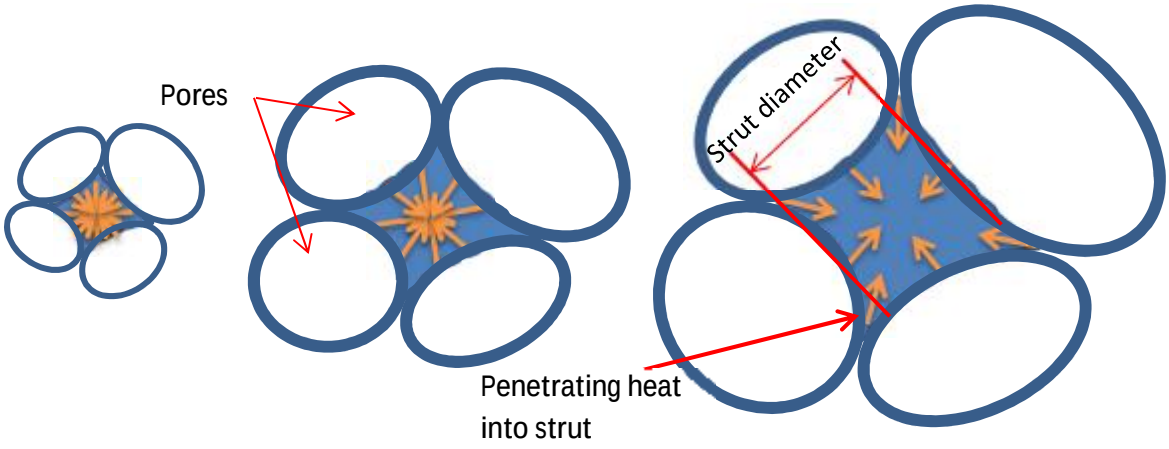

Fig. 10.2, Strut diameters of the different pore size samples

As it was discussed earlier in this chapter, the wire mesh sample had exceptionally good performance compared to the metal foams. There are several factors that makes wire mesh performs better than then the metal foams. One of the main factors is the sample material. Stainless steel has one of the highest volumetric heat capacity (material density times the specific heat capacity) among the conventional metals. Although aluminium has higher specific heat capacity than stainless steel, it has relatively lower density. Stainless steel has nearly 60% higher volumetric heat capacity than aluminium and therefore samples made from stainless steel would have 60% more thermal capacity than aluminium.

One of the issues with metal foam samples was their high longitudinal thermal conductivity. As it was shown in the previous chapter, having higher thermal conductivity reduces samples *NTU* and therefore reduces thermal performance. This is due to heat transfer through the samples via conduction which reduces the temperature difference between the air and the sample. As a result, reduces the samples effectiveness. In contrast, heat in samples with high thermal conductivity transfers from the gas to the sample and not through the sample itself. Once the gas thermal energy transfers to the sample its temperature drops to near the sample initial temperature. Therefore it passes the sample without increasing the temperature for the rest of the sample. As a result, rest of the

sample would have higher temperature difference between the gas and the sample which means that part of the sample would have higher effectiveness. For instance, in wire mesh heat transfers from the gas to the first few layers of the sample and gas temperature drops to the sample initial temperature. After blowing more high temperature gas, the first few layers are saturated with heat and they would have low effectiveness. However, the rest of the layers are still in initial temperature with high effectiveness. If this sample had high thermal conductivity, the heat would transfer through the sample and increases the entire sample temperature and reduces the sample overall effectiveness. This is particularly important in application such as Stirling engine which the working gas shuttles between two cylinders at high frequency. In addition, low thermal conductivity and small contact area with the wall leads to negligible heat loss to the wall which improves thermal performance of the wire mesh sample.

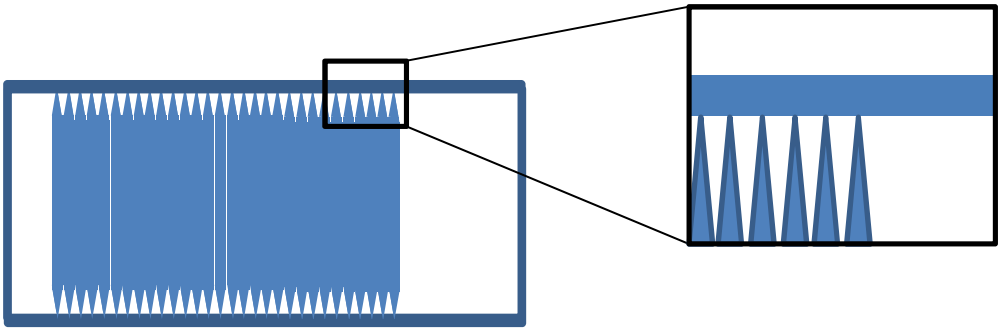

Fig. 10.3, A schematic view of sliced sample with tapered edges inside a pipe.

Thermal performance of aluminium metal foams could be improved by reducing longitudinal thermal conductivity and minimising heat loss to the wall. Samples longitudinal thermal conductivity could be reduced by slicing the sample into thin disks and alternately packed them with low conductivity stainless steel spacer. Doing this could potentially reduce the longitudinal thermal conductivity of the metal foam samples and therefore improve their thermal performance. Heat transfer to the wall could also be reduced by reducing the contact area between the sample and the wall. After slicing the foam, the edge of the disks can be tapered to reduce the contact surface area and therefore reduces the heat transfer between the wall and the sample. Shown in Fig. 10.3 is a schematic view of the sliced sample with tapered edges.

Chapter 11 - Conclusions and future work

11.1. Concluding remarks

The current study was covered several topics to help understand heat transfer and fluid mechanics in metal foams manufactured by the Replication method. The results of this study could help to develop high performance and low cost regenerators. The following list is a brief summary of the achievements and the work remains to be done.

11.1.1. Sample manufacturing:

1- Three different size salt particles (1-1.1 mm, 1.4-1.7 mm and 2.0-2.36 mm) were used to make aluminium foam with the Replication process.
2- The infiltrations method for replication process was investigated and two new methods, gas-only and mechanical infiltration, were introduced. It was found that samples manufactured by the gas-only method had better quality and process was more repeatable than the standard vacuum-gas and mechanical infiltration methods.
3- A total of eight samples (1.4-1.7 mm pore size) were manufactured under various infiltration pressures to study the effect of infiltration pressure on samples pressure drop.
4- The optimum infiltration pressure for gas-only method was studied and the optimum infiltration pressure for three pore sizes, 1-1.1 mm, 1.4-1.7 mm and 2.0-2.36 mm, were identified.
5- A total of nine metal foams (three of each pore size) were manufactured by the gas-only method for thermal and pressure test. The manufactured samples had on average 63% porosity.
6- A packed bed of 10000 2mm ball bearing and a packed bed of 100 layers of wire mesh (No. 200) were built for comparing with metal foams samples.

11.1.2. Steady state pressure drop:

1- A test rig was built and the samples pressure drop was tested from 1 to 6.5 m/s.
2- The extended Darcy-Forchheimer equation was used to calculate the samples permeability and form drag coefficient.

3- The results showed that samples' permeability increased by increasing the pore size and the form drag reduced by increasing the pore size.
4- The Wire mesh sample had the highest normalised pressure drop following the Ball bearing sample.
5- The samples made under different infiltration pressure were tested and the results showed that the samples made under higher infiltration pressure than 4.5 bar had higher pressure drop and the samples made at lower infiltration pressure either partly infiltrated or had defects.

11.1.3. Oscillatory pressure drop:

1- A test rig was built and samples pressure drop were measured under oscillatory flow from frequency 1 to 19 Hz.
2- The results showed that the profile of the pressure drop for frequencies lower than 14 Hz were nearly sinusoidal due to the reciprocating motion of the piston but at higher frequencies the pressure drop profile became unsymmetrical notably where the piston accelerated (before 90^o). Similar trends were observed for the second half of the cycle between 180^o and 270^o.
3- The maximum pressure drop occurred at 90^o and 270^o which was where the air velocity was at maximum. However, as the frequency increased the maximum pressure drop was shifted by a few degrees. This phase shift also increased by increasing the pressure drop.
4- Samples had higher pressure drop under oscillatory flow than steady state flow except for the Small samples which had higher pressure drop at steady state flow.
5- Darcy-Forchheimer equation was applied to the oscillatory pressure data and the data showed that the reduced pressure drop only followed Darcy-Forchheimer regime for flow velocity higher than 0.5 m/s
6- Flow velocity was measured at the centre of the connecting pipe (between the compressor and the test section) by a hot-wire anemometer. The results showed that the air velocity fluctuated during the acceleration and deceleration period and behave "like a turbulent flow".

11.1.4. Heat transfer measurement:

1- A single-blow test rig was designed and manufactured to measure thermal performance of the samples. Samples were tested at Reynolds number from 250 to 1350. Reynolds number was measured based on foams pore diameter.

2- Several types of the single-blow model method (depending on working fluid properties and regenerator types) were presented and analysed. The extended Schumann-Hausen model was implemented for predicting the outlet air temperature.

3- The mathematical model was numerically solved by an explicit finite difference method and the results were further improved by an implicit method (The Crank-Nicolson) for better accuracy. The accuracy of the modelling results was validated by the Kohlmayer's (Eq. 6.19) analytical solution.

4- The effect of changing *NTU*, NTU_w, R_{tc} and inlet air response on the maximum gradient was investigated and the results were plotted for visualising the effect of variables on *NTU.*

5- Four different matching techniques were evaluated and the maximum gradient method and direct curve matching were selected for match the experimental and predicted curves.

6- A new technique was introduced to match the experimental and predicted data with direct curve matching when the effective thermal conductivity, *NTU* and NTU_w were unknown.

7- Effective thermal conductivity of the foams was estimated for the first time with the direct matching technique and the results had good agreement with the data estimated based on sintered metal and high porosity metal foam correlation.

8- The metal foams results showed that *NTU* increased by decreasing the pore size and the results were similar for each pore size.

9- Samples heat transfer coefficients were calculated and plotted against Reynolds number. The results showed that based on mass flow rate Mid samples had the highest *h*, however the differences between the metal foams were insignificant.

10- The Ball bearing and Wire mesh samples results were compared with Kays and London results and good agreement particularly with the Wire mesh results was achieved.

11.2. Future work

During the course of this study several opportunity were discovered which could improve the results of this research. However, it was not possible to implement these ideas into this study mainly due to budget and time limitation. The following list is the author recommended future work:

11.2.1. Improving thermometry system

For this study K-type thermocouples were used to measure the temperature across the sample. The primary reason for selecting K-type thermocouple was the cost of the fast response thermometry system. The current system offered an acceptable level of accuracy but for better accuracy K-type thermocouples would not recommended. Instead, a cold-wire anemometry system would be an ideal thermometry system for this application due to high frequency and accuracy.

11.2.2. Measuring surface area with X-ray 3D CT-scan

As it was discussed earlier, accuracy of the heat transfer coefficient highly depends on accuracy of the specific surface area. Due to random and complex structure of the metal foam it is difficult to accurately estimate the specific surface area through a mathematical model. Therefore direct measurement of the specific surface area is more desirable. One of possible way of measuring is by X-ray tomography. A similar work has been done by Bock and Jacobi [101] on high porosity metal foams which can be adopted for the current metal foams. The results of X-ray tomography would be beneficial not only for measuring the surface area but also for detecting defects inside the foams. In addition, the digital geometry of the foam can be generated by this method and could be used in CFD study.

11.2.3. CFD modelling and analysis

The geometry created by the X-ray tomography can be used to model the foams and run CFD analysis to optimise the foams performance. Current experimental data could also be used to validate the model.

11.2.4. Writing an algorithm to match curves

As it was discussed in chapter 8, the predicted curve was fitted by guessing samples *NTU*, NTU_w and λ. This was a tedious method and will not be practical for large number of samples. Therefore, writing an algorithm and a computer code to do this automatically would be beneficial.

11.2.5. Measuring effective thermal conductivity

Knowing samples effective thermal conductivity is important for accurately predicting outlet temperature. Knowing this value is essential for the maximum gradient method and without this value using this method would yield a large error. Therefore, direct measurement of k_{eff} is recommended for future study. It would be important to measure this value and validate the results estimated in this study by matching the entire curve.

11.2.6. Measuring thermal performance under oscillatory flow

Samples optimum pore size and effectiveness of the regenerators could be evaluated under oscillatory condition. In addition, comparison between the steady and oscillatory flow results would be beneficial for investigating the physics of heat transfer under oscillatory flow.

11.2.7. Manufacture more samples with an improved packing mechanism

For this study three samples were manufactured with randomly packing the salts particles. However, the pressure drop results showed that the samples with similar pore size were not identical. As it was discussed in chapter 3, the reason of the discrepancy in pressure data could be the randomness of the salts packing. Therefore, more samples needed to be manufactured to statistically identifying samples deviation. Another possible action would

be improving repeatability of the process by improving the packing mechanism. This could be done by vibrating the salts particles pack to ensure consistent in packing density.

11.2.8. Manufacturing foams with different pore shape

As it was discussed in chapter 3, packing density depends on several factors such as shape, size and friction factor between the particles. Metal foam density depends on the preform packing density and the infiltration pressure. Therefore, changing the salt particles shape may change the foams density and pressure drop performance. Since the foams made for this study were made with crushed salt particles, it would be interesting to see the effect of particles shape on samples performance.

11.2.9. Making stainless steel foam

Stainless steel is suitable for using as a regenerator material since it has high volumetric heat capacity. Making foam from stainless steel with replicating method is a challenging process due to higher melting point of stainless steel. Therefore, a different preform material should be used to have a higher melting point than stainless steel and can be dissolved without reacting with the solvent.

11.2.10. Slicing foams to improve thermal performance

Following the discussion on chapter 10, reducing the longitudinal effective thermal conductivity could improve thermal performance of the samples without increasing the pressure drop. Slicing the samples into thin disks and alternately packing them with low conductivity stainless steel spacer could reduce k_{eff}. However, it is not clear the extent of this improvement. Therefore, testing samples before and after this process could reveal the effect of reducing samples thermal conductivity.

References

[1] Barari, F., Luna, E. M. E., Goodall, R., and Woolley, R., 2013, “Metal foam regenerators; heat transfer and storage in porous metals,” J. Mater. Res., **28**(17), pp. 2474–2482.

[2] Chen, P.-H., Chang, Z.-C., and Huang, B.-J., 1996, “Effect of oversize in wire-screen matrix to the matrix-holding tube on regenerator thermal performance,” Cryogenics (Guildf)., **36**(5), pp. 365–372.

[3] Jin, L., and Leong, K. C., 2006, “Heat Transfer Performance of Metal Foam Heat Sinks Subjected to Oscillating Flow,” IEEE Trans. Components Packag. Technol., **29**(4), pp. 856–863.

[4] Bhattacharya, A., Calmidi, V. V, and Mahajan, R. L., 2002, “Thermophysical properties of high porosity metal foams,” Int. J. Heat Mass Transf., **45**(June 2001), pp. 1017–1031.

[5] Du, Y. P., Qu, Z. G., Zhao, C. Y., and Tao, W. Q., 2010, “Numerical study of conjugated heat transfer in metal foam filled double-pipe,” Int. J. Heat Mass Transf., **53**(21-22), pp. 4899–4907.

[6] Dukhan, N., and Chen, K.-C., 2007, “Heat transfer measurements in metal foam subjected to constant heat flux,” Exp. Therm. Fluid Sci., **32**(2), pp. 624–631.

[7] Fuller, a. J., Kim, T., Hodson, H. P., and Lu, T. J., 2005, “Measurement and interpretation of the heat transfer coefficients of metal foams,” Proc. Inst. Mech. Eng. Part C J. Mech. Eng. Sci., **219**(2), pp. 183–191.

[8] Ko, K.-H., and Anand, N. K., 2003, “Use of porous baffles to enhance heat transfer in a rectangular channel,” Int. J. Heat Mass Transf., **46**(22), pp. 4191–4199.

[9] Zhao, C. Y., 2012, “Review on thermal transport in high porosity cellular metal foams with open cells,” Int. J. Heat Mass Transf., **55**(13-14), pp. 3618–3632.

[10] Schumann, T. E. W., 1929, “Heat transfer: A liquid flowing through a porous prism,” J. Franklin Inst., **208**(3), pp. 405–416.

[11] Hausen, H., 1983, Heat transfer in counterflow, parallel flow and cross flow, McGraw Hill, New York; London.

[12] Furnas, C. C., 1931, Heat Transfer From a Gas Stream to a Bed of Broken Solids, Washington.

[13] Locke, G. L., 1950, Heat transfer and flow friction characteristics of porous solids, Stanford, California.

[14] Coppage, J. E., and London, A. L., 1956, “Heat transfer and flow friction characteristics of porous media,” Chem. Eng. Prog., **52**(2), pp. 57–63.

[15] Amiri, a., and Vafai, K., 1994, “Analysis of dispersion effects and non-thermal equilibrium, non-Darcian, variable porosity incompressible flow through porous media,” Int. J. Heat Mass Transf., **37**(6), pp. 939–954.

[16] Tong, L. S., and London, A. L., 1957, “Heat-transfer and flow-friction characteristics of woven-screen and crossed-rod matrixes,” Trans. ASME, **79**, pp. 1558–1570.

[17] Chou, F. C., Chung, P. Y., and Cheng, C. J., 1991, “Effects of Stagnant and Dispersion Conductivities on Non-Darcian Forced Convection in Square Packed-Sphere Channels,” Can. J. Chem. Eng., **69**(Case I), pp. 1401–1407.

[18] Chang, C., Hung, S., Ding, P., and Chen, H., 1999, “Experimental evaluation of thermal performance of Giford- McMahon regenerator using an improved single!blow model with radial conduction,” Int. J. Heat Mass Transf., **42**, pp. 405–413.

[19] Shuangtao, C., Yu, H., Hongli, Z., and Lan, X., 2009, “A numerical model of thermal analysis for woven wire screen matrix heat exchanger,” Cryogenics (Guildf)., **49**(9), pp. 482–489.

[20] Tanaka, M., Yamashita, I., and Chisaka, F., 1990, “Flow and Heat Transfer Characteristics of the Stirling Engine Regenerator in an Oscillating Flow,” JSME Int. J., **33**(2), pp. 283–289.

[21] Fu, X., Viskanta, R., and Gore, J. P., 1998, “Measurement and correlation of volumetric heat transfer coeffients of cellular ceramics,” Exp. Therm. Fluid Sci., **17**, pp. 285–293.

[22] Younis, L. B., and Viskanta, R., 1993, “Experimental determination of the volumetric heat transfer coefficient between stream of air and ceramic foam,” Int. J. Heat Mass Transf., **36**(6), pp. 1425–1434.

[23] Rapley, C. W., and Webb, a. I. C., 1983, “Heat transfer performance of ceramic regenerator matrices with sine-duct shaped passages,” Int. J. Heat Mass Transf., **26**(6), pp. 805–814.

[24] Leong, K. C., and Jin, L. W., 2006, “Effect of oscillatory frequency on heat transfer in metal foam heat sinks of various pore densities,” Int. J. Heat Mass Transf., **49**(3-4), pp. 671–681.

[25] Hwang, J.-J., Hwang, G.-J., Yeh, R.-H., and Chao, C.-H., 2002, “Measurement of Interstitial Convective Heat Transfer and Frictional Drag for Flow Across Metal Foams,” J. Heat Transfer, **124**(1), p. 120.

[26] Boomsma, K., Poulikakos, D., and Zwick, F., 2003, “Metal foams as compact high performance heat exchangers,” Mech. Mater., **35**(12), pp. 1161–1176.

[27] Conde, Y., Despois, J.-F., Goodall, R., Marmottant, a., Salvo, L., San Marchi, C., and Mortensen, a., 2006, “Replication Processing of Highly Porous Materials,” Adv. Eng. Mater., **8**(9), pp. 795–803.

[28] Goodall, R., Despois, J.-F., Marmottant, A., Salvo, L., and Mortensen, A., 2006, “The effect of preform processing on replicated aluminium foam structure and mechanical properties,” Scr. Mater., **54**(12), pp. 2069–2073.

[29] Banhart, J., Ashby, M. F., and Fleck, N. A., 1999, “Properties and applications of cast aluminium sponges,” Met. Foam. Porous Met. Struct., pp. 159–162.

[30] Fabrizio, Q., Boschetto, A., Rovatti, L., and Santo, L., 2011, “Replication casting of open-cell AlSi7Mg0.3 foams,” Mater. Lett., **65**(17-18), pp. 2558–2561.

[31] Jamshidi-Alashti, R., and Roudini, G., 2012, “Producing replicated open-cell aluminum foams by a novel method of melt squeezing procedure,” Mater. Lett., **76**, pp. 233–236.

[32] Ebbing, D. D., and Gammon, S. D., 2009, General Chemistry, Houghton Mifflin Company, USA.

[33] Goodall, R., Despois, J.-F., and Mortensen, a., 2006, “Sintering of NaCl powder: Mechanisms and first stage kinetics,” J. Eur. Ceram. Soc., **26**(16), pp. 3487–3497.

[34] Goodall, R., Marmottant, A., Salvo, L., and Mortensen, A., 2007, “Spherical pore replicated microcellular aluminium: Processing and influence on properties,” Mater. Sci. Eng. A, **465**(1-2), pp. 124–135.

[35] Ergun, S., 1952, “Fluid flow through packed columns,” Chem. Eng. Prog., **48**(2), pp. 89–94.

[36] Reyes, G. Y. Z., 2012, “Aluminium Foams For Heat Transfer Applications,” The University of Sheffield.

[37] Abdulla, T., 2013, “The Effect of Pulsed Bipolar Plasma Electrolytic Oxidation Coatings on the Mechanical Properties of Open Cell Aluminium Foams,” The University of Sheffield.

[38] Goodall, R., and Mortensen, a., 2007, “Microcellular Aluminium? – Child’s Play!,” Adv. Eng. Mater., **9**(11), pp. 951–954.

[39] Despois, J. F., Marmottant, a., Salvo, L., and Mortensen, a., 2007, “Influence of the infiltration pressure on the structure and properties of replicated aluminium foams,” Mater. Sci. Eng. A, **462**(1-2), pp. 68–75.

[40] Atmakidis, T., and Kenig, E. Y., 2009, “CFD-based analysis of the wall effect on the pressure drop in packed beds with moderate tube/particle diameter ratios in the laminar flow regime,” Chem. Eng. J., **155**(1-2), pp. 404–410.

[41] Darcy, H., 1856, Les Fontaines Publiques de la Ville de Dijon, Paris.

[42] Boomsma, K., and Poulikakos, D., 2002, “The Effects of Compression and Pore Size Variations on the Liquid Flow Characteristics in Metal Foams,” J. Fluids Eng., **124**(1), p. 263.

[43] Dupuit, A. J. E. J., 1863, Etudes Theoriques et Pratique sur le Mouvement des Eaux, Paris.

[44] Boomsma, K., and Poulikakos, D., 2002, “The Effects of Compression and Pore Size Variations on the Liquid Flow Characteristics in Metal,” J. Fluids Eng., **124**(March), pp. 263–272.

[45] Dukhan, N., and Patel, P., 2008, “Equivalent particle diameter and length scale for pressure drop in porous metals,” Exp. Therm. Fluid Sci., **32**(5), pp. 1059–1067.

[46] Dybbs, A., and Edwards, R., 1975, “‘Department of Fluid, Thermal, and Aerospace Report,’” presented at Workshop on Heat and Mass Transfer in Porous Media, Springfield.

[47] Lage, J. L., Antohe, B. V., and Nield, D. A., 1997, “Two Types of Nonlinear Pressure-Drop Versus Flow-Rate Relation Observed for Saturated Porous Media,” ASME J. Fluid Eng., **119**, pp. 700–706.

[48] Bs En ISO 5167-1, 1997, Measurement of fluid flow by means of pressure differential devices.

[49] Zhao, T. S., and Cheng, P., 1996, “Oscillatory pressure drops through a woven-screen packed column subjected to a cyclic flow,” Cryogenics (Guildf)., **36**(5), pp. 333–341.

[50] Leong, K. C., and Jin, L. W., 2006, “Characteristics of oscillating flow through a channel filled with open-cell metal foam,” Int. J. Heat Fluid Flow, **27**(1), pp. 144–153.

[51] Jin, L. W., and Leong, K. C., 2007, “Pressure drop and friction factor of steady and oscillating flows in open-cell porous media,” Transp. Porous Media, **72**(1), pp. 37–52.

[52] Richardson, B. A., and Tyler, E., 1929, “The transverse velocity gradient near the mouths of pipes in which an alternating or continuous flow of air is established,” Proc. Phys. Soc., **42**, pp. 1–15.

[53] Zhao, T. S., and Cheng, P., 1998, “A Numerical Study of Laminar Reciprocating Flow in a Pipe of Finite Length,” Appl. Sci. Res., **59**, pp. 11–25.

[54] Hino, M., Sawamoto, M., and Takasu, S., 1976, “Experiments on transition to turbulence in an oscillatory pipe flow,” Fluid Mech., **75**, pp. 193–207.

[55] Isshiki, S., Sakano, A., Ushiyama, I., Isshiki, N., and Univ, N., 1996, “Measurement on Nusselt number of regenerator wire meshes by cylindrical probe,” Energy Conversion Engineering Conference, 1996. Proceedings of the 31st Intersociety, pp. 7–12.

[56] Zhao, T. S., and Cheng, P., 1996, “Experimental studies on the onset of turbulence and frictional losses in an oscillatory turbulent pipe flow,” Int. J. Heat Fluid Flow, **17**, pp. 356–362.

[57] Zhao, T. S., and Chen, P., 1996, “The friction coefficient of a fully developed laminar reciprocating flow in a circular pipe,” Int. J. Heat Fluid Flow, **17**, pp. 167–172.

[58] Ju, Y., Jiang, Y., and Zhou, Y., 1998, “Experimental study of the oscillating flow characteristics for a regenerator in a pulse tube cryocooler,” Cryogenics (Guildf)., **38**(6), pp. 649–656.

[59] Gedeon, D., and Wood, J. G., 1996, Oscillating-Flow Regenerator Test Rig : Hardware and Theory With Derived Correlations for Screens and Felts.

[60] Hsu, C. T., Fu, H. L., and Cheng, P., 1999, “On pressure-velocity correlation of steady and oscillating flow in regenerators made of wire screens,” J. Fluids Eng. ASME, **121**(1), pp. 52–56.

[61] Bruun, H. H., 1995, Hot-Wire Anemometry Principle and Signal Analysis, Oxford University Press, New York.

[62] Beasley, F. I., 2001, Theory and Design for Mechanical Measurements, John Wiley & Sons, Inc.

[63] King, L. V., 1914, “On the Convection of Heat from Small Cylinders in a Stream of Fluid : Determination of the Convection Constants of Small Platinum Wires , with Applications to Hot-Wire Anemometry,” Proc. R. Soc., **90**(622), pp. 563–570.

[64] Jorgensen, F. E., 2002, How to measure turbulence with hot-wire anemometers - A practical guide, Dantec Dynamics, Skovlunde, Denmark.

[65] O’Dea, J., and Fleming, P., 1995, “The conflicting conditions for precision and sensitivity in a Wheatstone bridge,” Reg. Tech. Coll., **30**, pp. 389–390.

[66] George, W. K., Beuther, P. D., and Shabbir, A., 1989, “Polynomial Calibrations for Hot Wires in Thermally Varying Flows,” Exp. Therm. Fluid Sci., **2**, pp. 230–235.

[67] Pamuk, M. T., and Özdemir, M., 2012, “Heat transfer in porous media of steel balls under oscillating flow,” Exp. Therm. Fluid Sci., **42**, pp. 79–92.

[68] Wakeland, R. S., and Keolian, R. M., 2003, “Measurements of Resistance of Individual Square-Mesh Screens to Oscillating Flow at Low and Intermediate Reynolds Numbers,” J. Fluids Eng., **125**(5), p. 851.

[69] Dukhan, N., and Minjeur, C. a., 2010, “A two-permeability approach for assessing flow properties in metal foam,” J. Porous Mater., **18**(4), pp. 417–424.

[70] Choi, S., Nam, K., and Jeong, S., 2004, “Investigation on the pressure drop characteristics of cryocooler regenerators under oscillating low and pulsating pressure conditions,” Cryogenics (Guildf)., **44**(3), pp. 203–310.

[71] Ju, Y., and Shen, Q., 2009, “Comparative study of oscillating flow characteristics of cryocooler regenerator at low temperatures,” Front. Energy Power Eng. China, **3**(1), pp. 80–84.

[72] Miyabe, H., Takahashi, S., and Hamaguchi, K., 1982, “An approch to the design of Stirling engine regenerator matrix using pack of wire gauzes,” 17th IECEC, pp. 1839–1844.

[73] Ju, Y., and Shen, Q., 2009, “Comparative study of oscillating flow characteristics of cryocooler regenerator at low temperatures,” Front. Energy Power Eng. China, **3**(1), pp. 80–84.

[74] Chen, P.-H., and Chang, Z.-C., 1997, “Measurements of thermal performance of cryocooler regenerators using an improved single-blow method,” Int. J. Heat Mass Transf., **40**(10), pp. 2341–2349.

[75] Loehrke, R. I., 1990, “Evaluating the results of the single-blow transient heat exchanger test,” Exp. Therm. Fluid Sci., **3**(6), pp. 574–580.

[76] Schmidt, F. W., and Willmott, A. J., 1981, Thermal Energy Storage and Regeneration, Mc Graw Hill.

[77] Kohlmayr, G. F., 1966, “Exact maximum slopes for transient testing heat-transfer testing,” Int. J. Heat Mass Transf., **9**.

[78] Pucci, P. F., Howard, C. P., and Piersall, C. H., 1967, “The single-blow transient testing technique for compact heat exchanger surfaces,” ASME J. Eng. Power, **89**(1), pp. 29–40.

[79] Cai, Z. H., Li, M. L., Wu, Y. W., and Ren, H. S., 1984, “A modified selected point matching technique for testing compact heat exchanger surfaces,” Int. J. Heat Mass Transf., **27**(7), pp. 971–978.

[80] Liang, C. Y., and Yang, W. J., 1975, “Modified single-blow technique for performance evaluation on heat transfer surfaces,” ASME J. Heat Transf., **97**, pp. 16–21.

[81] Mullisen, R. S., and Loehrke, I. R., 1986, “A transient heat exchanger evaluation test for arbitrary fluid inlet temperature variation and longitudinal core conduction,” ASME J. Heat Transf., **108**, pp. 370–376.

[82] Sonntag, R. E., Borgnakke, C., and Van Wyle, G. J., 1998, Fundamental of Thermodynamics, John Wiley & Sons, Inc., New York.

[83] Hoffman, J. D., 2001, Numerical Methods for Engineers and Scientists, Marcel Dekker, New York.

[84] Chapra, S. C., and Canale, R. P., 2006, Numerical Methods for Engineers, McGraw Hill, Singapore.

[85] Carnahan, B., Luther, H. A., and Wilkes, J. O., 1969, Applied Numerical Methods, Wiley, New York.

[86] Chen, P.-H., and Chang, Z.-C., 1996, “An improved model for the single-blow measurement including the non-adiabatic side wall effect,” Int. Commun. Heat Mass Transf., **23**(1), pp. 55–68.

[87] Darabi, F., 1982, “Heat and Momentum Transfer in Packed Beds,” University of Leeds.

[88] Baclic, B. S., Gvozdenac, D. D., Sekulic, D. P., and Becic, E. J., 1986, “Laminar Heat Transfer Characteristics of a Plate-Louver Fin Surface Obtained by The Differential Fluid,” ASME Adv. Heat Exch. Des., **66**, pp. 13–21.

[89] Baclic, B. S., Gvozdenac, D. D., and Vadlja, D., 1986, “Performance Identification of the Apparatus for Testing Compact Heat Exchanger Surfaces,” ASME Adv. Heat Exch. Des., **66**, pp. 13–20.

[90] Heggs, P. J., and Burns, D., 1988, “Single-Blow Experimental Prediction of Heat Transfer Coefficients A Comparison of Four Commonly Used Techniques,” Exp. Therm. Fluid Sci., **1**, pp. 243–251.

[91] Luo, X., Roetzel, W., and Ludersen, U., 2001, “The single-blow transient testing technique considering longitudinal core conduction and ¯ uid dispersion,” Int. J. Heat Mass Transf., **44**, pp. 121–129.

[92] Shaji, K., and Das, S. K., 2010, “The effect of flow maldistribution on the evaluation of axial dispersion and thermal performance during the single-blow testing of plate heat exchangers,” Int. J. Heat Mass Transf., **53**(7-8), pp. 1591–1602.

[93] MathWorks, 2002, Curve Fitting Toolbox User’s Guide, The MathWorks, Inc.

[94] Aichlmayer, H. T., and Kulacki, F. A., 2006, “The Effective Thermal Conductivity of Saturated Porous Media,” Adv. Heat Transf., **39**, pp. 377–460.

[95] Boomsma, K., and Poulikakos, D., 2001, “On the effective thermal conductivity of a three- dimensionally structured fluid-saturated metal foam,” Int. J. Heat Mass Transf., **44**, pp. 827–836.

[96] Alexander, E. J., 1972, “Structure–property relationships in heat pipe wicking materials.,” North Carolina.

[97] Atabaki, N., and Baliga, B. R., 2007, “Effective thermal conductivity of water-saturated sintered powder-metal plates,” Heat Mass Transf., **44**(1), pp. 85–99.

[98] Elsner, A., Wagner, A., Aste, T., Hermann, H., and Stoyan, D., 2009, “Specific surface area and volume fraction of the cherry-pit model with packed pits.,” J. Phys. Chem. B, **113**(22), pp. 7780–4.

[99] Lowell, S., 1984, Powder surface area and porosity, Chapman and Hall, London.

[100] Kays, W. M., and London, A. L., 1964, Compact Heat Exchangers, McGraw-Hill, New York.

[101] Bock, J., and Jacobi, A. M., 2013, “Geometric classification of open-cell metal foams using X-ray micro-computed tomography,” Mater. Charact., **75**, pp. 35–43.

Appendix 1

1. Orifice plate calibration

The orifice plate was used to measure flow rate in this study was calibrated with a laminar flow meter (Cussons Technology P7250). The laminar flow meter (LFM) was connected to the inlet pipe of the steady pressure measurement test rig (Fig 3-1) and the pressure drop across the orifice plate and the laminar flow meter was measured. The following table (Table 1) shows the measured pressure drop across the orifice plate (ΔP) and calculated flow rate for orifice plate and LFM in litre per second. The error is the absolute value of the difference between two measured values.

Table A1.1

LFM ΔP (Pa)	Orifice ΔP (Pa)	Orifice flow rate (L/s)	LFM flow rate (L/s)	error %
107	154	4.93	4.90	0.52
136	248	6.23	6.22	0.23
149	299	6.83	6.81	0.39
161	349	7.38	7.37	0.12
173	401	7.91	7.91	0.02
192	490	8.75	8.77	0.30
212	600	9.67	9.67	0.03
227	695	10.41	10.39	0.17
242	786	11.07	11.08	0.11
243	789	11.09	11.09	0.01
261	910	11.91	11.91	0.06
275	1009	12.54	12.55	0.08
287	1098	13.08	13.09	0.10
301	1210	13.73	13.74	0.10
312	1306	14.26	14.27	0.05
324	1411	14.83	14.81	0.13
334	1493	15.25	15.26	0.07
347	1607	15.82	15.83	0.11
359	1721	16.37	16.41	0.25
368	1812	16.80	16.80	0.00
378	1916	17.27	17.28	0.07
389	2031	17.78	17.78	0.01
406	2221	18.59	18.57	0.12

The following equation was used to calculate the flow rate for orifice plate [48]:

$$q_m = \frac{\pi/4\, d_o^2 C_o \sqrt{2\Delta P \rho}}{\sqrt{(1-\beta^4)}} \qquad \text{Eq. A1.1}$$

Where d_o is the orifice plate inner diameter, C_o is the discharge coefficient, β is the pipe diameter to d_o. The orifice plate had 24.5 mm inner diameter and β was 0.46. The discharge coefficient was 0.632 and air density (ρ) was 1.195 on the calibration day.

Appendix 2

1. Diffusion number example

The following figure, Fig. A2.1 shows the predicted outlet temperature history generated by the model. In this example *NTU*=10, λ=0.001, R_{tc}=1, λ_w= 0, Δx=0.01 and $\Delta\tau$=0.001. Diffusion factor can be calculated as:

$$di = \lambda \frac{\Delta\tau}{\Delta x^2} = 0.001 \frac{0.001}{0.01^2} = 0.01$$

Diffusion number for this example is lower than 0.25 and the plotted graph of the model shows that the results was stable and not oscillate

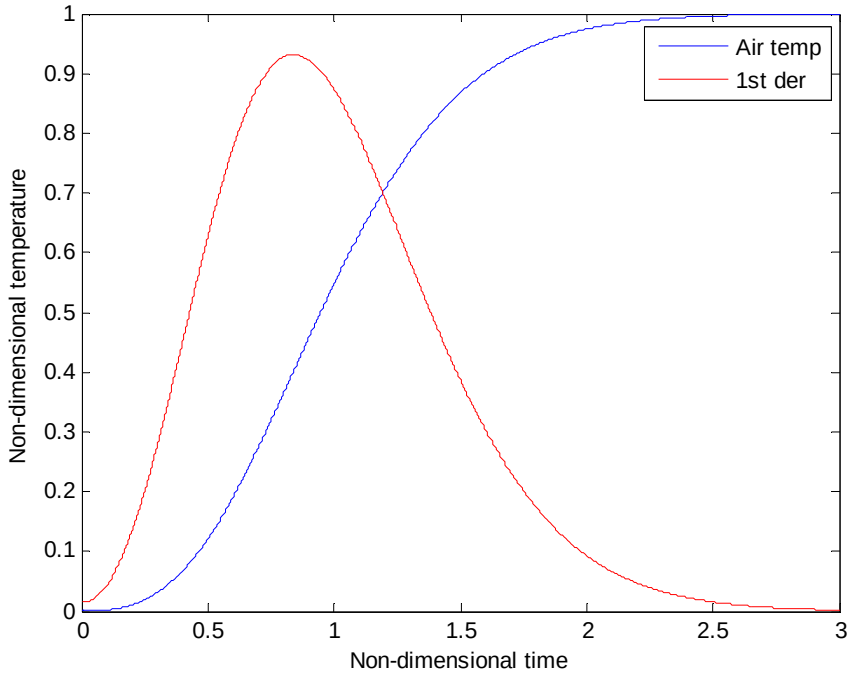

Fig. A2.1. Outlet temperature history for diffusion number of 0.01

The following will show the case that diffusion number was 0.5. In this example these input were used to predict the outlet temperature history: *NTU*=10, λ=0.05, R_{tc}=1, λ_w= 0, Δx=0.01 and $\Delta\tau$=0.001. Diffusion factor can be calculated as:

$$di = \lambda \frac{\Delta\tau}{\Delta x^2} = 0.05 \frac{0.001}{0.01^2} = 0.5$$

Shown in Fig. A2.2, is the outlet temperature history predicted by the model. The graph shows that the results was not stable and noticeably oscillate after 2.5 non-dimensional time.

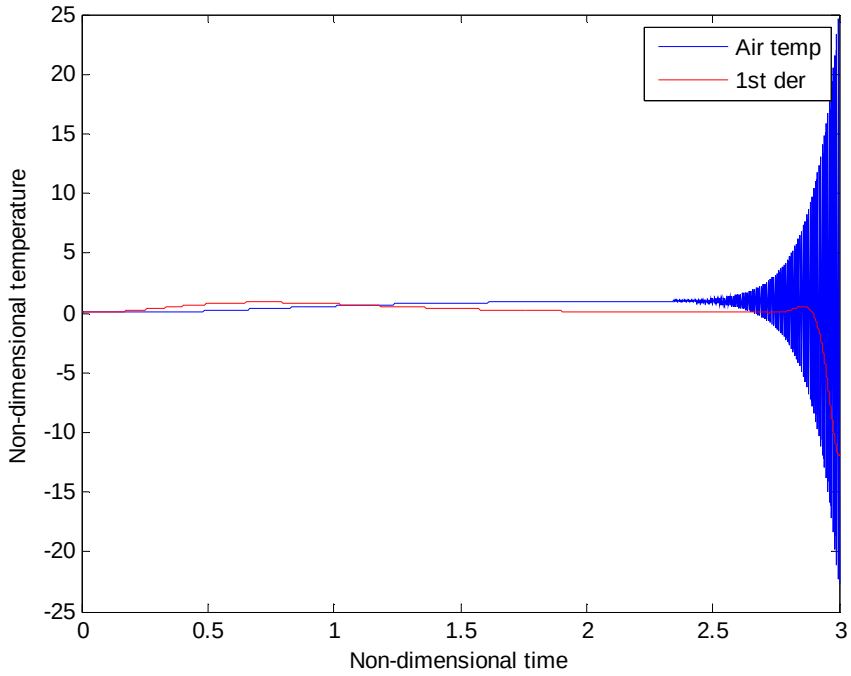

Fig. A2.2. Outlet temperature history for diffusion number of 0.5